Dissertation

Development and Validation of Masked Stereolithography for 3D Bioprinting with Cell-Laden Gelatin Methacryloyl Hydrogel

Benedikt K. Kaufmann

München, 2025

TUM School of Computation, Information and Technology

Development and Validation of Masked Stereolithography for 3D Bioprinting with Cell-Laden Gelatin Methacryloyl Hydrogel

Benedikt K. Kaufmann

Vollständiger Abdruck der von der TUM School of Computation, Information and Technology der Technischen Universität München zur Erlangung des akademischen Grades eines

Doktors der Ingenieurwissenschaften (Dr.-Ing.)

genehmigten Dissertation.

Vorsitz: Prof. Dr. Berna Özkale Edelmann

Prüfende der Dissertation:

1. Prof. Dr. Oliver Hayden
2. Prof. Dr. Hauke Clausen-Schaumann

Die Dissertation wurde am 15.04.2025 bei der Technischen Universität München eingereicht und durch die TUM School of Computation, Information and Technology am 11.09.2025 angenommen.

Abstract

Bioprinting has emerged as a promising technology within tissue engineering, with the potential to create highly customized and complex tissue constructs that aim to replicate the architecture and functionality of native tissues. This technology holds significant promise for applications such as drug testing, disease modeling, regenerative medicine, and ultimately for advancing personalized medicine. Despite notable progress, challenges persist, including the development of suitable bioinks, optimization of printing parameters, and integration of vascular networks. Additionally, there is no consensus on the ideal 3D printing technology for bioprinting, as each method presents unique advantages and limitations. Light-based technologies offer several advantages over other technologies, such as high spatial resolution and the ability to process protein-based biomaterials. Because of its fast layer-by-layer (rather than voxel-by-voxel) processing, among light-based technologies, masked stereolithography (mSLA) is a very promising method for the 3D printing of biomaterials. However, until today, no mSLA printer suitable for processing biomaterials has been introduced, and the application of the mSLA technology to bioprinting has not yet been investigated.

This doctoral thesis addresses this gap and, for the first time, investigates the potential of mSLA technology for bioprinting applications by demonstrating the application of mSLA to the bioprinting of cell-laden ECM-based protein resins. Key requirements for mSLA bioprinting were identified, and two conventional mSLA printers were modified accordingly by adding heating elements with temperature controllers and custom-made build platforms with removable glass substrates, resulting in a modular mSLA bioprinter concept. The printer design was validated using two gelatin methacryloyl (GelMA) derivates as protein resins, and the design and validation were published as an open-source project, allowing the scientific community to utilize the findings and accelerate the adoption of the technology. Suitable GelMA-based protein-resin, containing a cell-compatible photoinitiator and photoabsorber combination, were identified, and their concentrations were adjusted to allow cell-compatible high-fidelity printing. Subsequently, two cell lines derived from musculoskeletal tissue (hMSC and chondrocyte cell lines) were directly incorporated into the ECM-derived protein resins and used to print 3D constructs for the evaluation of cell behavior. Cell-laden samples were printed and cultured for multiple weeks and stained to visualize morphology and metabolic activity within the bioprinted artificial 3D matrix. Confocal z-stack imaging revealed spatially unconfined cell spreading, while cell morphology and distribution suggested a cellular response

to potential nutrient and stiffness gradients toward the construct's water-hydrogel interface. The results indicated that high cell viability, metabolic activity, and proliferation could be achieved within mSLA bioprinted constructs depending on the z-resolution. Samples printed at z-resolution (i.e., layer heights) approaching cell size (< 75 µm) exhibited reduced cell viability, suggesting that shear forces exerted on cells during the printing could be the primary cause.

In summary, this thesis, for the first time, investigated and successfully established mSLA in bioprinting applications. The approach was validated by printing complex 3D models with and without human cells directly incorporated into ECM-derived GelMA resins. Cell viability, metabolic activity, and proliferation were proven during subsequent 3D cell culture. This thesis thus provides a validated setup together with a suitable range of printing parameters for mSLA bioprinting enabling the generation of 3D cell-laden artificial tissue models with this promising, cell-friendly and fast 3D printing technology. By publishing a detailed description of the bioprinter design and printing parameters as an open-source project, the aim is to enable the scientific community and facilitate further advancements in the field of mSLA bioprinting.

Kurzfassung

Bioprinting hat sich zu einer vielversprechenden Technologie im Bereich des Tissue Engineering entwickelt, mit der sich hochgradig individualisierte und komplexe Gewebekonstrukte herstellen lassen, welche das Ziel haben, die Architektur und Funktionalität von nativem Gewebe zu replizieren. Diese Technologie ist äußerst vielversprechend für Anwendungen wie Arzneimitteltests, Krankheitsmodellierung, regenerative Medizin und letztendlich für den Fortschritt der personalisierten Medizin. Trotz bemerkenswerter Fortschritte gibt es immer noch Herausforderungen wie die Entwicklung geeigneter Biotinten, die Optimierung der Druckparameter und die Integration von vaskulären Netzwerken. Zudem gibt es keinen Konsens über die ideale 3D-Drucktechnologie für das Bioprinting, da jede Methode spezifische Vorteile und Einschränkungen aufweist. Lichtbasierte Technologien bieten eine Reihe von Vorteilen gegenüber anderen Technologien, wie etwa eine hohe räumliche Auflösung und die Möglichkeit, proteinbasierte Biomaterialien zu verarbeiten. Aufgrund ihrer schnellen schichtweisen Verarbeitung (statt Voxel für Voxel) ist die maskierte Stereolithografie (mSLA) unter den lichtbasierten Technologien eine äußerst vielversprechende Methode für den 3D-Druck von Biomaterialien. Jedoch wurde bis heute noch kein mSLA-Drucker vorgestellt, der für die Verarbeitung von Biomaterialien geeignet ist, und die Anwendung der mSLA-Technologie für das Bioprinting wurde bisher nicht untersucht.

Die vorliegende Doktorarbeit adressiert diese Lücke und untersucht zum ersten Mal das Potenzial der mSLA-Technologie für Bioprinting-Anwendungen, indem sie die Anwendung von mSLA für das Bioprinting von zellbeladenen ECM-basierten Proteinharzen demonstriert. Die Schlüsselanforderungen für das mSLA-Bioprinting wurden identifiziert, und zwei konventionelle mSLA-Drucker wurden entsprechend modifiziert, indem Heizelemente mit Temperaturreglern und individuell angefertigte Bauplattformen mit abnehmbaren Glassubstraten hinzugefügt wurden, wodurch ein modulares mSLA-Biodruckerkonzept entstand. Das Druckerdesign wurde unter Verwendung von zwei Derivaten von Gelatine-Methacryloyl (GelMA) als Proteinharze validiert. Das Design und die Validierung wurden als Open-Source-Projekt veröffentlicht, so dass die wissenschaftliche Gemeinschaft die Ergebnisse nutzen und die Etablierung der Technologie beschleunigen kann. Geeignete Proteinharze auf GelMA-Basis, die eine Kombination aus zellverträglichem Photoinitiator und Photoabsorber enthalten, wurden identifiziert, und ihre Konzentrationen wurden so angepasst, dass ein zellverträglicher Druck mit hoher Strukturtreue möglich ist. Anschließend wurden zwei aus muskuloskelettalem Gewebe stammende Zelllinien (hMSC- und Chondrozyten-Zelllinien) direkt in die ECM-Proteinharze

integriert und für den Druck von 3D-Konstrukten zur Evaluierung des Zellverhaltens verwendet. Zellbeladene Proben wurden gedruckt, mehrere Wochen lang kultiviert und anschließend angefärbt, um die Morphologie und die Stoffwechselaktivität innerhalb der künstlichen 3D-Matrix zu visualisieren. Konfokale z-Stapel-Bildaufnahmen zeigten eine räumlich nicht eingeschränkte Zellausbreitung, wobei die Zellmorphologie und -verteilung auf eine zelluläre Reaktion auf potenzielle Nährstoff- und Steifigkeitsgradienten in Richtung der Hydrogel/Wasser-Grenzfläche des Konstrukts schließen lassen. Die Ergebnisse zeigten, dass in Abhängigkeit von der z-Auflösung eine hohe Viabilität, Stoffwechselaktivität und Proliferation in den mit dem mSLA-Bioprinter hergestellten Konstrukten erreicht werden konnte. Bei Proben, die mit einer z-Auflösung (d. h. Schichthöhe) gedruckt wurden, die sich der Zellgröße (< 75 µm) annähert, war die Viabilität der Zellen verringert, was darauf hindeutet, dass Scherkräfte, die während des Drucks auf die Zellen ausgeübt werden, die Hauptursache sein könnten.

Zusammenfassend ist festzuhalten, dass in dieser Arbeit zum ersten Mal mSLA in Bioprinting-Anwendungen untersucht und erfolgreich etabliert wurde. Der Ansatz wurde durch den Druck komplexer 3D-Modelle mit und ohne menschliche Zellen validiert, die direkt in ECM-basierte GelMA-Harze integriert wurden. Zellviabilität, Stoffwechselaktivität und Proliferation wurden während der anschließenden 3D-Zellkultur nachgewiesen. Diese Arbeit liefert somit einen validierten Aufbau zusammen mit einem geeigneten Druckparameterbereich für das mSLA-Bioprinting, welches die Erzeugung von zellbeladenen künstlichen 3D-Gewebemodellen mit dieser vielversprechenden, zellfreundlichen und schnellen 3D-Drucktechnologie ermöglicht. Durch die Veröffentlichung einer detaillierten Beschreibung des Bioprinter-Designs und der Druckparameter als Open-Source-Projekt soll die wissenschaftliche Gemeinschaft befähigt und weitere Fortschritte auf dem Gebiet des mSLA-Bioprinting ermöglicht werden.

CONTENTS

Abbreviations

DAPI	4',6-Diamidino-2-phenylindol
DSBs	Double-strand breaks
DLP	Digital light processing
EBP	Extrusion-based bioprinting
ECM	Extracellular matrix
eGFP	Enhanced green fluorescent protein
GelMA	Gelatin methacryloyl
HEPES	4-(2-hydroxyethyl)-1-piperazineethanesulfonic acid
hMSC	Human mesenchymal stem cells
kDa	Kilodalton
LAP	Lithium-Phenyl-2,4,6-trimethylbenzoylphosphinat
MMPS	Matrix metalloproteinases
mSLA	Masked stereolithography
PA	Photoinitiator + photoabsorber solution
PBS	Phosphate-buffered saline
PhA	Photoabsorber
PhI	Photoinitiator
PI	Propidium iodide
QY	Quinoline yellow
RH	Relative humidity
ROI	Region of interest
RPM	Rounds per minute
RT	Room temperature
SLA	Stereolithography
2PP	Two-photon polymerization

1. Introduction

Preface: Selected passages and images have been adapted from the peer-reviewed publication Kaufmann et al., “mSLAb - An open-source masked stereolithography (mSLA) bioprinter” [1]. Direct quotes are italicized throughout this thesis.

Bioprinting comprises the adaptation of additive manufacturing technologies to biological, bio-derived, and bio-compatible materials to create highly customized and complex tissue equivalents that closely replicate the architecture and functionality of native tissues [2, 3]. By precisely depositing bioinks composed of living cells and biomaterials, bioprinting aims to fabricate functional tissue constructs for biomedical research, drug development, and tissue engineering [3-5]. The ultimate goal is to enable personalized medicine, where treatments can be tailored to the specific needs of individual patients, thereby improving therapeutic outcomes [6-8].

Despite the significant progress made in bioprinting, numerous challenges remain. These include developing suitable bioinks that support cell vitality and function, optimizing printing parameters to achieve high-resolution and structurally stable constructs, and integrating vascular networks to ensure adequate nutrient and oxygen supply to the printed tissues [9-11]. Additionally, there is no consensus on the ideal 3D printing technology for bioprinting, as each available technology offers unique advantages and limitations [2, 12-14]. Addressing these challenges requires ongoing research and innovation to fully realize the potential of bioprinting in tissue engineering and regenerative medicine.

While extrusion-based 3D printing technology is the most used, it often encounters limitations in achieving high resolution, structural fidelity, and the availability of suitable extracellular matrix (ECM)-derived materials. Recently, light-based technologies have gained significant attention from researchers, enabling the precise 3D structuring of ECM-derived materials down to the micrometer scale. While laser-based approaches, e.g., laser-based stereolithography (SLA) and two-photon polymerization (2PP), are used to structure scaffolds for subsequent seeding of cells, projection-based technologies like digital light processing (DLP) have been successfully used to print with cells directly incorporated within the biomaterial [15-20]. Masked stereolithography (mSLA) is a new projection-based approach to light-based 3D printing, leveraging the wide availability and continuous improvement of

high-resolution LCD screens designed for consumer goods (e.g., mobile phones and tablets) to selectively polymerize photosensitive polymers. mSLA has found widespread use among prosumers, 3D printing enthusiasts, and for prototyping and small-scale manufacturing in start-ups, using acrylic resins as materials. Researchers have already adopted this technology as a cost-effective solution for rapid prototyping, e.g., for microfluidic systems and molds [21-23].

Compared to traditional single-photon vat polymerization via SLA and DLP, mSLA offers a unique combination of high resolution, fast printing speeds, and low manufacturing costs. However, despite its potential, there is currently no published research on the application of mSLA in bioprinting.

The aim of this doctoral thesis was to explore the potential of mSLA technology for bioprinting applications. By developing a bioprinter based on mSLA, this work sought to create a tailored modular platform for fabricating high-resolution tissue constructs. This was implemented by modularly modifying a commercially available mSLA printer. This modular approach ensured that the modifications could be applied to future generations of printers, providing a sustainable platform for bioprinting. The results were published as an open-source project, allowing the scientific community to utilize the findings and accelerate the adoption of this technology.

The system was validated using state-of-the-art materials from the field of bioprinting. Specifically, gelatin methacryloyl (GelMA), an extracellular matrix (ECM)-based hydrogel, was used as a protein resin for printing. GelMA is widely recognized as an effective hydrogel for bioprinting applications due to its biocompatibility and tunable mechanical properties [16, 24-27]. For successful high-fidelity printing, GelMA must be combined with an appropriate photoinitiator and photoabsorber [24, 28]. It is essential to determine the optimal parameters, such as exposure time, and the concentrations of these additives for the desired z-resolution/layer thicknesses (e.g., 25, 50, 100 µm) [29-31].

Once the printing process was optimized, cells were integrated into the process to facilitate true 3D bioprinting. Specifically, human mesenchymal stem cell and chondrocyte-derived cell lines were used. Both cell types are derived from musculoskeletal tissue, where their natural environment is a collagen-rich ECM, making them well-suited for GelMA-based constructs. These cells were mixed directly with the material and printed with a homogeneous distribution within the construct. After printing, the samples were incubated and cultivated, followed by thorough analysis and characterization. The aim was to obtain comprehensive information on cell survival (cell viability), metabolic activity (e.g.,

mitochondrial activity), morphology, and cytoskeleton formation (F-actin fiber staining). Additionally, the ability of cells to proliferate within the constructs was investigated. Suitable staining methods for these analyses were established, and microscopy was performed using epifluorescence and confocal laser scanning microscopy.

The goal was to evaluate the potential and constraints of mSLA bioprinting with living human cells. The results were discussed in detail, generating recommendations for further experiments. This evaluation will provide valuable insights into the framework conditions necessary for successful bioprinting with cells with mSLA. This thesis provides guidelines, detailed materials and methods, and open-access published, open-source build instructions and software for the bioprinter. These resources not only ensure that the results can be reproduced but also enable further development based on these findings, contributing to the ongoing advancement of the field.

2. Fundamentals

2.1. Bioprinting

In the field of bioprinting, several additive manufacturing techniques are employed, differing significantly in their capabilities: Extrusion-based, jetting-based, and vat photopolymerization.

The most frequently used technology for generating artificial tissue constructs from ECM-based hydrogels is extrusion-based bioprinting (EBP). EBP creates three-dimensional structures by precisely layering the printing material through a nozzle or syringe in a predetermined pattern to construct tissue-like structures. Due to their simple construction, home-build EBP bioprinters can be realized easily, and numerous publications on conversions and upgrades for extrusion-based printers are available [32-35]. EBP is well suited to generate larger 3D constructs from highly viscous materials. However, EBP also has disadvantages: The printability of proteinaceous, ECM-based hydrogels is limited: As soft hydrogels with poor mechanical stability, 3D geometries printed from ECM proteins show poor shape fidelity and easily collapse under their own weight. Compared to other techniques, the resolution is relatively low because it is limited by the nozzle diameter, which ranges typically from about 100 µm to a few mm [36, 37].

Much finer resolutions can be achieved by jetting-based bioprinting, which includes techniques like inkjet printing, microvalve-based printing, and laser-induced-forward-transfer (LIFT). In jetting-based printing, small droplets of printing material are propelled onto the substrate. The size of each utilized droplet can be controlled precisely and is not limited by any nozzle [38, 39]. However, it is contingent upon the availability of suitable low-viscosity bioinks at low concentrations (typically $< 5\%$ (w/v)). The shear stress in the droplet formation process and during impact on the substrate is a primary factor limiting cell viability in printing cell-laden materials [10]. The LIFT process has a high cell viability and positioning accuracy [40, 41]. However, currently, LIFT is limited to predominately few-layer constructs and slow processing speeds (i.e., printed voxels over time) [42].

Vat photopolymerization uses a vat of liquid photopolymer, out of which the printed part is constructed layer by layer. A light source, usually a laser or a digital light projector, selectively cures and solidifies the photopolymer according to the

digital design provided to the machine. It is known for its high spatial resolution (approx.10 - 50 µm for single-photon excitation and 0.2 - 1 µm for two-photon excitation) and finish quality, making it suitable for applications requiring fine features and smooth surfaces [31]. Common technologies of vat photopolymerization include Stereolithography (SLA), Digital Light Processing (DLP), masked SLA (mSLA), and two-photon polymerization (2PP). Stereolithography (SLA) uses a laser to cure photosensitive resin layer-by-layer, offering high precision and surface quality but suffering from slow speeds as the laser has to scan the geometry voxel by voxel. Digital Light Processing (DLP) accelerates the process by projecting entire layers at once, using a digital micromirror device, resulting in faster printing with potential resolution limitations due to pixelation. 2PP achieves sub-micron resolution by focusing a laser beam to polymerize resin solely at the focal point via two-photon excitation, which is ideal for specialized applications requiring extreme detail. Due to its slow processing speed and high complexity, 2PP is a niche technology restricted to specialized applications [43-46].

Masked stereolithography (mSLA) is a variation of the traditional SLA process. In mSLA, an LCD screen is used as a digital mask to project the cross-sectional image of the desired object layer-by-layer onto the resin surface. The process begins with a vat of liquid photosensitive resin and a build platform that moves vertically towards the bottom of the vat, leaving a precise gap equal to the thickness of one layer between the substrate and the vat bottom. Once the layer is cured, the build platform retracts to release the cured layer from the bottom of the vat, and the process is repeated until the entire object is formed. This method allows for the simultaneous curing of an entire layer, rather than tracing the layer with a laser as in conventional laser-based SLA, retaining high resolution with improved processing speed.

The photosensitive material used in mSLA consists of at least one pre-polymer, a photoinitiator (PhI), and often a photoabsorber (PhA). The pre-polymer, which can be in the form of monomers and/or oligomers, can be tailored to achieve specific mechanical properties, while the PhI is chosen based on its absorption characteristics and efficiency in generating free radicals. The PhA is added to control the penetration depth of the light, ensuring that polymerization occurs only within the desired layer thickness [47]. This is crucial for achieving high resolution and preventing the curing of unintended areas [47]. The optimization of exposure time, PhI concentration, and PhA concentration is essential to achieving the desired z-resolution and ensuring the fidelity of the printed structures [47].

Compared to traditional single-photon vat polymerization via SLA and DLP, mSLA offers a unique combination of high resolution, fast printing speeds, and low manufacturing costs. However, despite its potential, there is currently no published research on the application of mSLA in bioprinting available.

2.2. Gelatin Methacryloyl

Gelatin Methacryloyl (GelMA) is a widely used biomaterial in light-based bioprinting due to its biocompatibility, biodegradability, and tunable mechanical properties [16, 24, 27, 48, 49]. GelMA is synthesized by modifying gelatin, which is derived from the partial hydrolysis of collagen, a major structural protein in the extracellular matrix (ECM) of various tissues [50, 51]. Collagen provides structural support and biochemical cues to cells, making gelatin an excellent starting material for creating biomimetic scaffolds [26, 50, 52]. The modification process involves introducing methacryloyl groups into the gelatin backbone, which enables GelMA to undergo photocrosslinking upon exposure to light in the presence of free radicals generated by a PhI.

Gelatin is used as the base material for GelMA because it retains many beneficial properties of collagen, including its ability to support cell adhesion, proliferation, and differentiation [25, 53-55]. By partly mimicking the natural ECM, GelMA provides a conducive environment for cells to grow and function, making it an ideal material for tissue engineering applications. GelMA was initially introduced into tissue engineering for creating hydrogels through casting and extrusion-based printing techniques, providing a supportive environment for cell growth and 3D culture applications. With the advent of light-based bioprinting technologies, GelMA can now be structured with high fidelity, enabling the precise fabrication of complex 3D tissue constructs.

The synthesis of GelMA typically involves reacting gelatin with a methacrylic reagent (e.g., methacrylic anhydride or glycidyl methacrylate) under controlled conditions (i.e., pH, temperature, and solvents used) [27, 48, 56-59]. This reaction introduces methacryloyl groups onto the gelatin molecules, allowing them to form covalent bonds when combined with a PhI and light. The degree of functionalization (DOF) can be adjusted by varying the reaction conditions, which in turn affects the mechanical properties (e.g., stiffness and rheology) and degradation rate of the resulting hydrogel [57-59]. This tunability is one of the key advantages of GelMA, as it allows researchers to customize the scaffold properties to match the requirements of different tissues. Numerous protocols have been published for the synthesis of various GelMA derivatives [27, 57-59].

Depending on the synthesis conditions, the gelatin's amino and hydroxyl groups are converted to functional groups. In the case of the RO-12h-L variant of GelMA, 56.3 ± 2% of the amino groups are functionalized by the introduction of methacrylic groups, yielding a GelMA that is in gel form at RT with good polymerization characteristics [27]. GM10 is a special GelMA derivate synthesized with a 10-fold molar excess of methacrylic reagent to yield a GelMA with nearly 100% conversion of free amino groups and exceptional crosslinking capability [57, 58]. This variant introduces not only methacrylic groups but also additional acetyl groups, which inhibit the formation of intermolecular helices and, thus, gelation at RT [57].

GelMA variants are typically classified based on the origin of the protein used, their synthesis methods, and the degree of functionalization [56, 60]. However, these classifications have not been standardized, which complicates the direct comparison of materials without detailed research. This lack of standardization can hinder the ability to quickly assess the suitability of different GelMA formulations for specific bioprinting applications. Despite this challenge, the versatility and tunability of GelMA continue to make it a popular choice for creating customized bioinks tailored to the needs of various tissue engineering and bioprinting applications [16, 24, 27, 48, 49].

2.3. Photoinitiator and Photoabsorber

2.3.1. Photoinitiator LAP

Lithium Phenyl-2,4,6-trimethylbenzoylphosphinate (LAP) is a widely used PhI in light-based bioprinting due to its high efficiency, low toxicity, and rapid polymerization capabilities [61-63]. LAP is particularly favored in bioprinting applications over alternatives like Irgacure 2959 because it initiates polymerization under visible light, which is less harmful to cells compared to ultraviolet light [64]. This property makes LAP an excellent choice for creating cell-laden bioprinted constructs.

LAP is a small organic molecule with a phenyl ring substituted at the 2, 4, and 6 positions with methyl groups and a phosphinate group attached to the benzoyl moiety. The chemical structure of LAP allows it to absorb light in the visible spectrum from 400 nm to 420 nm [61]. Upon exposure to light, LAP undergoes a photochemical reaction where the energy absorbed from the light causes the cleavage of the phosphinate bond, generating reactive free radicals [61, 65]. After excitation and cleavage, the light absorption of the remaining molecule is reduced (i.e., photobleaching occurs), and light can penetrate

deeper into the material and excite additional LAP molecules, increasing its efficiency [61].

These free radicals are highly reactive species that can initiate the polymerization process. In the context of GelMA, the free radicals generated by LAP interact with the methacryloyl groups present in the GelMA molecules. This interaction leads to the formation of covalent bonds between the methacryloyl groups, resulting in the crosslinking of the GelMA hydrogel. The crosslinking process transforms the GelMA solution into a solid hydrogel network, providing the necessary mechanical stability and structural integrity for tissue engineering applications [29].

The high solubility of LAP in water is another significant advantage over other PhIs, as it ensures uniform distribution within the GelMA solution, leading to efficient and homogeneous polymerization [28, 62]. The ability of LAP to initiate polymerization under visible light reduces the risk of photodamage to cells, enhancing cell viability and function within the printed constructs [62, 63]. Additionally, LAP's low toxicity at concentrations of ≤ 0.5% ensures that it does not adversely affect cell health, making it suitable for a wide range of tissue engineering applications [62, 63, 66].

The use of LAP in bioprinting has been extensively studied, and its performance has been validated in various applications, including the fabrication of tissue models, drug delivery systems, and organ-on-a-chip models [18, 67-70]. Despite its widespread use, the concentration of LAP and the exposure time to light must be carefully optimized to achieve the desired polymerization without compromising cell viability due to possible oxidative stress.

2.3.2. Photoabsorber QY

In light-based bioprinting, the PhA plays a critical role in controlling the polymerization process. The primary function of a PhA is to absorb light at the same wavelength as the PhI, leading to a rapid decay of available photons for PhI excitation. This absorption mechanism is essential for inhibiting crosslinking outside the desired volume (i.e., voxel). By carefully setting the concentration of the PhA, the polymerization depth can be precisely controlled to achieve the desired z-resolution (i.e., layer height) [47, 71]. The PhA substantially enhances the lateral (x and y) resolution and overall print fidelity. Without an appropriate PhA in the resin, the light would penetrate through multiple layers, leading to the polymerization of unwanted features and resulting in prints with diffuse x and y characteristics. Therefore, with the exception of 2PP, the inclusion of a PhA is a

necessity to ensure high-resolution and accurate 3D constructs in light-based printing.

Quinoline Yellow (QY) is a food dye (E 104) approved as a food additive in the European Union that has found applications within tissue engineering, e.g., as a cell-compatible yellow dye for hydrogel applications due to its high water-solubility paired with low toxicity [72]. Though there has been some controversy regarding the extensive use of synthetic dyes like QY as food additives, they remain widely used in scientific hydrogel applications [73]. The QY absorption spectrum has a peak at 416 nm and high absorption at 405 nm, making it an ideal candidate for a PhA for light-based bioprinting applications with LAP and has been used as such for DLP printing of (PEGDA) hydrogels [15, 19, 20, 74, 75]. QY absorption follows Lambert-Beers Law of extinction (i.e., linear increase of absorption in dependence on concentration, leading to an exponential decay of the illumination intensity in z-direction), which is helpful for intra- and extrapolation of suitable QY concentrations for specific z-resolutions [76].

3. Hypothesis

Bioprinting holds the promise of generating highly customized complex tissue constructs that mimic the architecture and functionality of native tissues. Despite significant advancements, the application of mSLA in bioprinting remains unexplored. This thesis aims to fill this knowledge gap by developing and validating an mSLA bioprinter for printing ECM-based materials. The central hypothesis of this thesis is that mSLA technology can be adapted for bioprinting applications to produce high-fidelity, cell-laden artificial tissue constructs that can be cultured with high viability. In particular, the following research questions were addressed:

1. Can mSLA be used for bioprinting of ECM-based materials, and what are the key requirements for mSLA bioprinters?

2. Can GelMA-based protein resins, containing a cell-compatible photoinitiator and photoabsorber combination, be identified for mSLA bioprinting, and how do these compositions, along with printing parameters (e.g., exposure time, layer height), affect the printability and fidelity of constructs?

3. Can different cell lines be incorporated into the mSLA bioprinting process and be printed with sufficient cell viability? Can the cell-laden constructs subsequently be cultured to allow for the evaluation of cell behavior within the constructs?

4. Which process parameters influence cell viability, and can suitable process windows be identified to balance cell viability and printing resolution?

4. Materials and Methods

In this chapter, the experimental methods, materials used, and data analysis procedures are described. All percentages given are weight/volume (w/v) unless stated otherwise. Further details, including the step-by-step instructions for the conversion of the 4K 3D printer and a list of all necessary standardized mechanical and electronic parts, are published in Kaufmann et al. (2024) [1]. CAD files for the 3D-printable parts are published in the accompanying online data repository under the Creative Commons (CC-BY-SA 4.0) open-source license [77].

4.1. GelMA Hydrogel synthesis

4.1.1. RO-12h-L

RO-12h-L GelMA variant was synthesized according to Kumar et al. [27].

Briefly, GelMA type RO-12h-L was synthesized in 10-gram batches by dissolving 10 g porcine gelatin (Type A, Bloom Strength ~ 300, G1890, Sigma Aldrich) in 100 ml reverse osmosis (RO) H_2O in a 250 ml glass beaker. Throughout the synthesis, the beaker remained on a magnetic stirrer set to 50 °C and 500 RPM (Rounds per minute) with the temperature probe submerged in the liquid. To minimize evaporation, the beaker was covered with two layers of Parafilm. The pH was adjusted to 3.5 by drop-wise addition of 25% acetic acid (7332.1, Carl Roth) using a burette. To start the synthesis, 18 ml of glycidyl methacrylate (GMA) (779342, Sigma Aldrich) was added gradually over 30 minutes (~600 µl/min) using a burette. The reaction then continued for an additional 12 hours at 50 °C and 500 RPM. The reaction was stopped by adding 100 ml of RO H_2O, and the solution was transferred into four pieces of 12-14 kDa dialysis tubing (888-11539-EA, Spectrum Chemical), each measuring 35 cm. It was dialyzed against RO H_2O in two 5000 ml beakers on a magnetic stirrer set to 200 RPM at room temperature for three days. The RO H_2O was replaced every 12 hours. Following the dialysis, the tubes were cut open, and the product was combined in a 250 ml beaker and heated to 50 °C on a magnetic stirrer set to 500 RPM. The heated solution was filtered with a glass microfiber filter (GF 6, Whatman) and again with a 0.45 µm cellulose nitrate filter (11406-50-ACN, Sartorius) using a bottle top filter (DS0320-2545, Thermo Scientific). The filtrate was divided into 25 ml portions, which were pipetted into 50 ml sterile centrifuge tubes and frozen at -20 °C. The frozen tubes, without lids, were lyophilized

at -80 °C and 0.1 mbar for 7 days. Lyophilized RO-12h-L was stored at -20 °C until use.

4.1.2. GM10

GM10 GelMA variant was synthesized according to Hoch et al. [57, 58].

Briefly, GelMA type GM10 was synthesized in 10-gram batches by dissolving 10 g bovine gelatin (Type B, Bloom Strength ~ 225, G9391, Sigma Aldrich) in 80 ml 7.4 pH 100 mM phosphate buffer (prepared by combining 15.2 ml 100 mM NaH_2PO_4 (2370.1, Carl Roth) and 64.8 ml 100 mM Na_2HPO_4 (T876.1, Carl Roth)) in a 250 ml glass beaker. Throughout the synthesis, the beaker remained on a magnetic stirrer set to 50 °C and 500 RPM with the temperature probe submerged in the liquid. To minimize evaporation, the beaker was covered with two layers of Parafilm. The pH was adjusted to 7.4 by drop-wise addition of 4 M NaOH (6771.1, Carl Roth) using a burette. To start the synthesis, 5.2 ml of Methacrylic anhydride (MA) (276685, Sigma Aldrich) was added gradually over 1 hour (~75-100 µl/min) using a burette. The pH of the solution was monitored and maintained between pH 7.0 and 7.4 using 4 M NaOH during the addition of MA and for an additional two hours. The product was transferred into six pieces of 12-14 kDa dialysis tubing, each measuring 35 cm. It was dialyzed against RO H_2O in three 5000 ml beakers on a magnetic stirrer set to 200 RPM at room temperature for three days. The RO H_2O was replaced every 12 hours. Following the dialysis, the tubes were cut open, and the product was combined in a 1000 ml beaker and heated to 30 °C on a magnetic stirrer set to 500 RPM. The heated solution was filtered with a glass microfiber filter (GF 6, Whatman) and again with a 0.45 µm cellulose nitrate filter (11406-50-ACN, Sartorius), using a bottle top filter (10231751, Thermo Scientific). The filtrate was divided into 25 ml portions, pipetted into 50 ml sterile centrifuge tubes, and frozen at -20 °C. The frozen tubes, without lids, were lyophilized at -80 °C and 0.1 mbar for 7 days. Lyophilized GM10 was stored at -20 °C until use.

4.2. mSLA Bioprinting

Two different commercially available mSLA 3D printers (Phrozen Sonic Mini 4K and Phrozen Sonic Mini 8K) were modified to enable bioprinting with protein resins. **Figure 1** shows an overview of all modifications made to the Phrozen Sonic Mini 4K printer to convert it to a mSLA bioprinter (mSLAb). Modifications include a microcontroller-based temperature controller (**Figure 1** E), which combined with resistive heating pads (**Figure 1** D) and two temperature sensors,

one of them on the resin reservoir (**Figure 1** C) and one near the heating pads on the z-axis (**Figure 1** D), lets the user set a temperature between 25-37 °C and heats the printer automatically. The introduction of a custom-designed platform (**Figure 1** A) with exchangeable glass substrates facilitates reduced material consumption and easy sample handling for downstream processes.

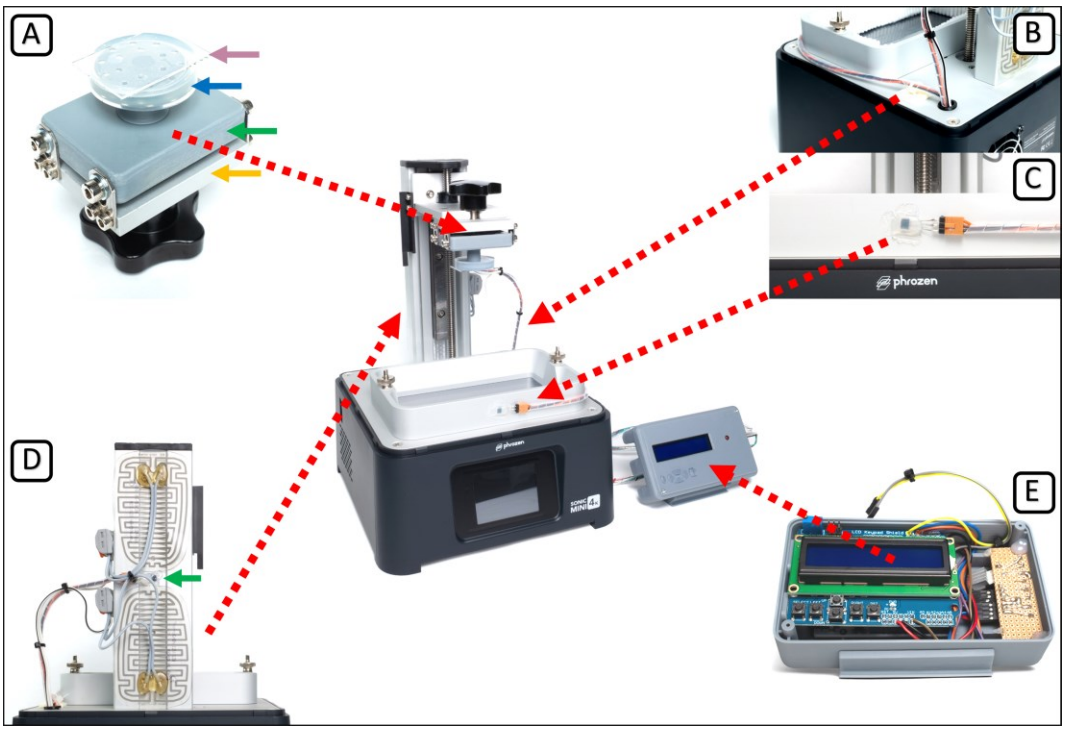

Figure 1: mSLA bioprinter modifications overview. Custom-designed build platform (A) with exchangeable glass substrate (purple arrow). The silicone-encased build platform (blue arrow) and base plate (green arrow) are attached to the original attachment plate (orange arrow). Temperature control is achieved by combining a microcontroller-based temperature controller with an LCD keypad user interface (E) with resistive heating pads on the back of the aluminum z-axis (D). Sensors to monitor temperatures were placed on the z-axis between the heating pads (D, green arrow) and the front of the material vat (C). Cables for sensors and heaters are neatly routed via a hole in the printer's base plate (B). (Images from Kaufmann et al. 2024)

Chapter 5.1 details the modification and validation process of the mSLAb system. The published version of the printer modification, “mSLAb – An open-source masked stereolithography (mSLA) bioprinter” (Kaufmann et al., 2024), includes a detailed description and step-by-step instructions for the conversion of the 4K 3D printer and a list of all necessary standardized mechanical and electronic parts. CAD files for the 3D-printable parts and a video demonstration were published in the accompanying open-source online data repository under the Creative Commons (CC-BY-SA 4.0) open-source license [77]. **Chapter 5.1.5** details the subsequent application of the concept of bioprinting modification for an mSLA system to a next-generation printer with 8K resolution (Phrozen Sonic Mini 8K).

This chapter describes the materials and methods used to print gelatin methacryloyl resins combined with cells on the mSLAb systems.

Figure 2 shows the operation flowchart for the mSLAb printing process, guiding the user from the start-up of the printer to the start of a print job. Briefly, the printer was pre-heated to 35 °C using the temperature controller, and the edges of the printing vat were lined with folded sterile surgical caps wetted with RO H_2O for humidification (> 90% relative humidity (RH)). Heating to 35 °C sufficiently reduced the viscosity of the material for successful mSLA printing and ensured that the additional heat introduced by the exothermic photopolymerization reaction did not lead to temperatures exceeding physiological conditions (37 °C) to maintain cell viability. Refer to **Chapter 5.1.4** for details.

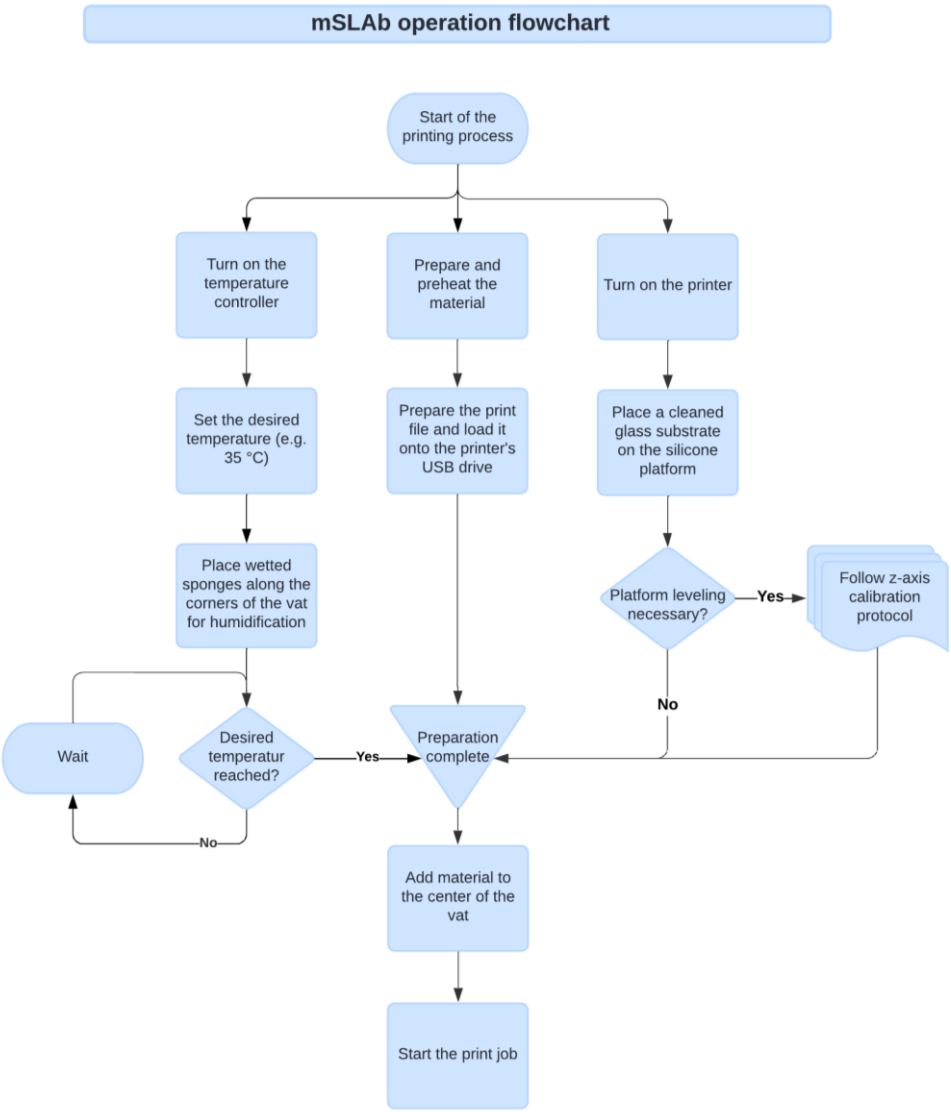

Figure 2: The mSLAb operation flowchart. The mSLAb operation flowchart provides a supplementary step-by-step overview of the process from printer start-up to starting a print. (Image adapted from Kaufmann et al. 2024)

3D models for bioprinting were designed using computer-aided design (CAD) software SolidWorks (Dassault Systèmes) and supplemented by an adhesion platform of 500 µm thickness to enhance substrate adhesion and compensate for possible planar tilting of the build platform and minimal thickness variations of the substrate. Print job files were generated by slicing the 3D models with Lychee Slicer (Mango 3D) slicing software. **Figure 3** is a screenshot of exemplary print settings in Lychee Slicer software used for printing with the 4K version of mSLAb. Key settings include the layer thickness (i.e., z-resolution) and exposure times. Exposure times and PhA concentrations were adjusted for specific layer heights (refer to **Chapter 5.2.1**) and are mentioned alongside the respective samples in the results section.

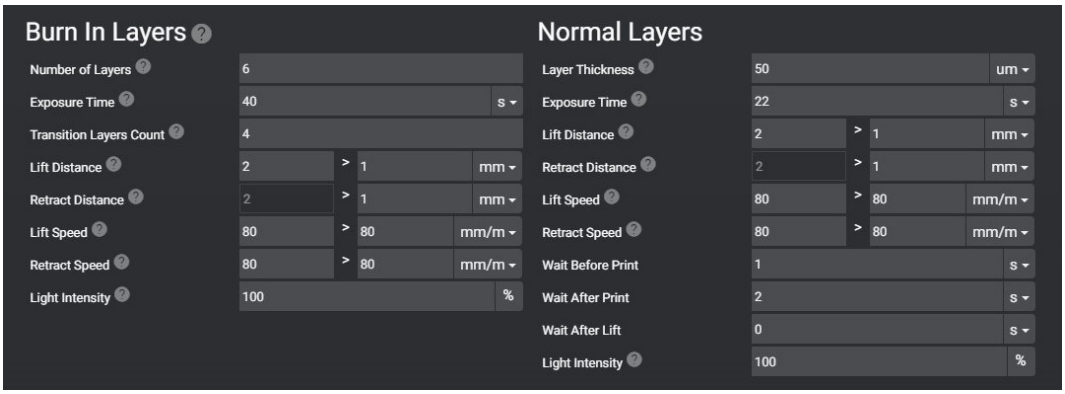

Figure 3: Screenshot of exemplary print settings in Lyche Slicer software. Exemplary slicer settings for a print with 50 µm layer height on the 8K version of mSLAb.

"Burn In" layers with long exposure times facilitate good adhesion of printed structures to the substrate. "Normal" layer settings apply after the number of "Burn In" and "Transition" layers are completed. "Transition" layers provide a linear gradient of varied exposure time to bridge the gap between the settings for "Burn In" and "Normal" layers and reduce possible tension between layers printed with noticeably different exposure times, which otherwise may lead to delamination of layers and failed prints.

The number of “Burn In” layers and “Transition” layers were set to match the thickness of the adhesion platform in a 2:3 ratio, i.e., for a 100 µm layer height print job and 500 µm adhesion platform, there were two burn-in layers and three transition layers. This ensured comparable conditions for all layer heights with good adhesion, gradual transition from “burn-in” to “normal” layer exposure times, and homogenous “normal” exposure times throughout the entire relevant construct, e.g., the gyroid structure.

To evaluate the cell viability and prove the capability of the mSLAb system to print complex 3D models with protein resin, multiple 3D models based on a

gyroid structure were designed. The gyroid model, a triply periodic minimal surface, was first described by Alan Schoen in 1970 and has since been discovered in multiple naturally occurring structures such as butterfly wing scales and bird feathers [78-81]. This biomimetic 3D model exhibits unique mechanical properties, such as a high strength-to-weight ratio and high mechanical isotropy [82, 83]. 3D printing technology allows for the generation of arbitrary geometries, thereby leveraging the benefits of the gyroid model. When used as a lightweight infill pattern, the gyroid structure enhances the mechanical stability and efficiency of printed constructs [84-86]. In the context of bioprinting, the gyroid model offers significant advantages as a scaffold for cell-laden constructs. Its porous nature facilitates efficient nutrient and metabolite exchange, which is crucial for maintaining cell viability and promoting proliferation [20, 87, 88].

By adopting the gyroid model and adjusting the pattern amplitude and lamella thickness, the design can be adapted to specific size and resolution requirements. The lamella thickness for the experiments was set between 200 and 500 µm to ensure optimal diffusion and to demonstrate the capability of printing 3D structures with a high surface-to-volume ratio. These structures could be printed with high fidelity and cultivated via passive diffusion of cell culture media, proving them suitable for tissue engineering applications.

The bioink components are prepared as individual stock solutions, considering their solubility, shelf-life, and the ability to prepare individual bioink combinations on demand for the experiments. All stock solutions were prepared by thoroughly mixing them with inversion and/or vortexing cycles intermitted by heating in a water bath at 45 °C. Photosensitive solutions were stored in non-translucent Eppendorf tubes.

Figure 4 shows the workflow for bioink preparation used for mSLAb printing, including individual steps and exemplary values.

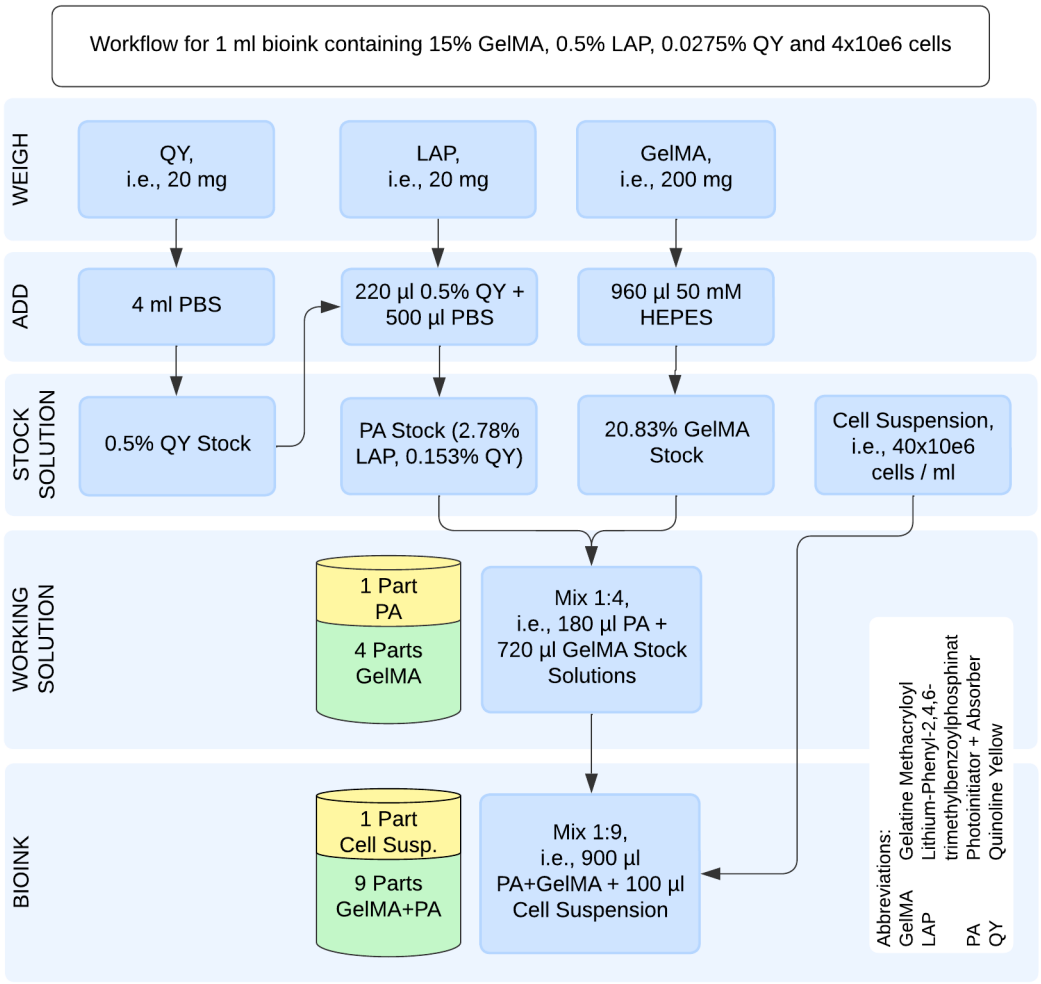

Figure 4: GelMA-based bioink preparation flowchart. Flowchart showing the workflow for bioink preparation used for mSLAb printing, including individual steps and exemplary values for 1 ml bioink containing 15% GelMA, 0.5%, 0.0275% QY, and 4x10^6 cells.

First, the Quinoline Yellow (QY) PhA was prepared as a stock solution of 0,5% in PBS (phosphate-buffered saline, BS.L1825, Bio&SELL). Second, the desired final concentration of LAP, QY, and GelMA was considered. A combination of the PhI and PhA (i.e., the PA solution) was prepared by weighing 10-20 mg LAP and adding QY stock solution plus PBS to result in a PA solution with a QY and LAP concentration of $\frac{50}{9}$ times the final desired concentrations, i.e., 2.78% LAP for a final concentration of 0.50% LAP in the bioink. GelMA is prepared by dissolving lyophilized RO-12h-L with 50 mM HEPES (4-(2-hydroxyethyl)-1-piperazineethanesulfonic acid, 6763.1, Carl Roth) or GM10 with 100 mM HEPES to a concentration of $\frac{25}{18}$ times the final desired concentration, i.e., 20.83% for a final concentration of 15.00% of GelMA in the bioink. For early validation experiments without cells, all solutions were prepared with RO H_2O instead of physiological buffers. The PA and GelMA solutions were stored for up to a week at 5 °C before and between use. Immediately before

experiments, the GelMA and PA solutions were preheated to 37 °C and combined by mixing four parts of GelMA and one part of PA solution. The final step was combining nine parts of GelMA + PA biomaterial with one part of cell suspension prepared with 10-fold excess concentration (i.e., $40x10^6$ cells/ml for a final concentration of $4x10^6$ cells/ml) in 50 mM HEPES. For details on cell culture, refer to **Chapter 4.5**. For experiments without cells, the cell suspension was substituted with 50 mM HEPES.

The mSLAb printing process begins with a fresh glass substrate placed on the printing platform and a droplet of bioink positioned at the center of the LCD (**Figure 5** A). As the print job starts, the glass substrate moves towards the LCD, creating a gap equal to one layer height (the set z-resolution) filled with liquid photosensitive bioink (GelMA) (**Figure 5** B). The LCD selectively cures a layer of GelMA, after which the platform retracts to lift the printed layer. The platform then reapproaches, maintaining a gap of one layer height between the newly formed layers and the LCD. This process of selectively curing the GelMA and retracting the platform is repeated until the entire part is formed (**Figure 5** C). Once printing is complete, the sample, along with the glass substrate, is removed from the print platform, post-processed to wash away any uncured GelMA, and prepared for high-resolution microscopy (**Figure 5** D).

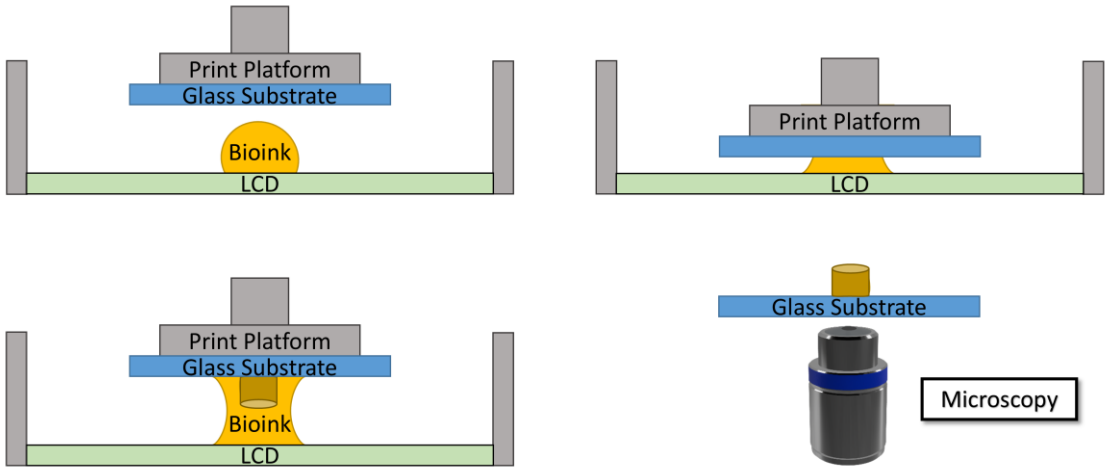

Figure 5: Schematic representation of the mSLAb printing process. (A) A fresh glass substrate is placed on the printing platform, and a droplet of bioink is positioned at the center of the LCD. (B) The substrate moves towards the LCD, creating a gap filled with liquid GelMA, which is selectively cured. (C) The platform retracts and reapproaches, repeating the curing process until the part is formed. (D) The printed sample is removed, post-processed to remove uncured GelMA, and prepared for microscopy.

When printing with cells, the printer is sterilized and positioned inside a laminar flow cabinet to minimize potential contamination. The sterilization process involves disinfecting the surface with 80% ethanol, followed by a 20-minute exposure to UV light at start-up. Printed samples are then handled

according to standard sterile cell culture procedures. The glass substrates used were standard microscope slides (631-0701, VWR) with a thickness of 1 mm, cut in half during the initial experiments (i.e., 4K mSLAb printer validation), and 30 mm diameter microscopy round cover slides with 170 µm thickness (MARI0117700, VWR). Thicker substrates can be removed easily by careful lifting (refer to the video demonstration in the data repository), while thin substrates can be more challenging to remove. Using a piece of unwaxed dental floss carefully wedged between the substrate and silicone build platform facilitates easy and reproducible removal for thin (i.e., 170 µm) glass substrates. Cell-laden printed samples were placed in 35 mm Petri dishes, covered with 3 ml of cell culture medium, and incubated at 37 °C with 5% CO_2 in a humidified incubator (refer to **Chapter 4.5** for cell-specific media). The medium was replaced after 24 hours and then twice a week for the duration of the culture.

4.3. 3D printed parts

3D models for 3D printing were designed using computer-aided design (CAD) software SolidWorks (Dassault Systèmes) and sliced in Lychee Slicer (Mango3D) for mSLA printing and Ultimaker Cura (Ultimaker) slicing software for FDM printing. Prototypes were printed using FDM and Ultimaker 2+ and Ultimaker 3 printers with standard PLA filaments (BASF Ultrafuse PLA) at 100 µm z-resolution.

The final versions of 3D-printed parts used to modify the Phrozen Sonic printers were printed with the respective Phrozen Sonic Mini 4K and 8K versions and Phrozen Aqua Grey 4K and 8K resin at 100 µm z-resolution. Prints were washed in isopropanol and cured with 405 nm light for 15 minutes. Surfaces that were later exposed to silicone were post-cured with 405 nm light exposure for 1 hour or heat treatment (120 °C for 4 hours) to prevent silicone polymerization inhibition due to residual photoinitiator leakage from insufficiently cured parts [89, 90].

4.4. Build Platform Assembly and Silicone Casting

Custom-design silicone parts were manufactured by casting two-component room-temperature vulcanizing silicone (SF-45, Versandhandel Blioch) into 3D-printed molds. Molds were printed and post-processed according to **Chapter 4.3**, filled with silicone, and left to cure at room temperature for at least 2 hours or overnight. Custom silicone parts include the seal for the z-axis homing sensor of the Phrozen 4K printer, the keypad used in the temperature controller, and silicone-encased print platforms. The keypad

was cast using a reusable open-source mold, and the sensor seal was cast in a single-use mold that breaks easily on designed weak points for silicone removal [1, 77]. The silicone-encased print platform for the 4K printer was created by suspending the build platform assembly (**Figure 6** A) approximately 1.5 mm above the surface of a 30 mm Petri dish and filling the dish with silicone. This was accomplished using a specially designed 3D-printed molding stand equipped with three screws for leveling (refer to **Figure 6** B and C).

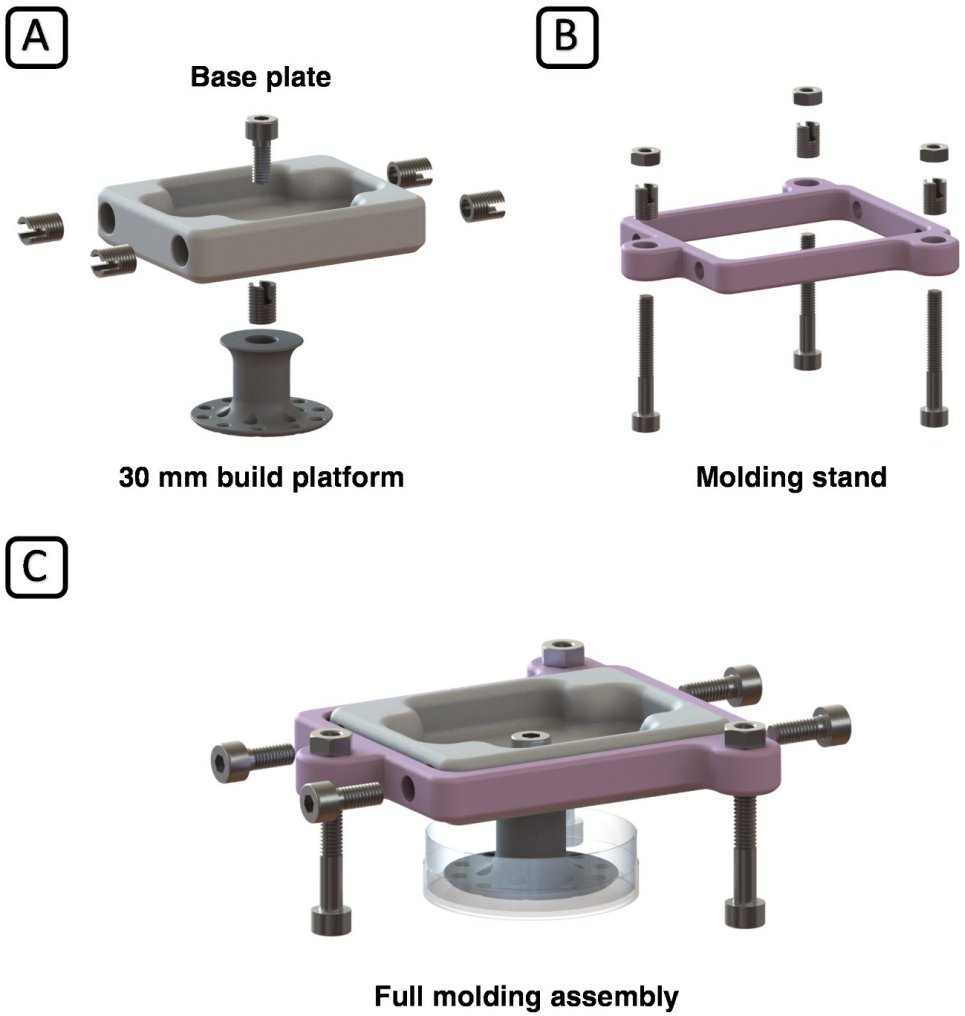

Figure 6: Detailed overview of the mSLAb build platform (4K version). Detailed overview of the build platform assembly (A), molding stand with three screws for leveling (B), and the complete molding assembly used to cast silicone around the build platform (C), including the positions of the thread inserts and screws. (Images from Kaufmann et al. 2024)

Minor changes to the design of the build platform for use with the Phrozen Sonic Mini 8K printer are discussed in **Chapter 5.1.5**.

4.5. Cell culture

Description of cell culture for SCP-1(eGFP) and TC28a2 cell lines.

4.5.1. SCP-1(eGFP) Human Mesenchymal stem cell line

The SCP-1 cell line is an immortalized human mesenchymal cell line derived from human bone marrow with constitutive eGFP expression [91, 92].

SCP-1 cells were cultured in T-175 flasks using Dulbecco's Modified Eagle Medium (DMEM) with sodium pyruvate (BS.FG 0445, Bio&SELL), supplemented with 10% fetal calf serum (FCS; F7524-500mL, Sigma-Aldrich), 1% Penicillin-Streptomycin (BS.A 2213, Bio&SELL), and 1% GlutaMAX (35 050 038, Life Technologies) at 37 °C and 5% CO^2 in a humidified incubator. Cells were passaged at approximately 80% confluency in a 1:5 ratio. Briefly, cells were washed with 10 ml PBS at 37 °C and then incubated with 5 ml Trypsin (1:250) / EDTA (0,25%/0,02%) solution (BS.L 2163, Bio&SELL) for 5 minutes at 37 °C. Trypsin was inactivated by adding 6 ml of fresh DMEM, and 7.2 ml of the cell suspension was either discarded or used for experiments.

4.5.2. TC28a2 Human Chondrocyte Cell Line

The TC28a2 cell line is an immortalized human chondrocyte cell line derived from human costal cartilage [93, 94].

TC28a2 cells were cultured in T-175 flasks using DMEM without sodium pyruvate, supplemented with 10% FCS, 1% Penicillin-Streptomycin, and 1% GlutaMAX at 37 °C and 5% CO^2 in a humidified incubator. Cells were passaged at approximately 80% confluency in a 1:10 ratio. Briefly, cells were washed with 10 ml PBS at 37 °C and then incubated with 5 ml Trypsin (1:250) / EDTA (0,25%/0,02%) solution for 8 minutes at 37 °C. Trypsin was inactivated by adding 6 ml of fresh DMEM, and 7.2 ml of the cell suspension was either discarded or used for experiments.

4.6. Microscopy and Cell Staining

Description of the microscopy setups used and the corresponding cell staining procedures that have been established for the specific samples.

4.6.1. Epifluorescence

Epifluorescence images were acquired using an Axio Observer Z1 (Carl Zeiss) equipped with structured illumination (Aptome-2 module). All images were acquired with an EC Plan-Neofluar 10x/0.30 Ph1 objective (Carl Zeiss).

Selected printed constructs were stained using propidium iodide ReadyProbes Reagent (R3710, ThermoFisher Scientific). Media in the Petri dishes containing the printed samples was removed and replaced with 3 ml fresh medium containing 140 µl of propidium iodide Solution. The cells were imaged after an incubation period of 5 minutes at 37 °C. In addition, the SCP-1(eGFP) cell line expresses eGFP fluorescent protein constitutively, staining the cytosol. Images were acquired using the dsRed (Filter Set 49 HE, Carl Zeiss) and eGFP (Filter Set 38 HE, Carl Zeiss) channels, respectively.

γ-H2AX assays were performed using Phospho-Histone H2A.X (Ser139) Monoclonal Antibody with eFluor 660 (eBioscience, Invitrogen). Following the light exposure event, the samples were cultured for 30 minutes at 37 °C to reach the maximum concentration of γ-H2AX [95]. Samples were fixed with 3.7% formaldehyde (CP10.1, Carl Roth) in PBS at 37 °C for 10 minutes, washed with PBS, and fixed with ice-cold methanol (100%) for 5 minutes at -20 °C. Afterward, samples were washed three times with PBS and permeabilized using 0.1% Triton X-100 (X100, Sigma-Aldrich) in PBS for 15 minutes at RT. Then, the samples were washed three times again using PBS. To minimize unspecific binding, samples were then blocked using 3% FBS in PBS and incubated for 60 minutes at RT. The blocking solution was then replaced with H2A.X antibody in 1:20 dilution and 0.1% FBS in PBS, resulting in a final antibody concentration of 2.5 µg/ml. Following incubation overnight at 4 °C, the samples were washed three times with PBS, and cell nuclei were stained using 0.1% DAPI (4',6-Diamidino-2-phenylindol) stock solution (1 mg/ml DAPI (6335.1, Carl Roth) in RO H_2O) in PBS for 30 minutes at RT and protected from light. Finally, the samples are washed with PBS three times and imaged using the CY5 (Filter Set 50, Carl Zeiss) and DAPI (Filter Set 49, Carl Zeiss) channels.

4.6.2. Confocal Microscopy

Confocal fluorescence z-stack images were acquired using a Stellaris 8 confocal laser scanning microscope (Leica Microsystems) and the HC PL FLUOTAR L 20x/0.40 DRY objective (Leica Microsystems).

Mitochondrial activity was visualized using MitoTracker Deep Red (M22426, ThermoFisher Scientific) in DMSO. MitoTracker solution was added by removing half of the supernatant (1.5 ml) of the cell-laden constructs in Petri dishes and adding the same amount of fresh medium supplemented with MitoTracker, yielding a final concentration of 500nM. Samples were incubated for 45 minutes at 37 °C.

Cell cytoskeleton morphology was visualized by F-actin staining with Phalloidin iFlour594 conjugate (23122, AAT Bioquest). 10 x 10 mm^2 center regions of 3D-printed gyroid constructs were cut using a scalpel, and rings with inner diameter of 18 mm fabricated from 2 mm sheets of PDMS were placed around the samples to create a well to reduce the amount of staining solution needed. The Phalloidin stock solution was diluted 1:1000 in PBS and added to cover the constructs fully. Following an incubation period of 60 minutes at 37 °C on an orbital shaker at 45 rpm, the samples were washed with PBS twice. In addition, cell nuclei were stained with 0.06% Hoechst 33342 (H3570, ThermoFisher Scientific) in PBS for 60 minutes at 37 °C on an orbital shaker at 45 rpm, followed by washing with PBS twice.

Cell Proliferation was monitored using 647 EdU Cell Proliferation Assay with Eterneon-Red 645 Azide dye (BCK-EdU647IM100, BD Biosciences). Bioprinted gyroid constructs were cultured for 11 days before fixation and imaging. The EdU solution was added on day 6 by removing half of the supernatant in the petri dish and adding the same amount of fresh medium for a final concentration of 10 µM EdU. After 11 days of culture, the 3D tissue models were fixed with 3.7% formaldehyde in PBS, embedded in Tissue-Tek O.C.T. Compound (4583, Sakura Finetek), and frozen at – 20 °C. Following cryosectioning (CM 1950, Leica Biosystems), the samples were permeabilized with 0.5% Triton X-100 and washed with 1 ml of 3% BSA in PBS twice. EdU detection was accomplished by adding 500 µl of reaction cocktail (prepared according to the manufacturer's instructions). Following incubation for 30 minutes at RT, the samples were washed with 1 ml of 3% BSA in PBS three times. In addition, cell nuclei were stained by treatment with 100 µl of 0.06% Hoechst 33342 in PBS for 15 minutes at RT.

4.6.3. Brightfield Microscopy

Large-scale brightfield images acquired to examine 3D-printed structures (i.e., for validation and optimization of printing parameters) were acquired using the Leica M165 C stereomicroscope equipped with the PLANAPO 0.63x objective.

5. Results & Discussion

5.1. Development of an mSLA bioprinter

Conventional desktop SLA 3D printers are capable machines offering sub-50 µm resolution but lack the necessary features for bioprinting. Temperature control is essential for the use of the most prevalent biomaterials in order to ensure suitable viscosities during printing, as well as for the inclusion of living cells into the printing process. Moreover, the temperature control increases the flexibility and reproducibility of the printing process. Conventional 3D printers are equipped with large metal printing platforms, whereas glass substrates are generally preferred for biological applications. The use of individually sized transparent glass substrates in our setup increases flexibility and avoids unnecessary post-processing steps, thereby reducing the risk of corrupting the sample during handling. The prints can be analyzed using high-resolution optical microscopy without first transferring them to a suitable substrate. In addition, the modified printing platform allows for the use of hydrogel volumes as small as 100 µl, which is essential if expensive or custom-made hydrogels are used as 3D printing resin.

To investigate the use of mSLA technology in bioprinting, a commercially available conventional desktop mSLA printer (Phrozen Sonic Mini 4K) was converted into a high-resolution 3D bioprinter using off-the-shelf hardware and custom-made 3D-printed components (**Figure 13**). This setup and its validation and parameter optimization using ECM-based hydrogels together with human bone marrow and cartilage cells represent the first documented application of mSLA technology to bioprinting and fills a knowledge gap as well as a gap in the existing literature. The conversion process involved integrating a temperature controller to maintain constant temperatures between 25 and 37 °C, facilitating the processing of ECM-based and cell-laden hydrogels. Additionally, a humidification strategy was implemented to prevent the evaporation of liquid from the hydrogel. An innovative build platform for attaching glass substrates was designed to streamline sample handling and integrate the printed tissue constructs into cell cultivation and microscopic analysis workflows.

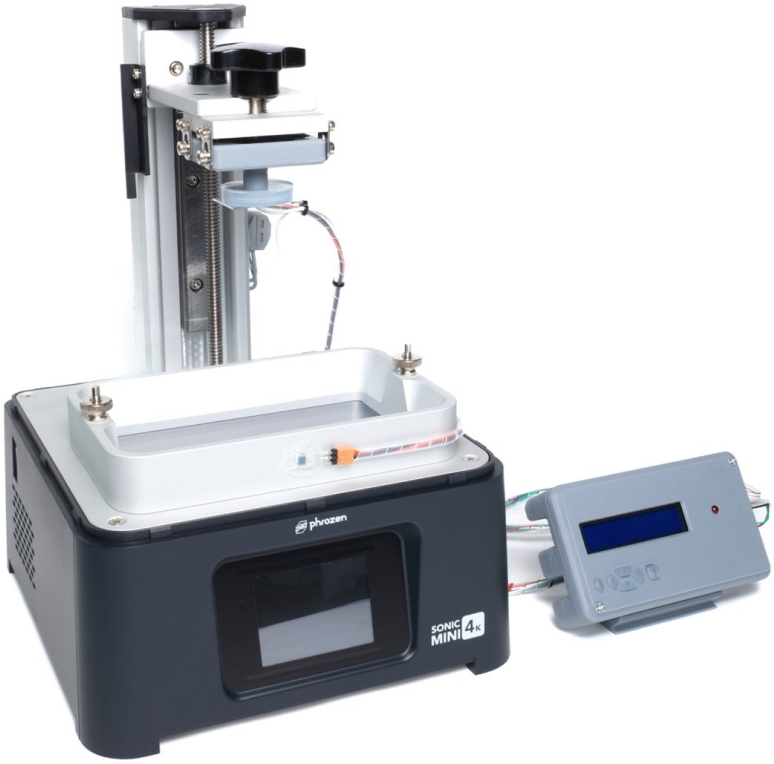

Figure 7: Modified mSLA bioprinter based on the Phrozen Sonic Mini 4K. (Image from Kaufmann et al. 2024)

To ensure the accessibility of mSLA-based bioprinting for potential users, the Phrozen Sonic Mini 4K Printer was selected as the basis for this project. This state-of-the-art consumer-level stereolithographic printer offers a 35 µm lateral (x, y) resolution and 405 nm lensed LED matrix illumination, making it an ideal candidate for high-resolution bioprinting (see **Table 1**).

Table 1. Phrozen Sonic Mini 4K technical specifications

Parameter	Set value
Layer height (z res)	10 – 300 µm
Pixel Size (xy res)	35 µm
Light source	ParaLED Matrix 2.0 (lensed LED matrix/array)
LED Wavelength	405 nm
Printing Display	6.1" monochrome 4K LCD, 3840 x 2160 px
Printer size	250 x 250 x 330 mm^3
Printer weight	5 kg
Max print volume	134 x 75 x 130 mm^3

The printer features robust construction with solid aluminum used for the z-axis, chassis base plate, and resin vat. It is controlled by a ChiTu Mainboard, a widely used controller in mSLA printers, ensuring compatibility with a variety of free-to-use and commercial slicing software. Phrozen is one of the market

leaders in mSLA printers and has consistently provided innovative solutions. By choosing this manufacturer, we anticipate benefiting from future advancements and innovations, leveraging their design as a solid basis for ongoing bioprinting developments. It is important to note that the concepts introduced to modify the printer are not manufacturer-specific and can be adapted to fit other printers and manufacturers, ensuring broader applicability and flexibility.

All modifications can be completed in less than two working days using lab-made 3D printed parts, standard tools, and widely available standardized components. All 3D printed parts were printed with the same Phrozen Sonic Mini 4K that was converted, eliminating the need for a separate 3D printer. The total cost of this bioprinter amounts to less than €500 […].

The modifications and additional equipment were kept to a minimum to simplify the setup process. Only essential new functions were integrated, including a temperature controller to maintain optimal conditions for ECM-based and cell-laden hydrogels and a humidification system to prevent evaporation. This approach ensures that the bioprinting platform remains user-friendly and accessible while still delivering the necessary capabilities for high-resolution bioprinting.

All necessary files for the mSLA to bioprinter conversion (mSLAb) have been published as open-source files on a publicly accessible repository [77]. This aims to enable the scientific community to participate in the platform's further development and benefit from ongoing revisions. The goal is to present a sustainable concept for converting a commercial mSLA platform into a bioprinter that can be easily adapted to future mSLA printer generations and designs. The intention of the open-access and open-source approach is to enable the widespread use of mSLAb in scientific research as well as educational projects.

5.1.1. Custom build platform for glass substrates

Like most conventional stereolithographic 3D printers, the Phrozen Mini 4K is equipped with a metal printing platform, large enough to use all pixels of the LCD. This approach is effective when using 200-300 ml of standard synthetic printing resin in the vat, particularly when printing large models for rapid prototyping. For biological and scientific applications, transparent glass substrates are generally preferred, comparatively small objects are printed, and only minimal material is to be used. To meet these requirements, the metal build

platform was replaced with a custom-designed 3D-printed build platform to enable the use of removable individually sized glass slides (**Figure 8**).

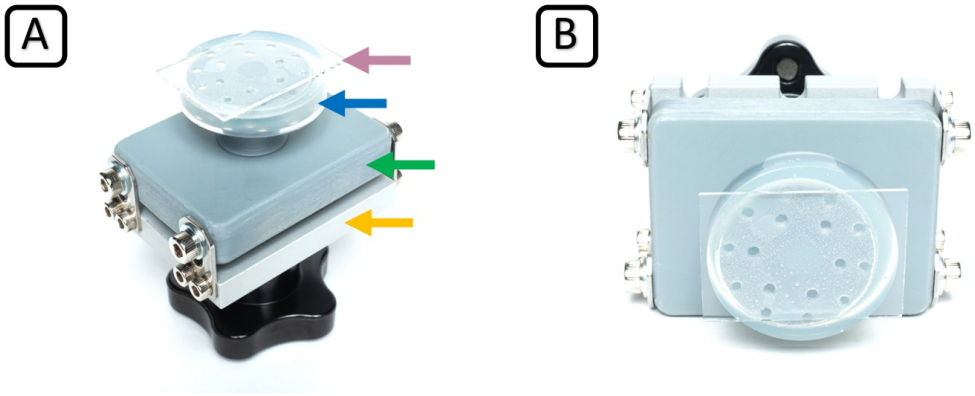

Figure 8: The custom-designed 3D-printed build platform. The custom-designed 3D-printed build platform (grey) with glass substrate (purple arrow). The silicone-encased build platform (blue arrow) and base plate (green arrow) are attached to the original attachment plate (orange arrow) in side view (A) and bottom view (B). (Images from Kaufmann et al. 2024)

The new build platform consists of a base plate (**Figure 8**, green arrow) that fits the original attachment plate of the printer (**Figure 8**, orange arrow) and a silicone-encased build platform (**Figure 8**, blue arrow). The printer's native semi-automatic z-axis leveling procedure is still supported by retaining the original attachment plate, ensuring level prints. The silicone-encased platform is exchangeable and can be customized to fit different sizes of glass substrates. Glass substrates can be attached to the silicone pad securely via suction force and removed easily. To validate the platform concept, standard 1 mm thick microscopy slides cut in half were used as substrates (**Figure 8**, purple arrow).

Replacing the factory metal platform with a custom-made 3D-printed platform that accommodates individually sized glass substrates offers multiple benefits. Utilizing standard microscopy slides or cover glasses with thicknesses of 1 mm and 170 µm, respectively, and printing directly onto these glass surfaces allows samples to be imaged with high-resolution optical microscopy with accurately corrected objectives while avoiding unnecessary sample manipulation. These substrates also do not interfere with the subsequent processing steps (e.g., washing or staining) and incubation in Petri dishes or multiwell plates. Moreover, the amount of material required for printing is greatly reduced due to the individually sized substrates. Typically, only 200-800 µl of fresh protein resin is used for individual experiments. Like an immersion liquid between the cover glass and the objective in microscopy, here, during printing, the droplet of resin used is confined by the surface tension between the resin, the LCD’s plastic film, and the surrounding air. By always utilizing fresh material,

such as functionalized proteinaceous hydrogels and cells, for individual experiments in minimal volumes, economical and reproducible light-based bioprinting can be achieved.

5.1.2. Temperature Controller and Humidification

In mSLA-based printing, the material has to be liquid to enable the layer-by-layer polymerization process. Printing is further improved by reduced viscosity because the process involves up and down movement of the build platform after each consecutive layer is cured to allow fresh resin to flow into the gap between the newly cured layer and the bottom of the vat. A lower-viscosity material will flow more easily and evenly, creating a consistent thin layer for the next exposure to light. This also helps to avoid defects in the constructs and cell damage caused by shear forces or air bubbles. [RO-12h-L] GelMA exists in a gelatinous state at room temperature, making it too viscous to be processed in the mSLA process. However, upon heating the material to 35 °C, it undergoes a phase transition to a liquid state with significantly reduced viscosity, making it suitable for printing. Therefore, in order to successfully print with GelMA, it is essential to modify the mSLA printer and include a temperature control for the printing chamber. Additionally, this feature offers the possibility for […] printing of hydrogels laden with living mammalian cells, which require an ambient temperature of 37 °C. However, the increase in temperature favors the evaporation of water from the GelMA, thus increasing its protein concentration. For consistent printing quality, the material properties should remain constant, and evaporation should be avoided by humidification.

To achieve reliable temperature control in the modified mSLA bioprinter, the high thermal capacity of the aluminum parts installed in the original printer was utilized. Two self-adhesive resistive heating pads (189149, Thermo Technologies), each with a power output of 12 Watts, were installed on the back of the z-axis (**Figure 9** B, blue arrows) of the printer and powered by a single n-type MOSFET (TO-220AB, Infineon Technologies) controlled by an Arduino Uno to heat the printer. Temperatures are measured by two high-accuracy (± 0.1 °C) pre-calibrated semiconductor temperature sensors (TSIC 506F TO92, Innovative Sensor Technology) placed on the front of the printer's material vat (**Figure 9** A, green arrow) and between the heating pads (**Figure 9** B, green arrow).

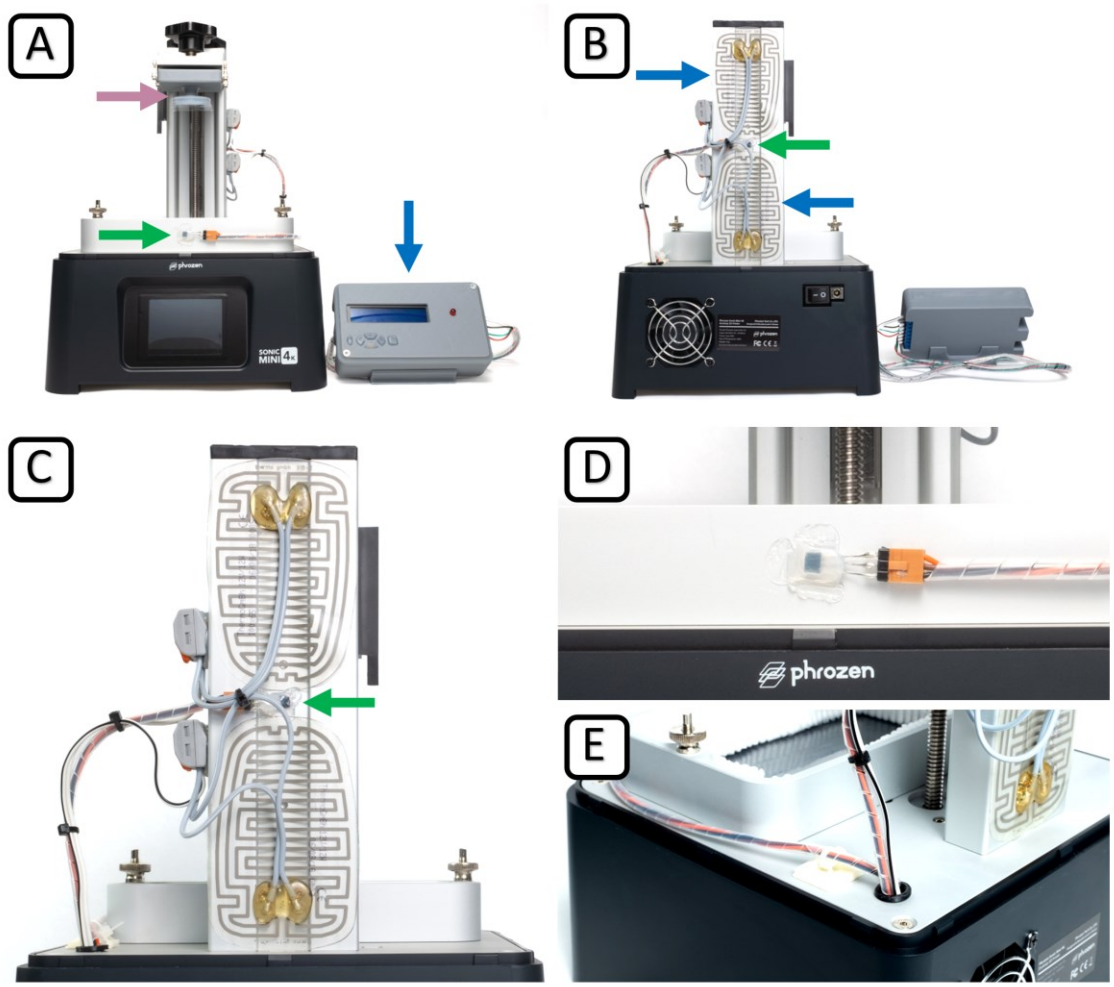

Figure 9: mSLA bioprinter with close-up views of the modifications. Front view (A) with temperature controller (blue arrow), custom-designed build platform with glass substrate (purple arrow), and vat temperature sensor (green arrow). Rear view (B) with heating elements (blue arrows) and z-axis temperature sensor (green arrow). Close-up views showing the placement of the heating pads, z-axis temperature sensor (green arrow) and wiring routing (C), vat temperature sensor placement (D), and cable grommet (E). (Images adapted Kaufmann et al. 2024)

The desired target temperature (25 – 37 °C) can be set using the keypad on the external Arduino-based temperature controller (**Figure 9** A, blue arrow), which then proceeds to heat the printer automatically. The LCD of the controller displays the current vat temperature and the target temperature. The temperature controller is pre-calibrated to standard laboratory conditions and may be recalibrated to different printer and heating pad combinations by following the instructions provided in the publication and commented code [1]. For minor changes, the controller menu offers the ability to set an offset in 0.1 °C increments to account for deviations without modifying the code. The wiring for the heating pads and sensors is routed through a 10 mm hole drilled into the aluminum chassis of the printer (**Figure 9** E) and out the bottom of the printer. The hole is lined with a 3D-printed grommet to protect the wiring and seal the

printer's circuit against moisture. **Figure 10** A shows the circuit schematic of the temperature controller with two semiconductor temperature sensors and the n-channel MOSFET to switch the power to the heating pads, connected to an Arduino Uno microcontroller with an LCD Keypad Shield as user interface. The perfboard with assembled circuit facilitates the connection of the Arduino microcontroller to the components fitted to the printer via screw terminals and pin sockets, respectively (**Figure 10** B). The LCD keypad shield is stacked on top of the Arduino Uno and, together with the perfboard, fits within a 3D-printed case adapted from an open-source design (**Figure 10** C).

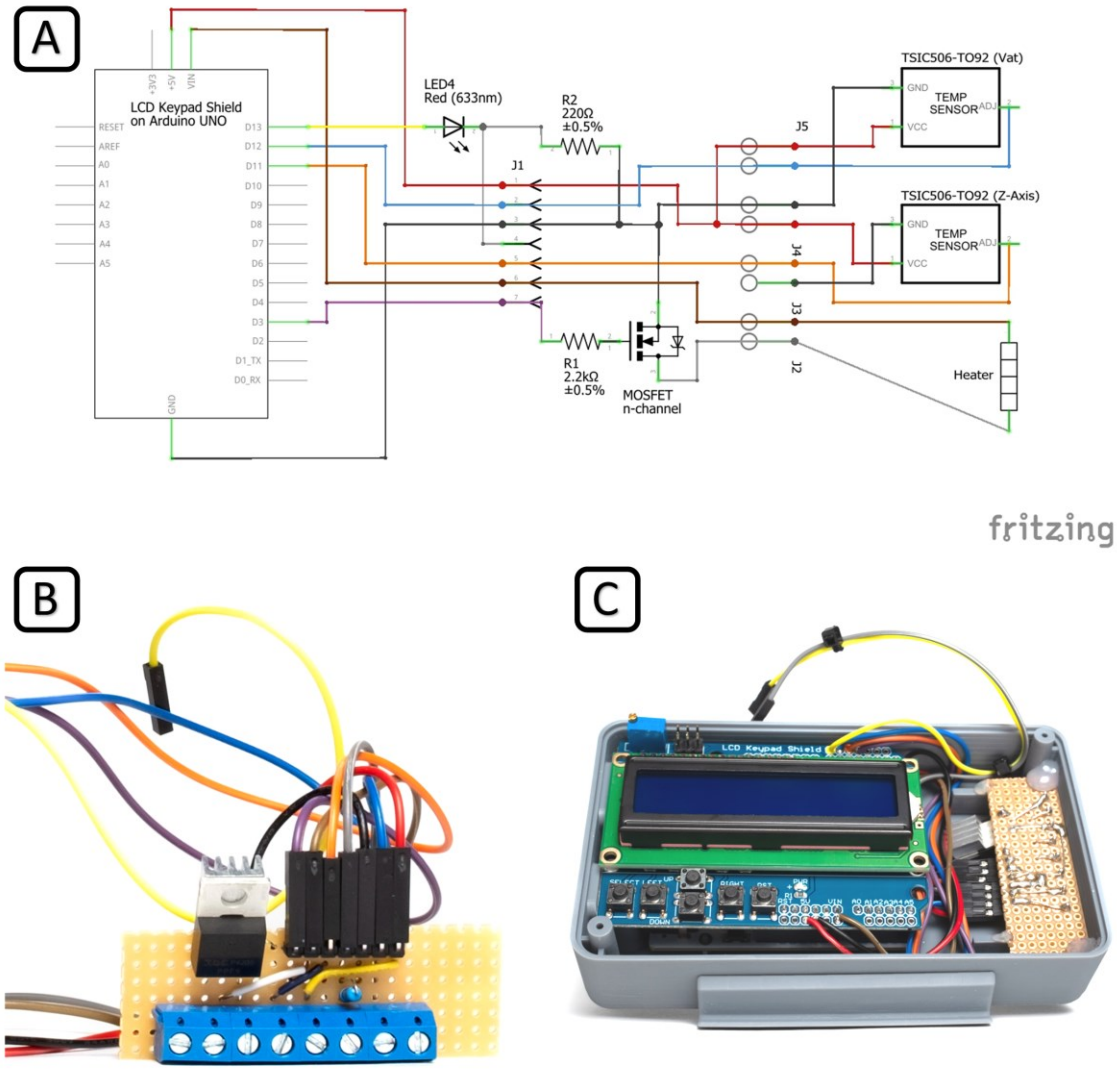

Figure 10: Temperature controller schematic. Circuit schematic of the temperature control module (A) and component layout on the perfboard (B). Arduino UNO with LCD Keypad Shield and the assembled perfboard, placed within the 3D-printed case of the temperature controller (C). (Images adapted from Kaufmann et al. 2024)

The print chamber was sealed to protect the electronics from water vapor and to isolate it from the airflow of the printer's integrated fan cooling system by

placing a custom-made silicone seal around the z-axis homing sensor. To further prevent water evaporation, the humidity in the printing chamber was increased to over 90% by lining the rim of the vat with wet sterile material with a high surface area (i.e., folded disposable surgical head caps) (refer to **Chapter 4.2** for details).

5.1.3. Validation of Temperature Controller and Humidification

Most GelMA derivates (e.g., RO-12h-L) exist in a gelatinous state at room temperature and only become suitable for printing when heated to 35 °C, requiring a temperature control system in the mSLA printer. This is crucial not only for printing GelMA but also for future applications involving hydrogels laden with living mammalian cells, which require an ambient temperature of 37 °C. However, increased temperature can lead to increased water evaporation from GelMA, affecting its protein concentration and material properties. Humidification is necessary to prevent evaporation and ensure consistent printing quality. This section aims to validate the system concerning temperature stability and humidification, presenting data on both temperature and humidity during representative printer operation.

To validate the temperature controller and humidification, the printer was set up for bioprinting and turned on, according to **Chapter 4.2**. In addition to data logging of the vat temperature sensor of the mSLAb printer, a separate temperature-compensated digital humidity sensor (DHT22/AM2303, EXP) was placed in between the resting position of the print platform and the resin vat to measure relative humidity during heat up as well as during and after simulated sample handling.

Figure 11 *shows the typical curve of temperature and humidity measured in the printing area. After about 80 min, the target temperature is almost reached, with a deviation of only about 0.5 °C. The humidity rises much faster, reaches nearly 100% after 30 min, and stabilizes at 93%, which is sufficient to prevent evaporation. After 99 min, the cover of the printer was removed for 30 s to simulate sample handling. Note that light exposure causes a temperature increase within the printing material (due to the exothermic nature of the polymerization reaction), which is why the temperature in the printing chamber is set to 35 °C, although a printing temperature of 37 °C is aimed for. The graph shows the negligible temporary impact of sample handling on the temperature curve. Both temperature and humidity remain almost constant during printing.*

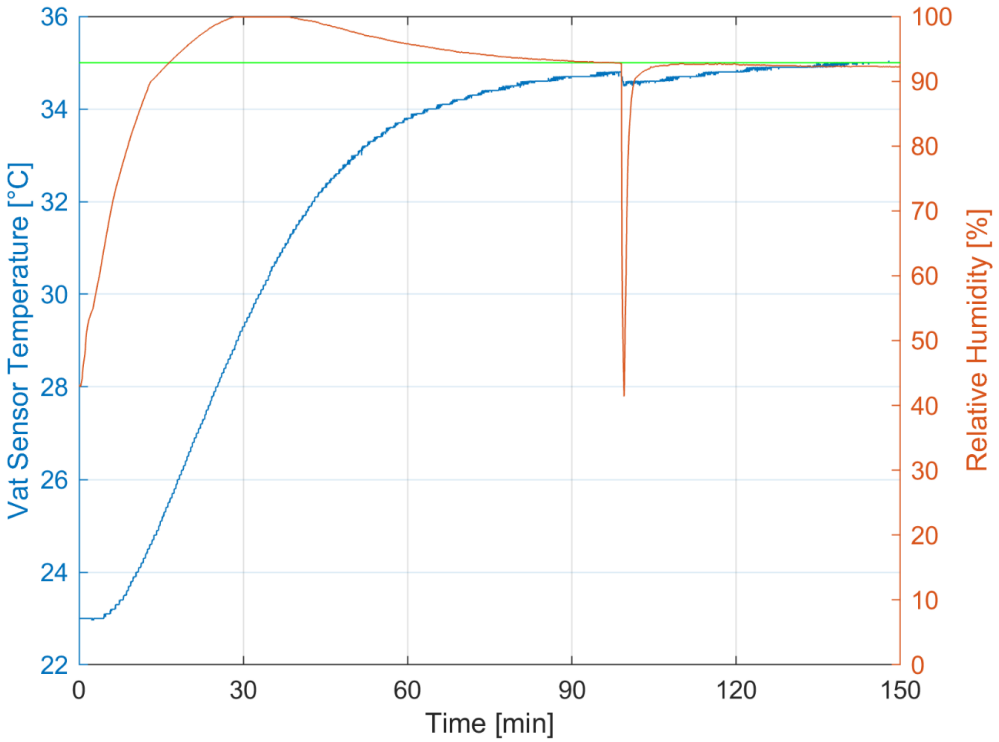

Figure 11: Temperature and Humidity Measurement. Exemplary temperature and humidity curve during the start-up of the bioprinter. Vat Sensor Temperature (blue), Relative Humidity (orange), and Temperature Set Value (green). The printer's top cover was removed for sample handling at 99 min. (Image from Kaufmann et al. 2024)

The temperature control system leverages the high thermal masses of the printer's aluminum chassis components (i.e., aluminum z-axis, chassis base plate, and resin vat) to ensure stable temperatures. This stability results in minimal deviations during sample handling. By eliminating the need for active fans, the system prevents air recirculation, which is crucial for maintaining the water content of hydrogels used in bioprinting. Preventing hydrogel evaporation is essential, as water loss increases viscosity and alters the concentration of hydrogel components such as photoinitiator and photoabsorber, thereby negatively impacting the printing performance and reproducibility. Sample handling has minimal effects on temperature and humidity in the printing chamber, with humidity recovering to above 90% within two minutes. This indicates high reproducibility of environmental conditions for successive prints.

5.1.4. Validation of Protein Resin Printability

Following the conversion of a conventional mSLA printer to a bioprinter and subsequent validation of the temperature controller, the mSLAb was validated for bioprinting, and suitable printing and material parameters were investigated. First, the technical specifications and potential changes from the Phrozen Sonic Mini 4K base model due to the bioprinter conversion were considered. Second, various 3D models relevant to tissue engineering were designed and printed to evaluate the print quality and suitability for bioprinting applications.

The conversion of the Phrozen mSLA printer for bioprinting applications does not affect the precision, resolution, and tolerances (=basic mechanical parameters) [of the printer] since the mechanics remain unchanged (see

***Table 1**). The final resolution or minimum feature size achieved in bioprinting depends on a variety of factors, including the material used (such as the capability to be crosslinked to a solid, polymerization/absorption characteristics, photoinitiator system, and viscosity) and the printing parameters chosen (such as exposure, z-layer height, movement speed, and print orientation).*

The first test model designed to evaluate the suitability and performance of the mSLAb system for the printing of ECM-based protein resins for tissue engineering applications was a gyroid structure with dimensions of 10 x 10 x 3 mm^3 (**Figure 12**). The gyroid structure features high porosity with interconnected channels, allowing for good diffusion of cell culture growth media, metabolites, and oxygen within the printed construct (refer to **Chapter 4.2** for details on the gyroid model). In later experiments, the use of gyroid models combined with cells directly integrated into the printing process was explored (refer to **Chapter 5.3**). Gyroid samples were printed at 100 µm z-resolution using 800 µl of protein resin containing 15% RO-12h-L, 0.6% LAP and 0.06% QY.

Figure 12 shows a 3D rendering of this gyroid model in an isometric overview (A) and a close-up of the top surface (B). The respective 3D-printed GelMA construct closely resembles the geometry of the CAD model and presents clearly distinguishable layer transitions (**Figure 12** C and D). This print demonstrates the capability to produce arbitrary 3D geometries with overhangs and hollow channels, showcasing a substantial advancement in the projection-based printing of protein materials. Unlike many existing studies that primarily focus on 2.5D features (i.e., stacked layers without hollow structures), our approach successfully achieves complex, fully three-dimensional

constructs. The successful generation of these intricate 3D models using ECM-based protein resin underscores the potential for advanced bioprinting applications, paving the way for innovative tissue engineering solutions.

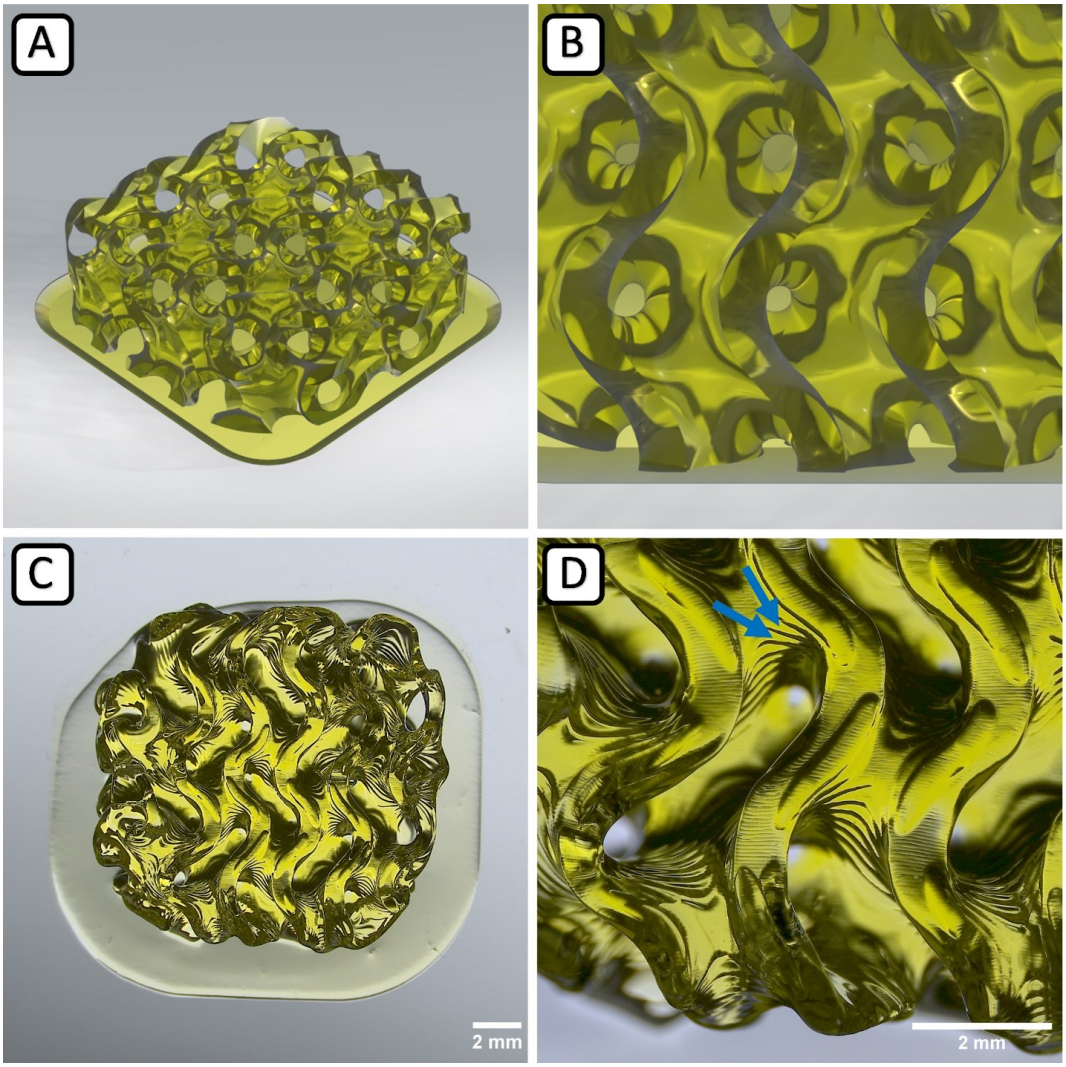

Figure 12: Macroscopic gyroid scaffold. Rendered image (CAD) in isometric view (A) and close-up (B). Microscopy image of the printed scaffold using GelMA hydrogel in overview (C) and close-up (D) with visibly resolved z-layers (D, blue arrows). (Images from Kaufmann et al. 2024)

Vascularization is a critical challenge in tissue engineering, particularly for the development of larger tissue equivalents that contain living cells [96]. Without an adequate vascular network, these constructs cannot be supplied with nutrients and oxygen, nor can they effectively remove waste products solely through passive diffusion in culture media within the printed material [97]. This limitation hinders the viability and functionality of engineered tissues, making the creation of vascular structures or other perfusable channels essential for advancing the field[98].

To investigate the feasibility of printing complex vascular structures, a 3D hollow tube model was designed and printed using ECM-based protein resin. The samples were printed at 100 µm z-resolution using 800 µl of protein resin containing 15% RO-12h-L, 0.6% LAP, and 0.06% QY. These settings and material composition were identical to those used for the gyroid model, demonstrating the flexible process window of the mSLAb in combination with protein resins. **Figure 13** A and B show 3D renderings of the CAD model used to print a hollow tube in top and isometric view. This simplified vascular model features a sinusoidal bend to investigate the capability to print arbitrary 3D features that can be perfused. The close-up view in **Figure 13** C reveals the sharp z-layering of the wall structure surrounding the hollow channel. The mechanical stability of the tube construct is sufficient to allow the insertion of a cannula and perfusion with liquid, confirming that the channel is open and perfusable (**Figure 13** D and E).

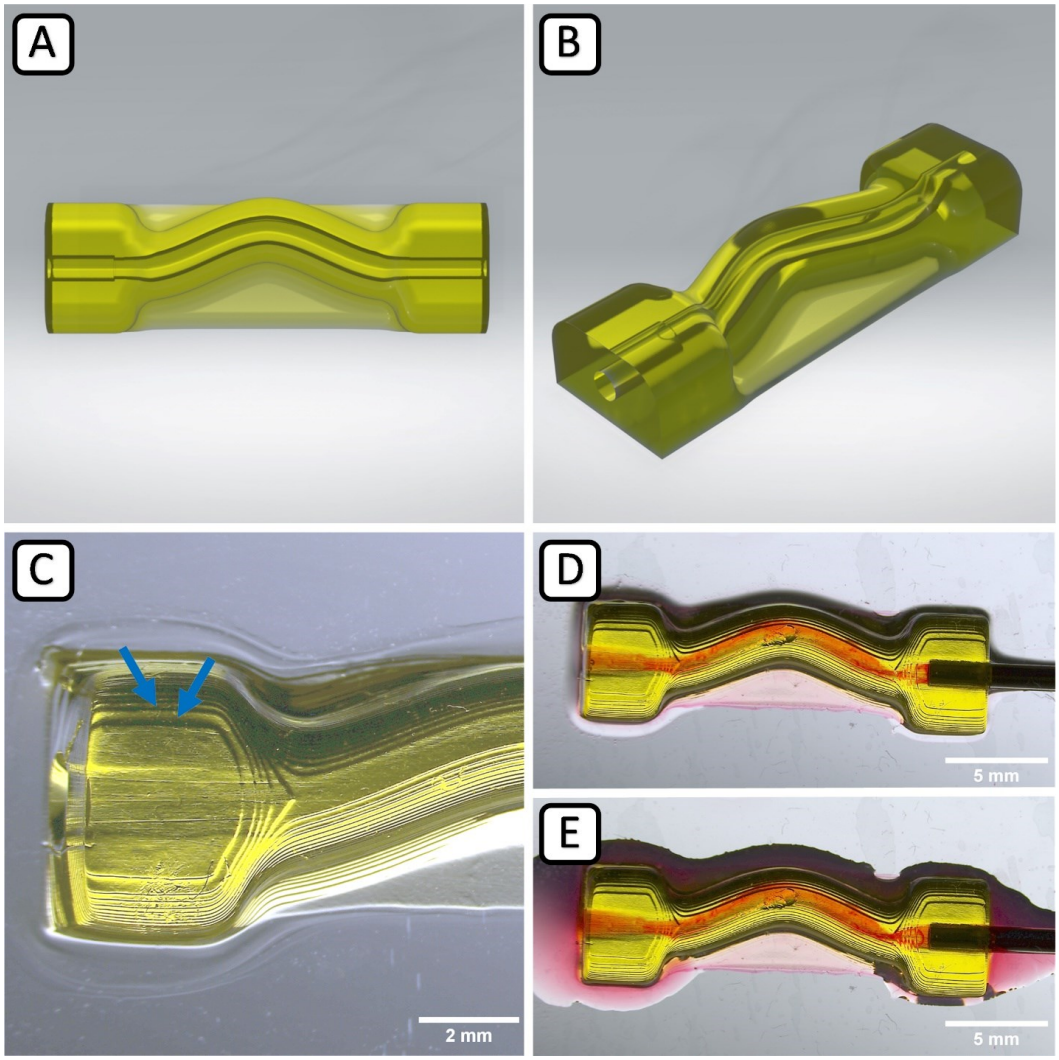

Figure 13: Perfusable channel construct. Rendered image (CAD) in overview (A) and isometric view (B). Microscopy image of the printed channel construct using GelMA hydrogel in overview (C) with visibly resolved z-layers (C, blue arrows) and during perfusion with red food dye using a blunt tip syringe needle (D, E). (Images from Kaufmann et al. 2024)

Most traditional 3D printing approaches in tissue engineering, such as extrusion-based systems, are limited to the production of single continuous tubes by co-axial extrusion or the use of sacrificial materials to print straight/planar tubes [99-101]. In comparison, mSLAb offers true 3D structuring capability using ECM-based material without the need for sacrificial materials or support baths. The results suggest that mSLAb provides an effective platform for future experiments aimed at integrating vascular networks into tissue-engineered constructs.

To further investigate the versatility of the newly developed printing platform, experiments were conducted using a second formulation of GelMA (GM10). These experiments aimed to investigate the platform's resolution and its ability to print larger-scale models exceeding 1 cm^3. GM10 was chosen due to its higher degree of functionalization, which results in increased crosslinking and, thus, greater stiffness when compared to the RO-12h-L derivate. This property is advantageous for creating robust and stable scaffolds. Furthermore, GM10 has been shown to achieve varying degrees of stiffness depending on the cumulative exposure, as well as good cytocompatibility [16]. This variability in stiffness is particularly interesting as it may serve as a mechanical stimulus for cells, influencing their migration, differentiation, and overall behavior within the scaffold in future experiments. The prints conducted using a protein resin formulation of 20% GM10, 0.6% LAP, and 0.06% QY demonstrate the wide process window in terms of the material composition and printer, enabling both small, intricate designs and larger structures with consistent quality.

Figure 14 A and B shows a larger-scale scaffold design consisting of square profile beams (500 x 500 µm) stacked orthogonally, forming a structure measuring 10 x 10 x 10 mm^3 on an adhesion platform (15 x 15 mm^2). This design was chosen to investigate the printer's capability to construct detailed and sizable 3D models. The high wetting properties of the scaffold structure, as shown in **Figure 14** C-F, are ideal for subsequent cell seeding and the diffusion of nutrients throughout the structure during cultivation. **Figure 14** G and H provide a top view of the scaffold, with alternating beams and hollow spaces clearly visible. The variation in focus depth from the top (G) to the bottom (H) illustrates the three-dimensionality of this comparably high structure and the uniformity of the beams throughout the construct. This level of detail and precision underscores the printer's ability to produce high-resolution, large-scale scaffolds suitable for advanced tissue engineering applications.

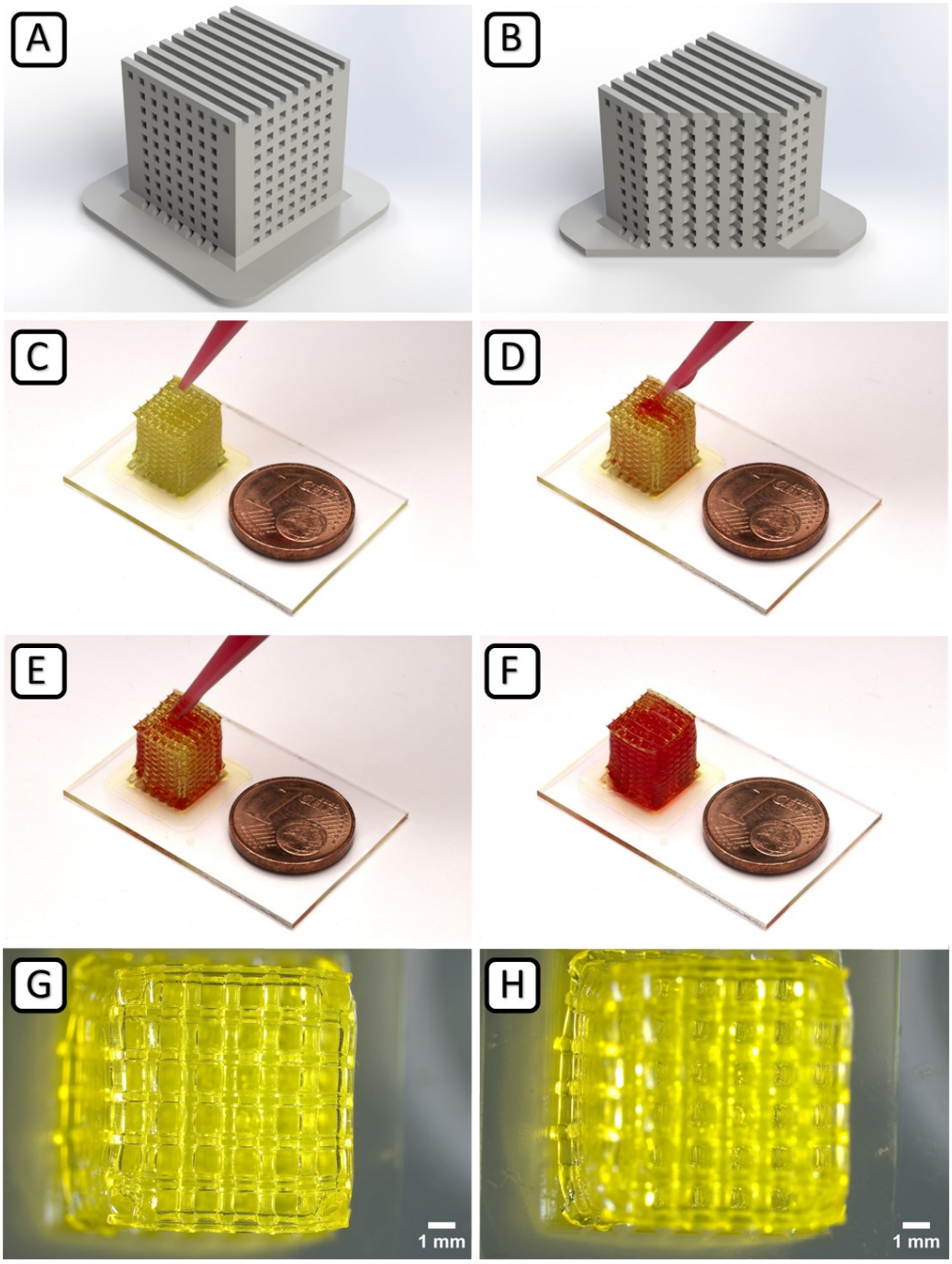

Figure 14: Complex orthogonal line scaffold. Complex orthogonal line scaffold (10 x 10 x 10 mm^3) 3D printed on mSLAb with GM10 biomaterial. Rendered image (CAD) in isometric view (A) and cut view to visualize internal features (B). Photography images demonstrate the internal structure's excellent wetting properties, which are essential for subsequent cell seeding and cultivation in tissue engineering (C-F). Microscopy images showing the alternating beams and hollow spaces with varied focus on the top (G) and bottom (H) layers demonstrate that the lattice structure has been realized throughout the entire construct. (Images from Kaufmann et al. 2024)

To further investigate the capabilities of the printing platform, experiments were conducted to print an array of sinusoidal lines with a width of less than 100 µm on an adhesion platform measuring 15 x 15 x 0.5 mm³. **Figure 15** features an array of nine 3D sinusoidal lines printed without defects. Each line has an average width of less than 2 pixels, which is nearly independent of orientation. The individual pixels are visible within the flat adhesion platform, highlighting the printer's resolution capabilities. The average width of the sinusoidal lines measured in this print was 52.38 µm, with a standard deviation of 5.69 µm. The width was measured using ImageJ (Fiji Distribution) and the InteredgeDistance Macro, which utilizes two splines drawn along the edges of the lines in the microscopy image (**Figure 15** D). The distance between the edges was measured at 97 equidistant locations along the splines. This experiment aimed to demonstrate the printer's precision in creating fine, consistent patterns that are crucial for applications requiring high-resolution structures. Such precision is essential for applications in tissue engineering, where the microarchitecture of scaffolds can significantly influence cell behavior and tissue formation [102-104].

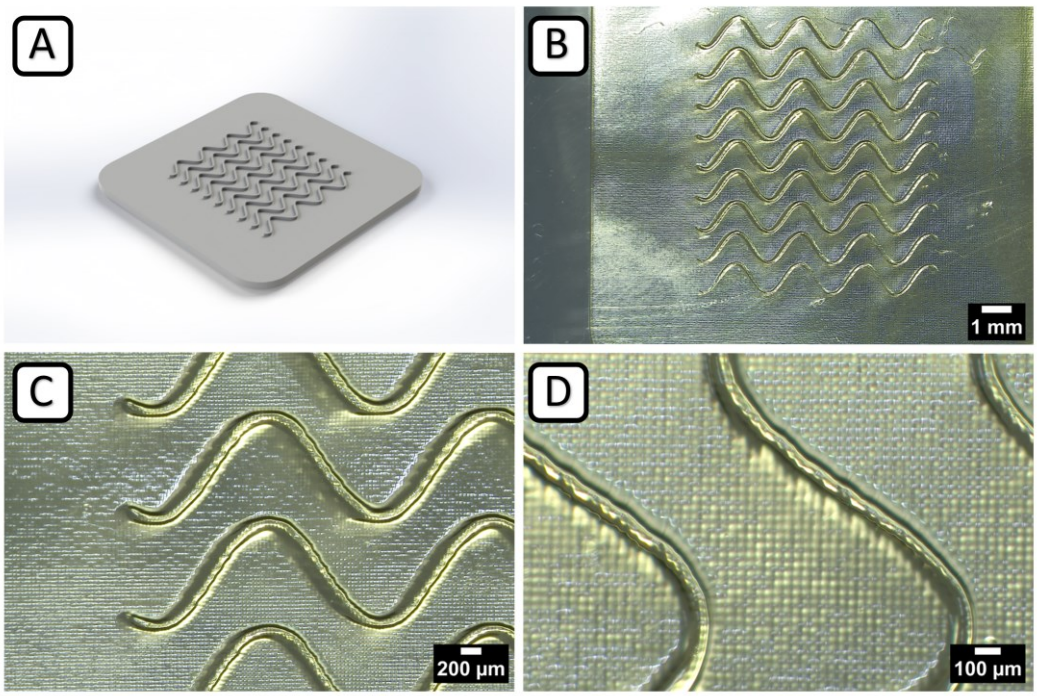

Figure 15: Sinusoidal Line Array: Sinusoidal Line Array 3D printed on mSLAb with GM10 biomaterial. Rendered image (CAD) in isometric view (A). Microscopy images with different degrees of magnification of the structures printed on the mSLAb with GM10 material (B-D). Note the fully formed 3D sinusoidal lines with a mean 52.38 µm width. The pixel size is visible inside the flat adhesion platform, especially at higher magnifications (C-D). (Images from Kaufmann et al. 2024)

5.1.5. Application of the mSLAb concept to a new printer

Following the successful conversion of a 3D printer to a bioprinter, as detailed in the previous chapter, the modular concept was further examined through its application to a next-generation printer. This chapter outlines the specific modifications made to the new printer model, demonstrating the adaptability and versatility of the mSLAb concept.

The Phrozen Sonic Mini 8K MSLA 3D printer's main advantage is the improved pixel resolution of 22 x 22 µm² compared to the 35 x 35 µm² of the previous 4K model. The light source was redesigned from a 4 x 6 LED array with individual lenses to a central Chip on Board LED design called the "Linear Projection LED Module," which utilizes a single lens. This new design offers a more uniform light distribution, and the intensity was increased, resulting in slightly shorter exposure times needed for successful printing. The mechanical setup closely resembles the old (4K) model, and only minor design changes were required to adapt the parts for the conversion to a bioprinter. **Figure 16** shows the 8K printer converted using the mSLAb concept in front (A) and rear view (B). The placement of the temperature sensors, one on the front of the material vat and one between the heaters on the z-axis is analogous to the converted 4K printer.

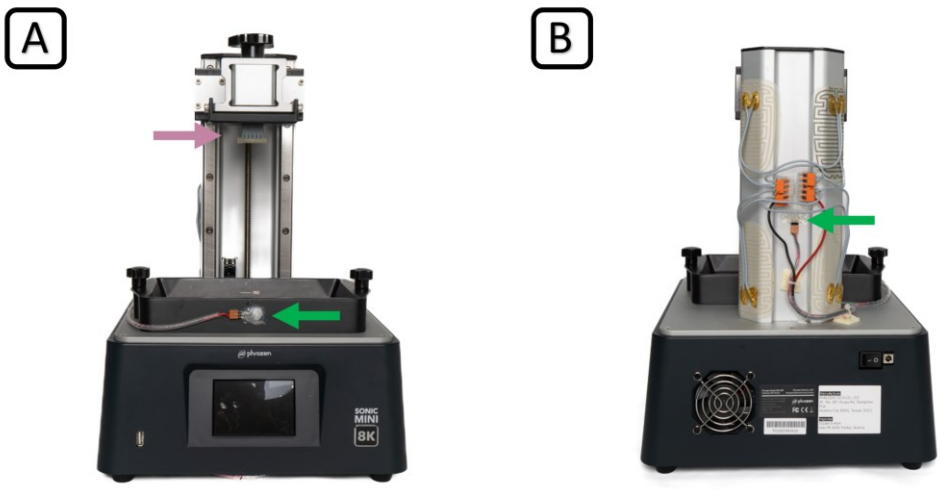

Figure 16: mSLAb 8K variant. mSLAb modified Phrozen Sonic Mini 8K printer in front (A) and rear view (B). Green arrows mark the temperature sensor placement on the front of the material vat and in the middle of the resistive heating pads on the back of the aluminum z-axis.

The 8K model features a larger aluminum z-axis, which makes it possible to fit four instead of two heating pads, reducing heat-up times and further improving temperature stability. The electrical circuit was adjusted to handle the

increased power consumption from the additional heating pads, highlighted in **Figure 17**. By adding a separate power connector, the current used by the MOSFET to switch the heating pads is no longer routed over the circuit board of the microcontroller.

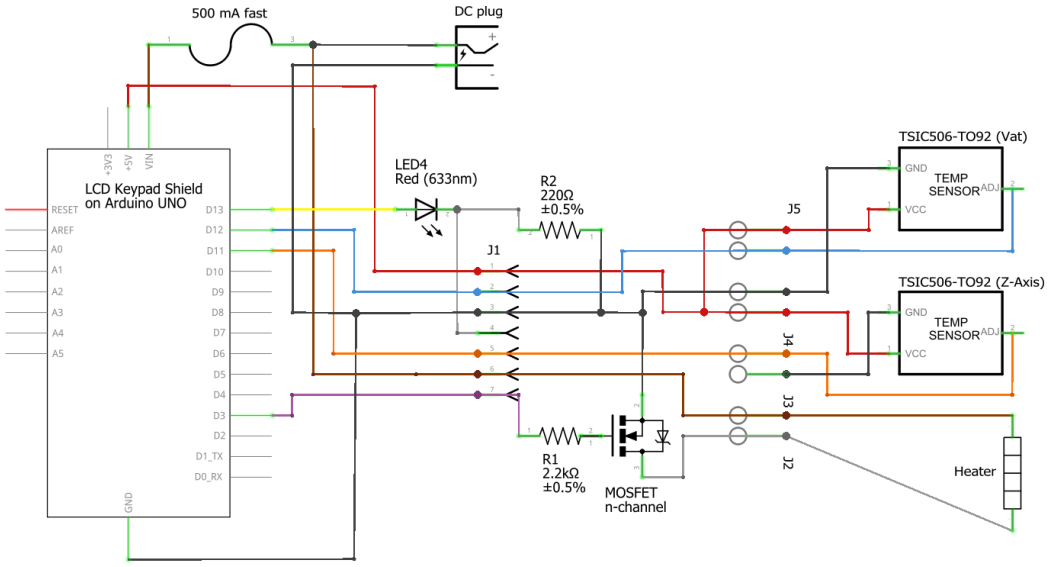

Figure 17: Updated Circuit Schematic. Circuit schematic for the temperature controller for the 8K variant of the mSLAb printer. A separate DC plug was added to handle the increased power consumption from the additional heating pads.

The temperature controller was calibrated as described in the code published in Kaufmann et al. to account for the new temperature gradient from the heating pads to the printing location. The base plate of the 3D-printed build platform was modified to fit the new original attachment plate of the 8K printer. The silicone-encased build platform's design was improved by adding a second fixation screw to prevent undesired rotational movement (**Figure 18** A). The molding stand was revised from an adjustable height design to a fixed one, ensuring homogenously 1.5 mm thick and planar silicone padding, see **Figure 18**. The 3D printed Petri dish for the molding process was revised to include a diagonal protrusion that will result in a semicircle profile groove with a 500 µm radius in the silicone to reduce the adhesion of glass substrates and ease the removal when used with thin and comparably brittle 170 µm thick glass coverslips as substrates (**Figure 18** C). Using glass coverslips as substrates enables high-resolution microscopy with objectives corrected for a thickness of 170 µm and generally increases usable working distance with inverted microscopes.

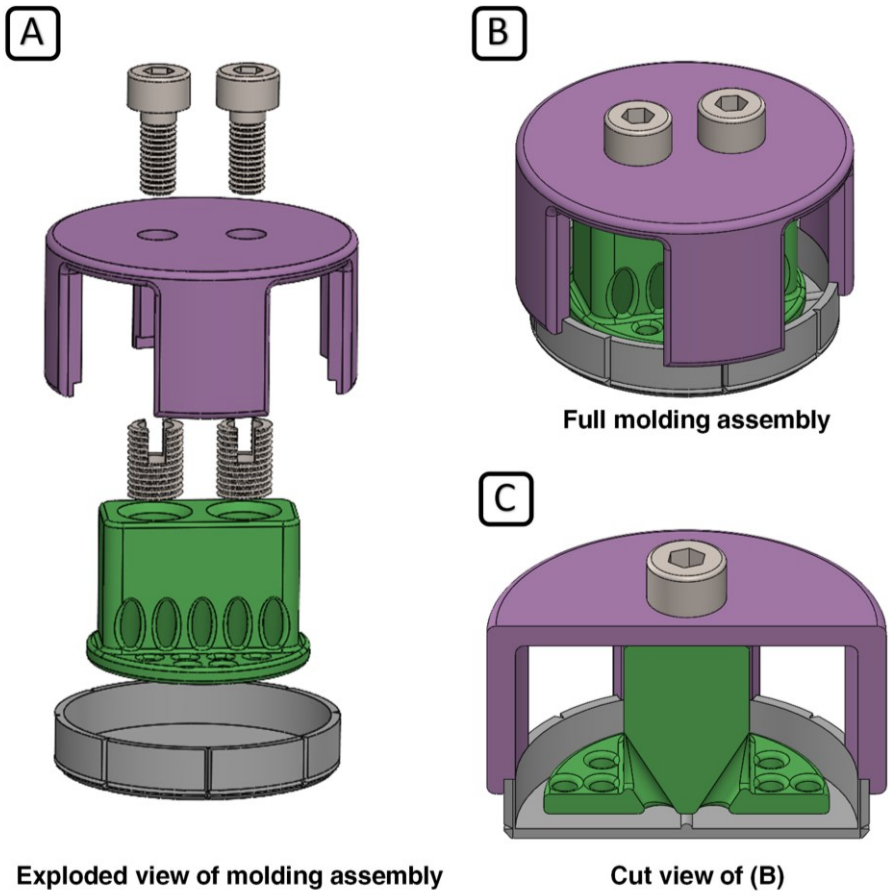

Figure 18: 8K build platform molding assembly. Detailed exploded view of the build platform modified for the Phrozen Sonic Mini 8K printer (A), the complete molding assembly (B), and section view of "B" (C) including the positions of the thread inserts and screws.

Figure 19 shows the fully assembled build platform, now including a 3D-printable attachment plate that can substitute the original part (grey). Having a fully printable build platform enables the stocking of multiple platforms, facilitating faster sample changes and the ability to easily switch between different platform designs if necessary.

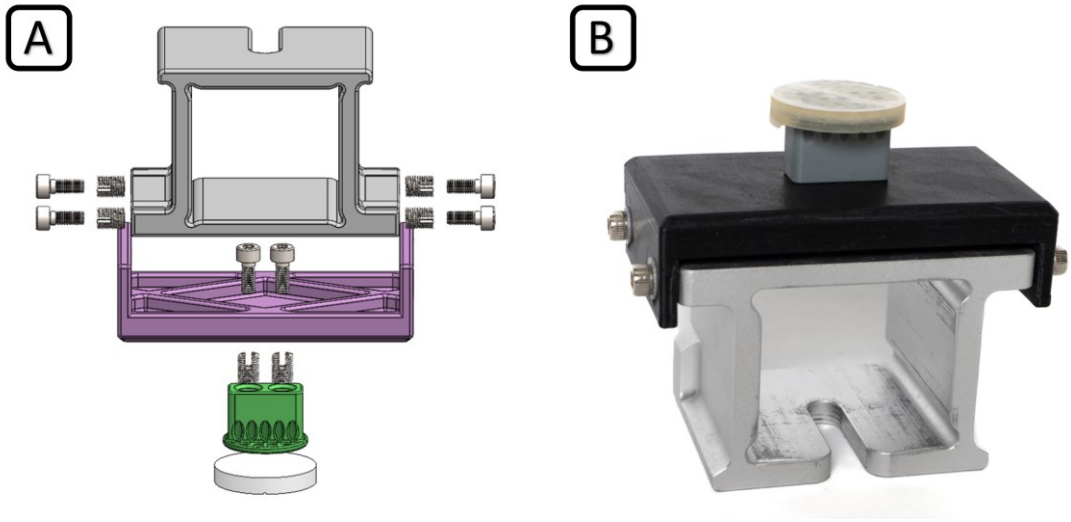

Figure 19: Updated version of the build platform. The custom-designed 3D-printed build platform was modified to fit the Phrozen Sonic Mini 8K printer. Exploded view of the CAD assembly, including threaded inserts and screws to fix the individual parts (A). Fully assembled build platform including mounted glass substrate (170 µm thick coverslip) on the silicone-coated platform (B).

The design of the 8K version of the printer simplifies wire routing compared to the 4K variant, eliminating the need for drilling a hole in the chassis. The wiring for the sensors and heating pads can be routed through the existing hole intended for the z-axis homing sensor. Additionally, thanks to the new design of the homing sensor, a silicon seal is no longer necessary, as the extra wires for the sensors and heating pads provide adequate sealing for the hole.

The modifications to the 8K version of the mSLAb printer were validated analogously to those of the 4K version. **Figure 20** displays an exemplary gyroid structure printed using the 8K version of mSLAb for validation, utilizing a protein resin composed of 16.67% GM10, 0.67% LAP, and 0.5 QY. The gyroid model, presented in **Figure 20** A and B in the top and close-up side view, was adjusted to a lamella thickness of 240 µm to showcase the printing of even finer features compared to the 4K model. The print maintains high fidelity, even at the edges of the structure. Moreover, this print was specifically selected to investigate potential printing artifacts, which can be seen in the printed construct's middle and lower left adhesion plate. These minor artifacts may occur due to accidental pipetting of bubbles when placing the protein resin droplet into the printer’s vat and should be avoided. **Figure 20** D illustrates the well-defined layer structure with fine details extending to the topmost layer, which corresponds to the tips of the structure visible in the side view (**Figure 20** B).

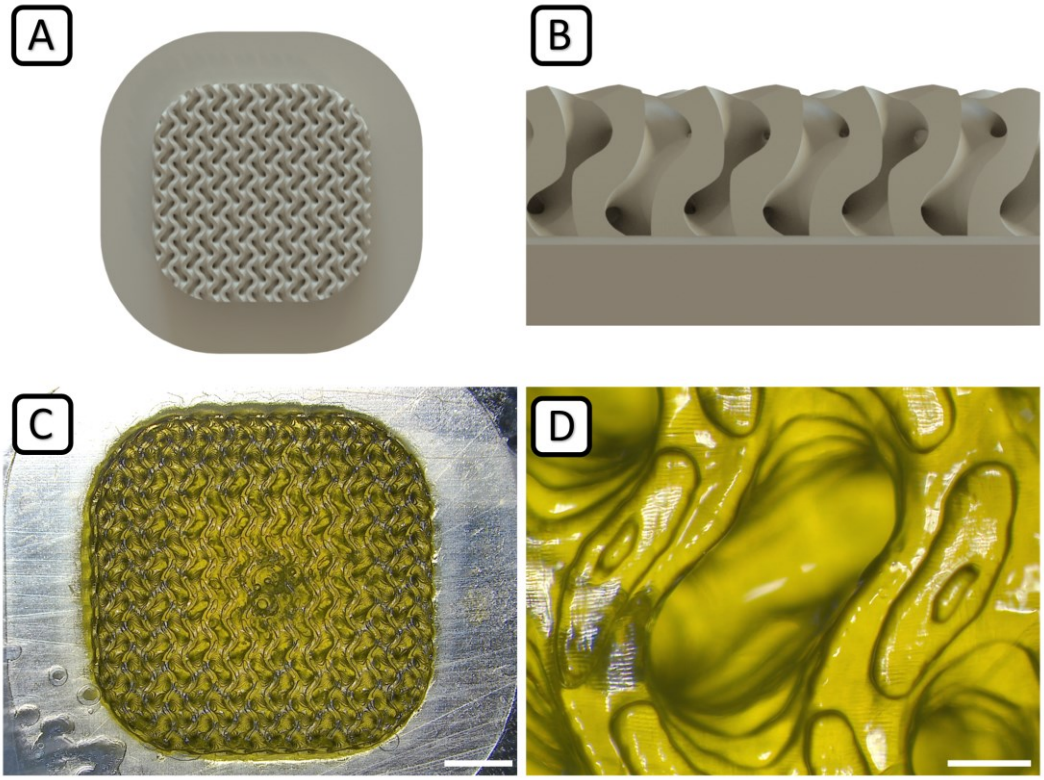

Figure 20: Gyroid Scaffold printed with the 8K version of mSLAb. Exemplary gyroid structure for the validation of the 8K version of mSLAb. 3D rendering in the top (A) and close-up side view (B) and printed structure in the top (C) and close-up top view (D). The gyroid structure was printed with 16.67% GM10, 0.67% LAP, and 0.5 QY on the 8K mSLAb. Scale bars, 2 mm (C) and 200 µm (D).

The successful adaptation of the concept to the next-generation printer further validates the initial design concept, demonstrating its applicability to newer and more advanced printer models.

5.2. Printing Parameter Optimization

Investigating and optimizing printing parameters is crucial for achieving high-resolution and structurally stable constructs in stereolithographic 3D printing processes. Key challenges include fine-tuning exposure time and photoabsorber (PhA) concentrations to attain the desired z-resolutions, which is essential for fabricating complex geometries such as overhangs and hollow structures. The precise PhA concentration required can vary depending on the printed model's specific geometry, influencing the final construct's fidelity and quality.

Benchmark structures based on the gyroid model were utilized to optimize the process of printing biomimetic scaffolds for tissue engineering. The gyroid model, known for its intricate and interconnected porous architecture, serves as

an ideal template for establishing optimal printing parameters. This model's complexity necessitates careful calibration of exposure times and PhA concentrations to ensure accurate replication of its features.

Exposure times were determined empirically by systematically varying the exposure until the 3D model was printed entirely and with sharp features. The optimal parameters were identified when further increases in exposure did not enhance print fidelity. Overexposure was carefully avoided to preserve resolution and minimize printing time and potential oxidative stress on cells, which can result from excess free radical production during the printing process. Once the ideal exposure times for multiple layer heights were established, these values were used to approximate exposure times for different layer heights through linear inter- and extrapolation. The specific exposure times used for the prints are detailed in the results, refer to **Table 2**. The PhI (LAP) concentration was investigated and optimized for cell compatibility in **Chapter 5.3.2**.

5.2.1. Photoabsorber Concentration

Optimizing the PhA, concentration is crucial for achieving high-fidelity prints with stereolithographic processes. In this study, the food dye quinoline yellow (QY) was used as a PhA. Here again, the gyroid model, known for its intricate and interconnected porous architecture, was used as a benchmark structure to determine the ideal QY concentration for printing with GelMA. Gyroid models were printed and post-processed by washing away unpolymerized GelMA and carefully drying the structures with filtered compressed air to allow high-contrast imaging using a stereomicroscope. An ideal process window regarding QY concentration was determined empirically by counting the discernible layers from the topmost gyroid structure crossing downwards. The goal was to set the QY concentration so that a maximum number of individual layers was clearly visible.

Figure 21 shows a 3D rendering of the gyroid model used as a benchmark structure (A), an exemplary microscopic image of a printed gyroid structure (B), and a close-up of the gyroid lamellae crossing features marked by arrows where the individual layers were counted (C) printed with 16.67% RO-12h-L, 0.67% LAP, 0.050% QY, and 18s exposure at 50 µm layer height. Detailed stereomicroscopic imaging allowed for the accurate evaluation of the printed structures.

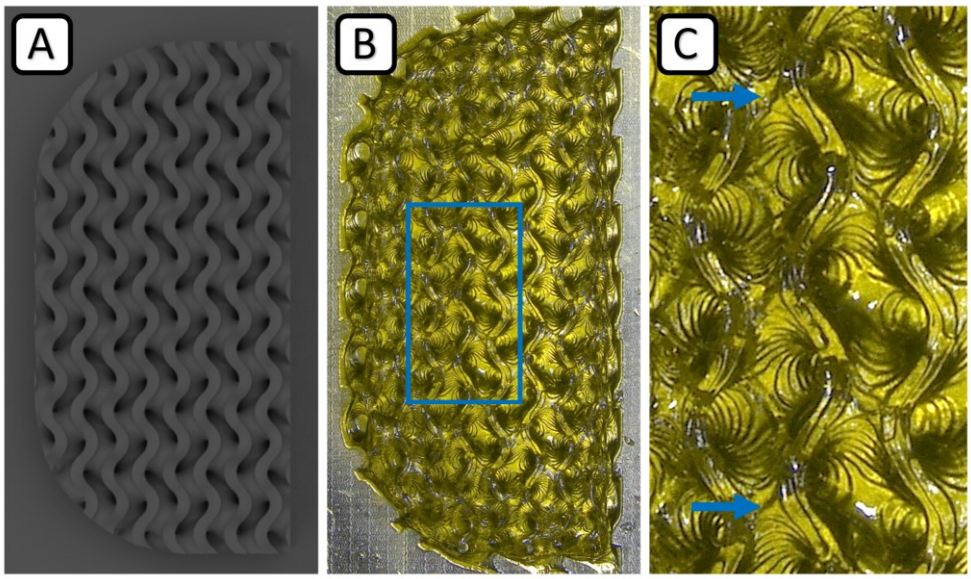

Figure 21: Photoabsorber concentration optimization. The gyroid model was used as a benchmark structure to determine the ideal quinoline yellow (QY) photoabsorber concentration by systematically varying the QY concentration and determining print fidelity using microscopy. Gyroid benchmark structure as 3D rendering (A) and exemplary benchmark printed with 16.67% RO-12h-L with 0.050% LAP and 18 s exposure at 50 µm layer height in overview (B) and a close-up of the structure to determine discernible layers, counting down from gyroid lamellae crossing points (C, blue arrows).

To illustrate the optimization process, **Figure 22** shows an exemplary plot of counted visible layers for a material composition of printing of 16.67% RO-12h-L and 0.67% LAP, with 18 s exposure time at 50 µm layer height. The QY concentration was first varied between 0.04% and 0.08% in 0.01% increments. After this initial assessment, the effect of QY concentration was subsequently examined closer between 0.05% and 0.06% revealing an optimal process window between 0.050% and 0.055% QY. This range provided the highest number of clearly visible layers, indicating the best print fidelity. Ideal QY concentrations were determined empirically analogous to this example for other material compositions.

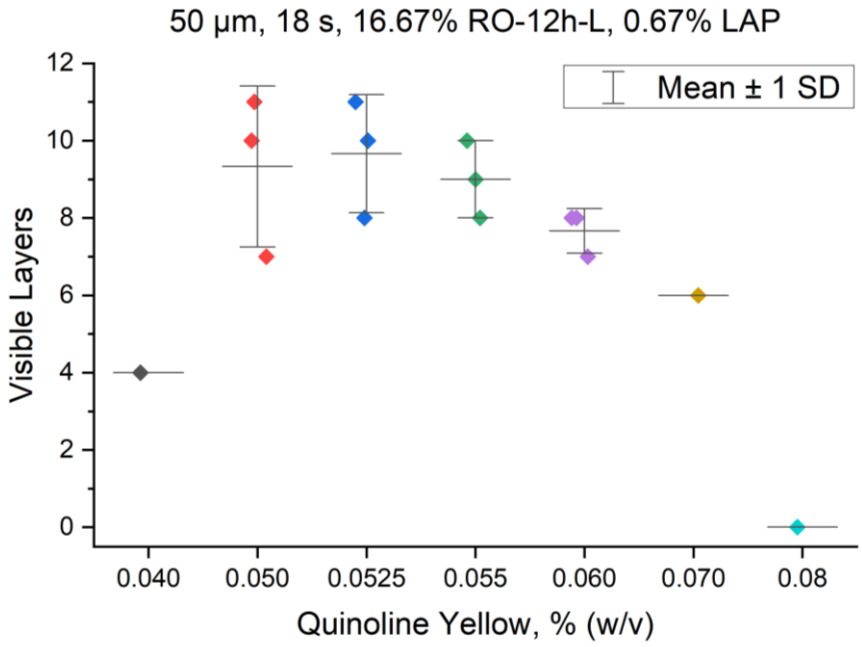

Figure 22: Plot of the visible layers as a function of the quinoline yellow concentration. An exemplary plot of clearly discernible individual layers (i.e., "visible layers) in dependence on photoabsorber (i.e., quinoline yellow) concentration for printing with 16.67% RO-12h-L with 0.67% LAP and 18s exposure at 50 µm layer height.

5.2.2. Dark Polymerization

The complex interaction between all printing process variables, including the concentrations of GelMA (polymer), LAP (photoinitiator), and QY (photoabsorber), as well as the exposure time, becomes even more evident when additional printing parameters are considered. The user can determine waiting times before and after exposure when slicing the 3D model in preparation for the print. Waiting times before the exposure may be used to reduce material flow and mechanical vibrations during polymerization due to build platform movement. Waiting time after exposure is used to wait for further polymerization due to prolonged radical chain reaction even in the absence of further excitation by light and is usually set in the 1-2 s range.

A review of multiple studies on the polymerization process of photosensitive hydrogels revealed an initial lag period during illumination where no significant increase in stiffness is measured, followed by an exponential rise and an asymptotic approach to final stiffness [18, 27, 29, 47, 105]. This phenomenon is explained by the initial crosslinking of mono- and oligomers, which does not significantly increase stiffness until a threshold of interconnection is reached. Interestingly, it was found that samples with substantially reduced exposure times can achieve similar final stiffness after extended waiting periods [106]. The final stiffness of samples is significantly decreased only when exposure times fall below a material composition-specific threshold. To determine if the effect

of dark polymerization can be leveraged in bioprinting to reduce exposure times and minimize the generation of unnecessary free radicals, a series of prints was conducted with systematically reduced exposure times and increased waiting times after individual layer illumination. Results showed that by increasing the waiting time after exposure from 1 s to 60 s, the exposure time could be reduced by approximately 50% (i.e., from 22 s to 12 s) while simultaneously decreasing the amount of photoinitiator used from 0.67% to 0.15% LAP while retaining good print fidelity. Good x, y, and z-resolution can be achieved by carefully optimizing exposure time and QY concentration. Optimizing the printing parameters to print sharp features and reducing overexposure to yield good printability of overhanging features and hollow structures of the gyroid model resulted in slight undersizing of x and y features using GelMA-based resins. Other groups found similar results. They seem to be typical for projection-based 3D printing, even if commercially available synthetic resins are used [107]. Notably, the prints conducted with dark polymerization using mSLAb exhibited extensive x and y-deviations. To determine the dependency of the deviation for the GelMA-based protein resins used in this study, the gyroid model's features were scaled in 100 µm increments and printed with identical material and printer settings. **Figure 23** shows exemplary printed structures and a plot of the measured lamella thickness in comparison to the design thickness. The lamella thickness was measured using ImageJ and the InteredgeDistance Macro, analogous to the evaluation of the sinusoidal line array in **Chapter 5.1.4**. In the exemplary case of printed gyroid models with 16.7% GM10, 0.15% LAP, and 0.017% QY printed at 50 µm layer height with 12 s exposure and 60 s dark polymerization, the deviation was found to be a near-linear factor of 0.55 (refer to **Figure 23**). Because the deviation is material and process-dependent, it should be determined empirically and factored into the design to achieve an accurate representation of features when using stereolithographic printing.

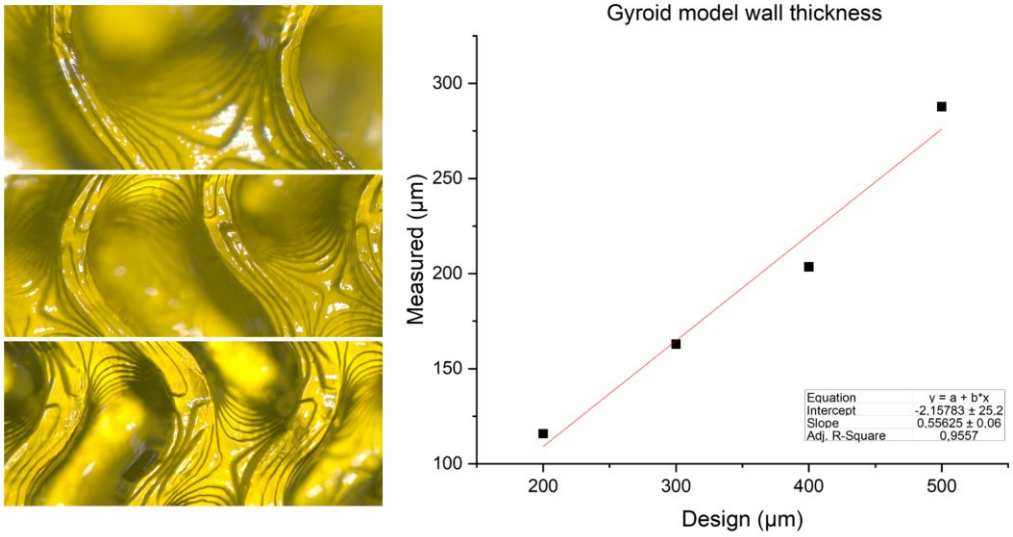

Figure 23: Determining dimensional deviations. Dimensional deviations were determined by evaluating measured lamella thickness as a function of designed lamella thickness. Exemplary plot for gyroid structures printed with 12 s exposure and 60 s dark polymerization using 16.67% GM10 with 0.15% LAP and 0.017% QY. Exemplary microscopy images of printed structures show that high fidelity is retained when substantially reduced exposure times are combined with dark polymerization.

However, parallel experiments on cell viability as a function of exposure time showed no significant effect and, therefore, gave no reason to reduce exposure times and LAP concentration (refer to **Chapter 5.3.2**). Consequently, the experiments on dark polymerization were not continued. Nonetheless, this approach could prove interesting if future experiments focus on varying stiffness by exposure time. The results suggest that the process window of mSLA bioprinting may be extended to shorter exposure times by increasing the waiting time after layer illumination, thereby expanding the range of possible final print stiffness with the same protein resin.

5.3. Bioprinting and cell viability

Light-based bioprinting has made substantial steps forward in tissue engineering, particularly in the printing of scaffolds for subsequent cell seeding. Techniques such as single-photon and two-photon stereolithography have successfully established methods for creating scaffolds onto which cells can be seeded post-printing with high viability [16, 20]. These approaches benefit from not requiring stringent physiological conditions during the printing process, as cells are introduced only after the scaffold is formed. This eliminates concerns related to maintaining cell viability during printing, such as controlling temperature, humidity, and pH levels and avoiding mechanical stress, including shear stress.

However, the direct integration of cells within the bioink during the printing process remains one of the key challenges in bioprinting. True bioprinting, where cells are embedded within the material during printing, introduces several cell-specific requirements and limitations. These include maintaining physiological conditions throughout the printing process and minimizing mechanical stress to ensure cell viability. Additionally, print time becomes a critical factor, as prolonged exposure to non-physiological conditions can adversely affect cell viability. Even with initially optimal physiological conditions, cells may experience stress due to insufficient nutrient supply, inadequate removal of metabolic waste, and suboptimal CO_2 levels affecting pH balance within the material.

Despite these challenges, the direct integration of cells into the bioink offers several significant advantages. It allows for a uniform distribution of cells within the printed material, ensuring that cells are not limited to the surfaces of constructs but are embedded throughout the entire structure. This uniform distribution may lead to more homogeneous tissue formation and potentially to more functional and in vivo-like tissue constructs.

To validate and establish the feasibility of mSLA bioprinting with cells directly incorporated into the material, two cell lines derived from musculoskeletal tissue were selected: the human bone marrow-derived human mesenchymal stem cell line SCP-1(eGFP) and the human coastal cartilage-derived chondrocyte cell line TC28a2. These cell lines, originating from naturally collagen-rich ECM environments, were chosen for their anticipated compatibility with the artificial ECM-protein matrix provided by GelMA hydrogels. The results presented in this

section aim to demonstrate the viability of these cells within the printed constructs, providing insights into the potential of mSLA bioprinting.

5.3.1. Initial assessment of bioprinted constructs

Following the validation of printing ECM-based protein resins with mSLAb in **Chapter 5.1.4**, the first experiments of printing gyroid models with cell-laden GelMA were conducted. Printing SCP-1(eGFP) cells with 15% RO-12h-L at 100 µm z-resolution yielded promising results, with visible cell viability and spreading within the construct. **Figure 24** presents an exemplary printed gyroid construct, including an overview, close-up, and epifluorescence microscopy image after 19 days of culture.

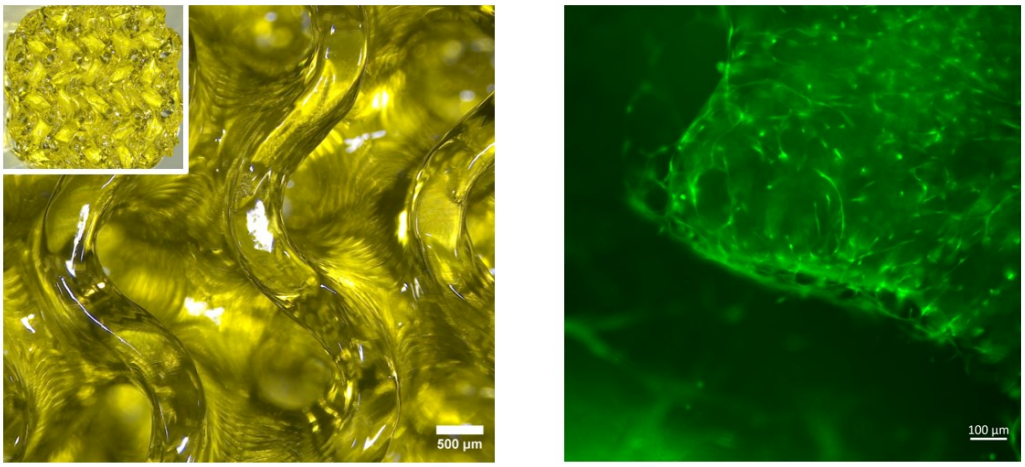

Figure 24: Gyroid structure printed with cells. Gyroid structure printed with SCP-1(eGFP) cells in 15% RO-12h-L at 100 µm z-resolution. Overview and close-up of the printed gyroid structure after print (left) and epifluorescence image of the cell's strong eGFP expression within the print after 19 days of culture. Cell spreading and cell-cell contacts suggest cell mobility and cell-matrix interaction.

The cells embedded in the gyroid structure during printing were successfully cultured by transferring the gyroid along with the glass substrate into Petri dishes. This allowed for passive diffusion of nutrients from the cell culture media during incubation, demonstrating the suitability of this porous 3D model for long-term culture without the need for active perfusion. The cells showed strong eGFP expression, indicating adequate nutrient delivery and metabolic activity. Additionally, the observed cell spreading and cell-cell contacts suggest mobility within the construct. The SCP-1(eGFP) cell line was selected with the expectation that the inherent ability of hMSCs to remodel the ECM could facilitate active interaction with the ECM-protein-based printed constructs [108]. This potential remodeling may occur through the enzymatic degradation of GelMA by matrix metalloproteinases (MMPS) [26].

These initial results demonstrate the effectiveness of mSLA bioprinting in maintaining sterile sample handling and retaining cell viability for multiple weeks. When the layer height was reduced to only 50 µm to improve z-resolution, cell viability was drastically reduced. A review of the existing literature revealed a gap in the detailed investigation of specific printing parameters and their influence on cell viability in light-based bioprinting, in general. This highlights the necessity for a more comprehensive and systematic approach to evaluate how the bioprinting process affects cell viability. To gain a deeper understanding of mSLA bioprinting and its impact on cell viability, a series of experiments were designed to investigate the contribution of specific printing parameters. The subsequent chapters will highlight these experiments, assessing the influence of individual parameters on cell viability. By systematically analyzing these parameters, the goal is to refine the mSLAb process, validate its effectiveness, and advance toward the creation of high-viability printed structures for advanced tissue engineering applications.

5.3.2. Influence of light irradiation and free radicals

The first set of experiments focused on assessing the influence of the 405 nm light source used by the mSLAb printers. To evaluate potential DNA damage due to light irradiation, a yH2.AX assay was conducted with SCP-1(eGFP) cells to check for DNA double-strand breaks (DSBs). SCP-1(eGFP) cells were cultured in a 6-well plate as a monolayer; the supernatant was removed and replaced with PBS, and the plate was placed on the LCD of the mSLAb printer and exposed for 120 seconds at 405 nm. Following irradiation, cells were incubated for an additional 30 minutes to allow for maximum yH2.AX concentrations. Cells were then fixed and labeled using the yH2.AX antibody assay [95]. The control group, which was exposed to a 365-385 nm light source, exhibited high yH2.AX levels, which indicated substantial DNA damage, and validated the assay (data not shown). **Figure 25** shows representative fluorescence microscopy images of SCP-1(eGFP) cells after 405 nm irradiation with eGFP expression (green), Hoechst-stained cell nuclei (blue), yH2.AX (red) and as merged image.

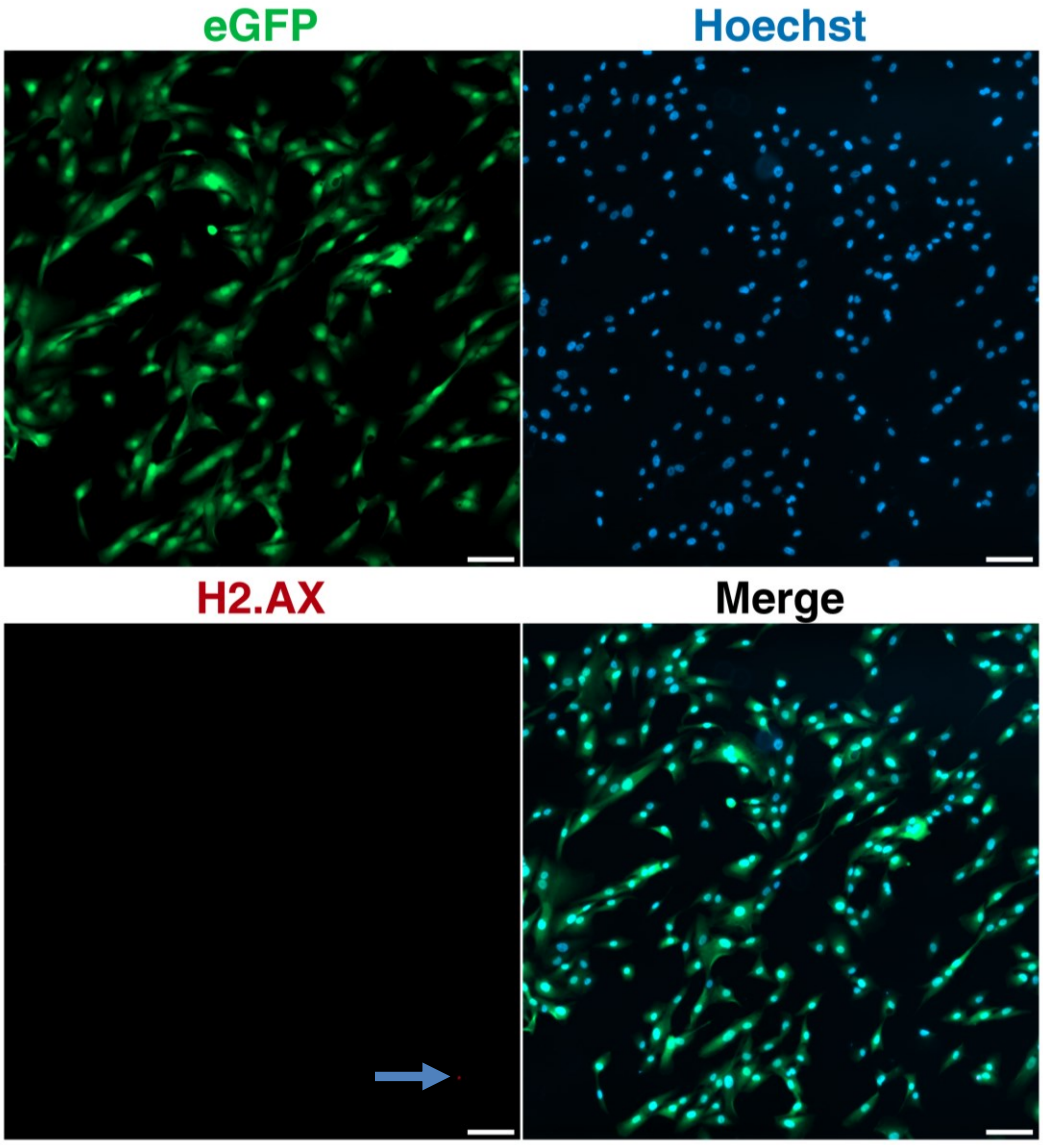

Figure 25: yH2.AX assay with SCP-1(eGFP) cells. yH2.AX assay was used to assess DNA double-strand damage due to irradiation at 405nm during the printing process. SCP-1(eGFP) cells after prolonged (120 s) exposure with 405 nm. SCP-1(eGFP) cells with eGFP expression (green), Hoechst-stained cell nuclei (blue), yH2.AX (red) and as merged. The single positive yH2.AX signal is indicated by the blue arrow. Scale bars, 100 µm.

With an exposure time of 120 seconds, the duration deliberately exceeded possible levels during bioprinting to simulate extreme conditions. Consequently, the number of photons interacting with each cell drastically exceeded standard bioprinting conditions, where a high number of cells (typically $4x10^6$ cells per ml) and hydrogel components were present to interact with the photons for polymerization. Even in these extreme conditions, only a single positive signal indicating DSBs is observable in the region of interest shown in **Figure 25** (blue arrow), which could also be attributed to processes like cell division [109]. These results are consistent with the literature, showing significantly less cell damage at 405 nm compared to light sources with lower wavelengths [64].

Subsequent experiments examined the possible negative impact of free radicals, specifically reactive oxygen species (ROS), generated by the photoinitiator LAP under 405 nm light. These ROS are produced during the photopolymerization chain reaction and may adversely affect living cells within the gel [62]. To investigate the dependency of cell viability on light exposure duration and LAP concentration, a series of experiments were conducted using 96-multiwell plates. Cells were cultured in the wells, the supernatant was removed, and the LAP in PBS solutions were added. The wells were then exposed to varying lengths of light exposure (10, 20, 40, and 60 seconds) across different plate regions. Additionally, LAP concentration varied linearly in seven steps from 6.4% to 0.1% plus control (0%). This experimental design allowed both variables to be studied simultaneously using a single multiwell plate, reducing sample preparation variances. Cells were cultured in 96 well plates to 80% confluency; the supernatant was removed and replaced with 50 µl of the specific LAP in PBS concentrations, placed in the mSLAb printer, and selectively exposed to 405 nm light according to the scheme. Following the exposure, the cells were cultured for 20 more minutes to simulate the duration of a typical print job. Afterward, the LAP solutions were removed and replaced with cell culture media, and the samples were incubated overnight. Cells were stained using DAPI and propidium iodide (PI), and the center of each well was imaged using epifluorescence and an automated script to keep data acquisition times below 30 minutes so as not to bias the results. **Figure 26** shows the pipetting scheme for the 96 multiwell plates with eight variations in LAP concentration and four variations in exposure time, yielding triplicates of all combinations (left) and hypothetical results for the live/dead assay using PI with a (PI) intensity gradient towards high LAP and exposure values (right).

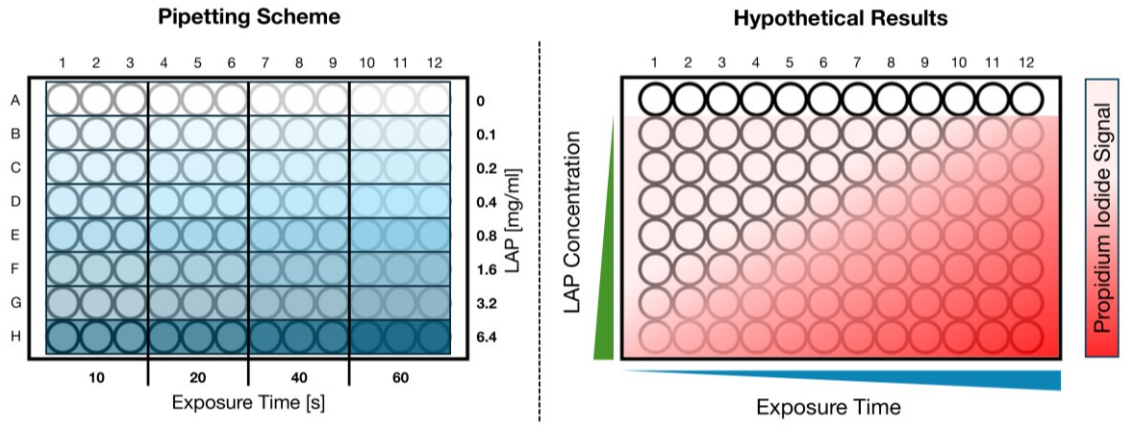

Figure 26: Influence of ROS - Pipetting scheme and hypothetical results. Left: Pipetting scheme for 96 well plates for Live/Dead assay to analyze the influence of reactive oxidative species on cell viability during photoactivation of LAP. LAP concentration was varied linearly from 0 to 6.4 mg/ml in Row A through H, and exposure time was varied in four steps from 10 to 60 s, yielding triplicates of all combinations. Right: Hypothetical results for the gradual increase of propidium iodide signal in dependence on LAP concentration and exposure time.

At the end of the automated acquisition cycle, the first well of each plate was imaged again to verify that there had been no signal change during acquisition times. Images were analyzed using the “Find Particles 2D” function of ImageJ, and the number of PI-positive cells was compared to the total number of cells determined by the DAPI-stained cell nuclei. Multiple cell lines were tested to assess different levels of tolerance to ROS. **Figure 27** shows exemplary data for TC28a2 cells when exposed to different LAP concentrations and exposure durations. The experimental design showed high noise with a 43% PI signal, even in control wells with low exposure and no LAP. However, there was a noticeable increase of PI signal for extreme (6,4%) LAP concentrations even at low exposure values and for high LAP concentrations (≥0,8%) with prolonged exposure times (60s). The results for high LAP concentrations are consistent with literature that reports good cell viability with LAP concentrations of 0.3% and 0.5% and reduced viability with concentrations above 0.7% after 60 minutes of printing [63].

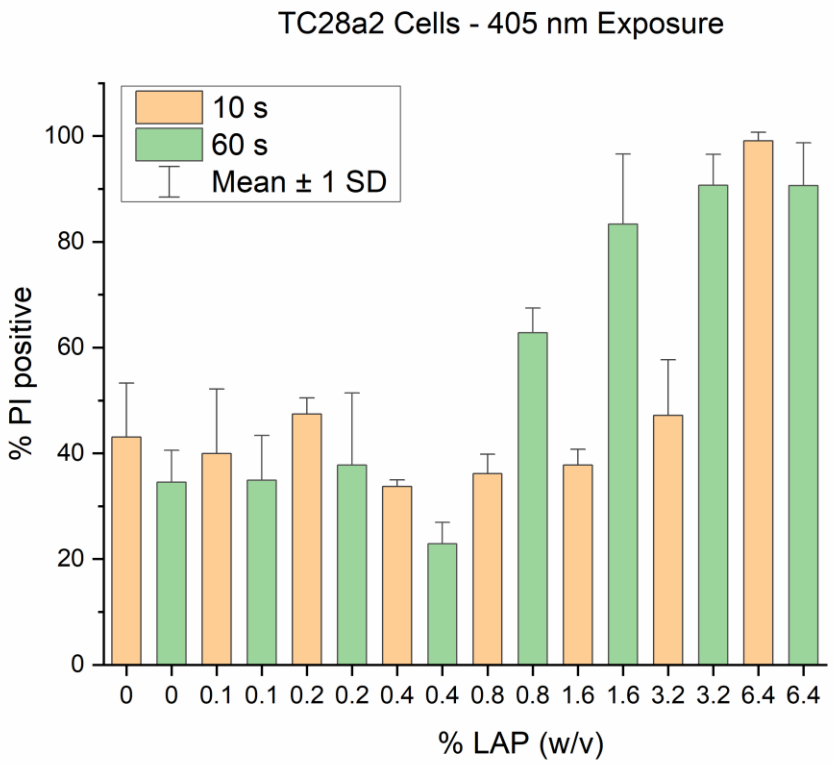

Figure 27: Influence of photoactivated LAP on TC28a2 cells. Percentage of TC28a2 cells that show positive signals for propidium iodide staining indicating membrane permeability after 10 and 60 seconds of irradiation with 405 nm in dependence on LAP concentration.

The increase in PI signal indicating cell membrane damage for high concentrations of LAP and long exposures suggests notable cell damage due to free radical oxygen species only at levels exceeding printing conditions. These results indicated no significant adverse effects on cell viability within the typical

range of LAP concentrations (≤ 0.5%) and exposure times (≤ 25 s) used for bioprinting. Only under severe conditions was a reduction in cell viability observed. It is important to note that the experimental conditions involving a monolayer of cells and 100 µl of LAP solution likely resulted in a substantially higher ratio of radicals per cell compared to typical bioprinting conditions, where the ratio of LAP molecules per cell is much lower, and the free radicals are used to polymerize the material. Possible reasons for the high background level of the PI signal during experiments include the use of excessive PI, cell membrane permeabilization due to mechanical stress, and temperature changes during plate and liquid handling. The results were consistent with the literature, so further optimization of the assay was not considered necessary at this stage. Following these preliminary experiments, there was no explicit indication that the wavelength of the light source or the number of free radicals generated by LAP exposure had a substantial adverse effect on cell viability within the parameters used for bioprinting with mSLAb.

5.3.3. Influence of z-resolution on cell viability

The initial results presented in **Chapter 5.3.1** indicated higher cell viability and cell spreading when printing thicker layers (100 µm) compared to thinner layers (50 µm). To further investigate the impact of different z-resolutions (i.e., layer thickness) on cell viability, a series of additional experiments were conducted. These experiments aimed to assess various aspects of cell health and behavior, including cell viability (constitutive eGFP expression), metabolic activity (via mitochondrial activity assay), proliferation (EdU cell proliferation assay), and cell morphology (F-actin staining with Phalloidin and cell nucleus staining with Hoechst solution), in relation to the z-resolution used for printing. The 3D model used in these experiments is an updated version of the previously used gyroid model, now with 15 x 15 x 1.8 mm^3 dimensions and a lamella thickness of 300 µm. **Figure 28** A shows an isometric view of the gyroid model, while **Figure 28** B provides a sketch with precise dimensions. The top view in **Figure 28** C highlights a central cut made post-incubation, facilitating parallel examination using different microscopy and staining techniques. A typical region of interest (ROI) for confocal imaging is indicated by a blue arrow. Phase contrast imaging of the gyroid structure (**Figure 28** D) provides a clear visualization of the printed model, emphasizing the central gyroid lamella within the ROI.

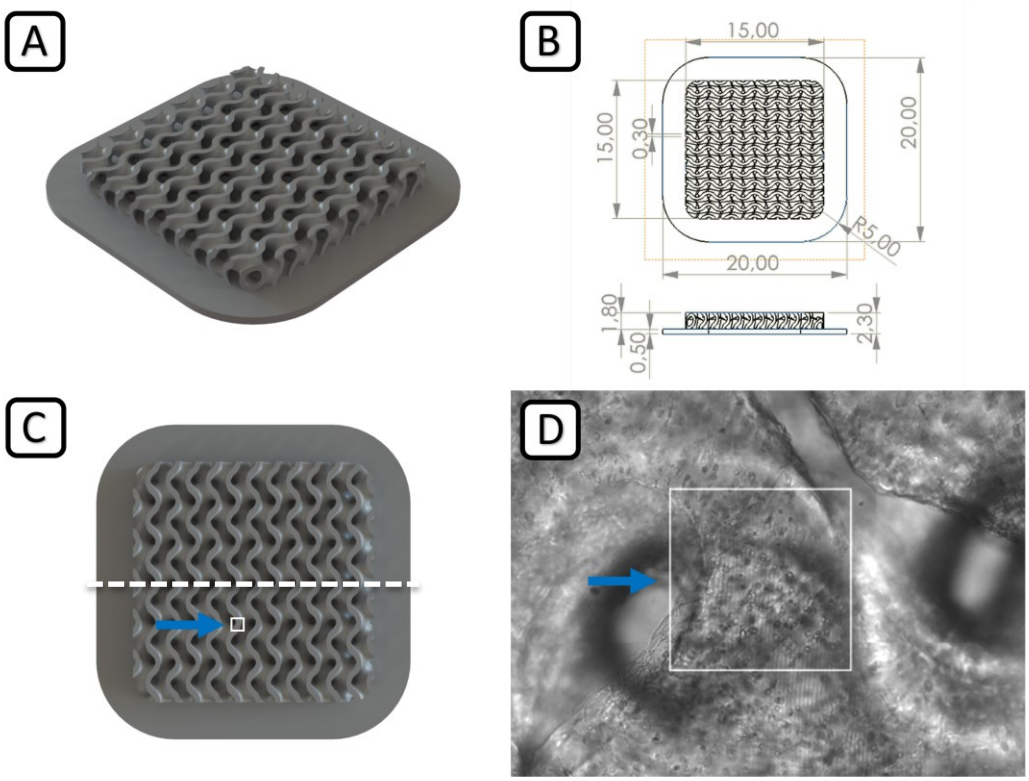

Figure 28: Gyroid model used for bioprinting. Rendering of the gyroid 3D model used for bioprinting with mSLA in an isometric view (A) and sketch with dimensions (B). The top view of the gyroid model (C) shows a central cut that is made post-incubation for the parallel examination in different microscopy and staining techniques, as well as a typical region of interest (ROI) for confocal imaging (blue arrow). Phase contrast image of the gyroid structure and representative ROI for confocal imaging with a central gyroid lamella (D).

Prints were conducted in identical conditions using the same batch of RO-12h-L (15%), LAP concentration (0.5%), and cell concentration ($4x10^6$ cells/ml) on the 8K version of the mSLAb printer. QY concentration and exposure time were adjusted to the specific layer heights, following the methods outlined in **Chapter 5.2.1**, and are detailed in **Table 2**. The printed constructs were cultured for a total of 11 days. Following fixation, the samples were cut in half (see **Figure 28** C) and used for two separate staining protocols. One part of the sample was used to observe cell morphology in 3D by staining F-actin with Phalloidin and cell nuclei with Hoechst solution. The other half of the sample was cryosectioned and stained to analyze cell proliferation. For detailed information on sample incubation and staining procedures, please refer to **Chapters 4.2** and **4.6.2**.

Table 2. Specific print settings used for the investigation of cell viability in dependence on z resolution.

Layer height [µm]	**100**	**90**	**80**	**70**	**60**	**50**
Exposure [s]	25	25	24	23	23	22
QY [%]	0.0275	0.0295	0.0315	0.0335	0.0355	0.0375

Figure 29 shows the cell morphology of SCP-1(eGFP) cells printed in gyroid constructs using mSLAb. The images are normalized maximum intensity projections of 147 µm confocal z-stacks (50 slices, spaced 2.998 µm apart) with eGFP expression in the cell cytosol (green) and Hoechst-stained cell nuclei (blue). Images show representative and comparable sections of the gyroid structure taken at identical exposure settings and post-processing of images. Samples printed at 50 and 60 µm z-resolution showed drastically lower nuclei count and negligible eGFP signal compared to higher layer heights. eGFP expression as an indicator of cell viability and metabolic activity and a higher number of cell nuclei are visible in samples printed with 70 µm layer height and above, improving drastically with 80 µm and gradually with samples printed at 90 and 100 µm.

While cell spreading and cell-hydrogel interaction (adhesion) are visible at the outer surfaces of the gyroid lamella in samples printed at 80 µm (the water-hydrogel interface is indicated by the yellow dotted line in **Figure 29**), the morphology of cells located deeper within the structure further improved with cells showing eGFP expression and spreading at 90 and 100 µm layer height. Exemplary cell-cell contacts are indicated by the yellow arrows in **Figure 29**. These results show low cell viability and indicate high cell stress during printing with low layer heights (< 70 µm), low to moderate cell viability at 70 µm, and improved viability in samples printed at 80 µm and higher after 11 days of culture.

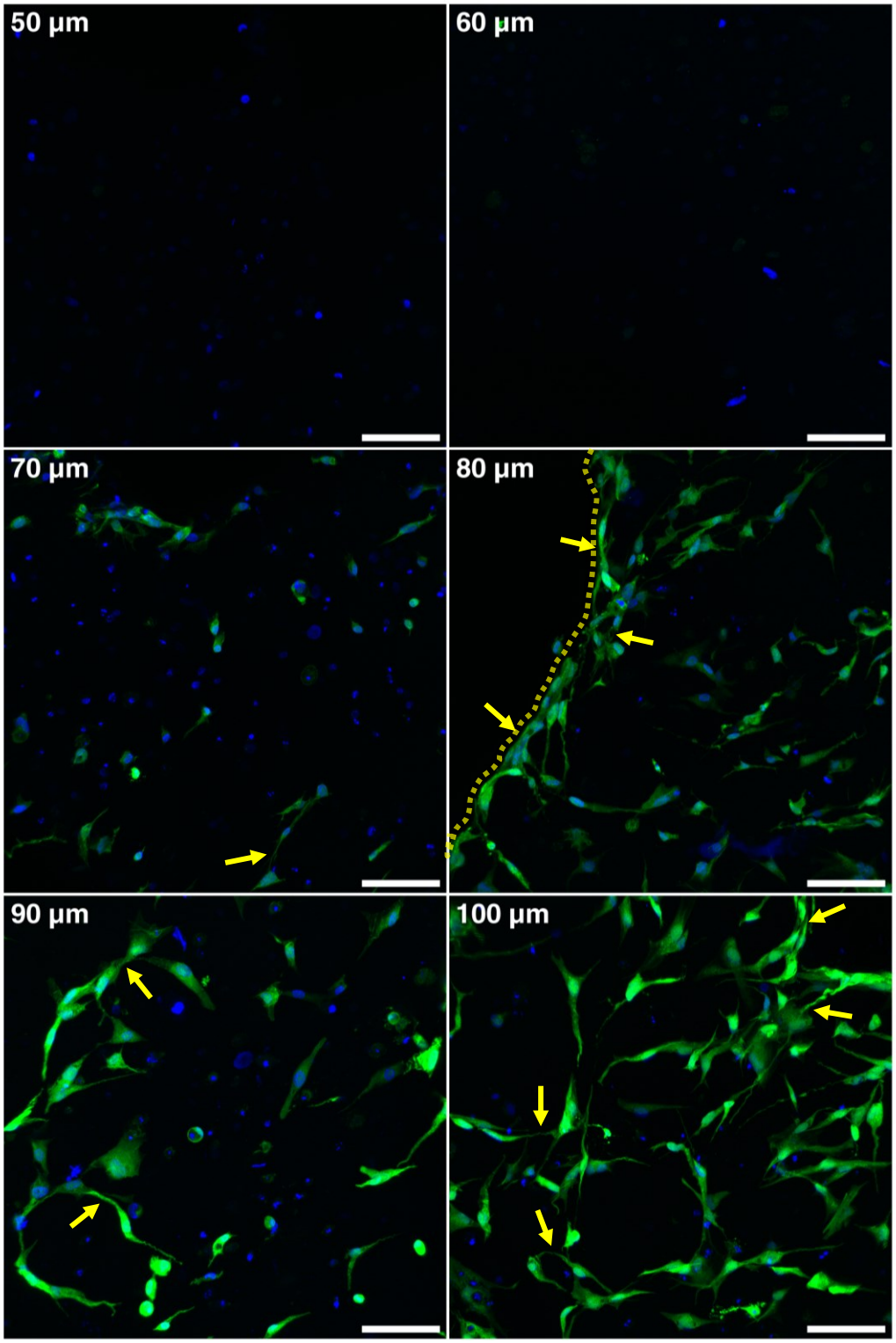

Figure 29: eGFP expression of SCP-1(eGFP) cells printed with different z-resolution. Confocal microscopy images of gyroid constructs printed with SCP-1(eGFP) cells at different z-resolutions (layer height) using mSLAb and 15% RO-12h-L after 11 days of culture. Maximum intensity projections of 147 µm z-stacks with eGFP expression in the cytosol (green) and Hoechst-stained cell nuclei (blue). Images show representative and comparable sections of the gyroid structure taken at identical exposure settings and post-processing of images. Noticeable eGFP expression and cell spreading for samples with 80 µm layer height and above indicate good cell viability and interaction with the biomaterial. The dotted line indicates the water-hydrogel interface. Images were acquired with 20x/0.40 objective. Scale bars, 100 µm.

Figure 30 shows the maximum intensity projections of the phalloidin-labeled F-actin fibers and Hoechst-stained cell nuclei of the 50, 70, and 100 µm samples (identical to **Figure 29**) with zoomed-in region of interest (ROI) of representative cell clusters. The F-actin fiber morphology is in alignment with the results for the eGFP expression, showing only residual signals of unaligned F-actin in the 50 µm layer height sample. The F-actin signals suggest that an equal number of cells were printed into all samples with disorganized spherical F-actin revealing cell locations, visible as cell-sized circles in the phalloidin channel of the 50 µm sample in **Figure 30**. Compared to F-actin signals, only a few Hoechst and no eGFP signals remained in samples printed at 50 and 60 µm z-resolution. This suggests that, while cells were embedded in the samples during printing, they were not viable. Consequently, it is likely that eGFP expression ceased, and cell nuclei underwent fragmentation and degeneration as part of apoptosis, leaving only F-actin signal from encapsulated cell debris. The samples printed at 70 µm layer height were the first to exhibit signs of F-actin anisotropy, suggesting cytoskeletal organization and cell-biomaterial interaction, such as cell adhesion to the biomaterial. These results suggest that the cells may have selectively degraded the surrounding protein matrix using MMPs, facilitating their movement and spreading and thereby potentially remodeling their microenvironment to promote cell migration and the establishment of cell-cell contacts [26, 108, 110]. In addition, the formation of cell-cell contacts after multiple days of culture among the initially predominantly individually distributed cells (like the encapsulated spherical cells in the 50 µm sample) supports the assumption of cell mobility and high viability of the remaining cells in the 70 µm sample. In the samples printed at a 100 µm layer height, these positive characteristics were further enhanced. The F-actin anisotropy was more prevalent, demonstrating a higher degree of cytoskeletal organization, with only a few cells showing spherical morphology (see also **Figure 29)**.

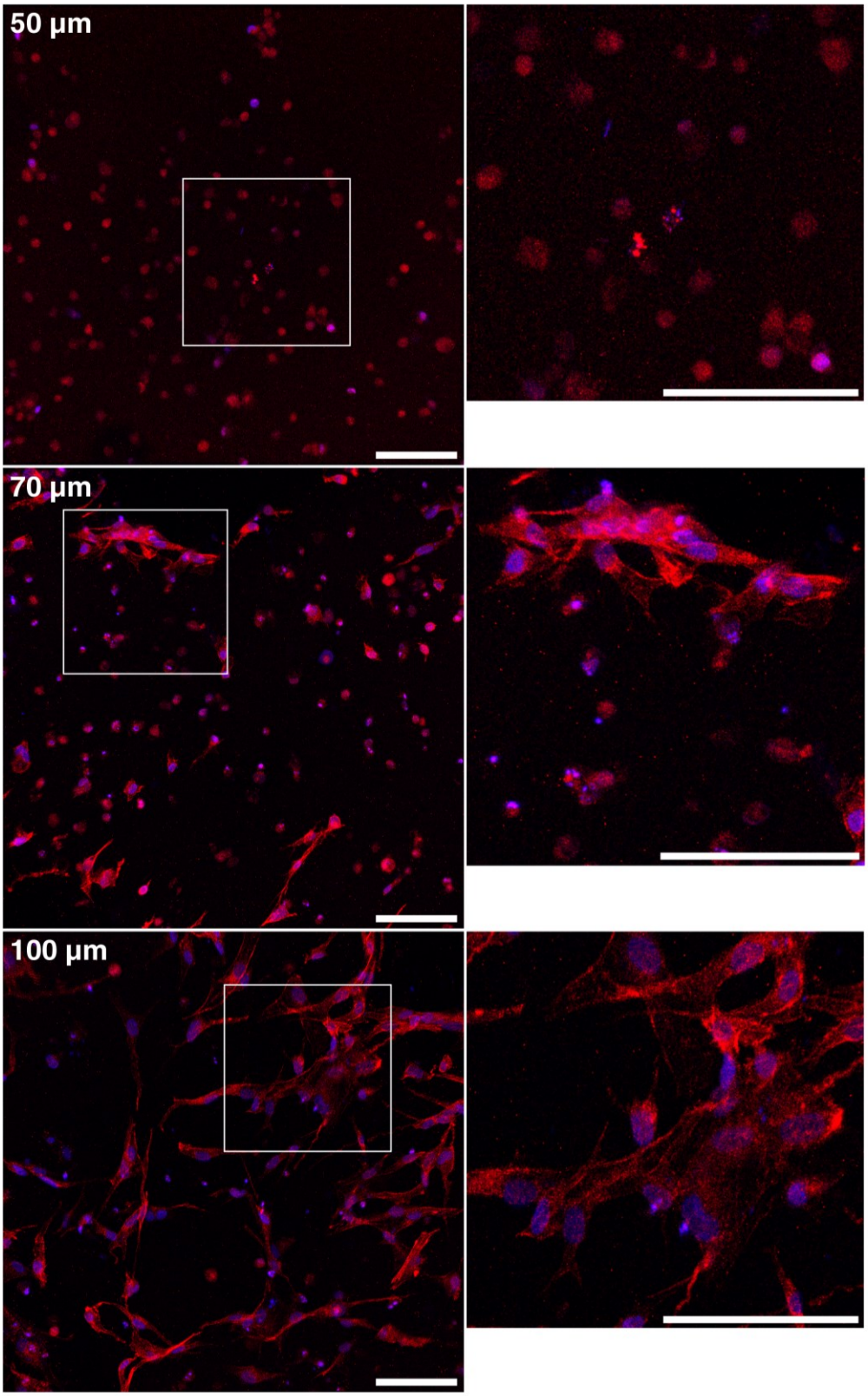

Figure 30: Actin-F cytoskeleton morphology of SCP-1(eGFP) cells printed with different z-resolution. Confocal microscopy images of gyroid constructs printed with SCP-1(eGFP) cells at different z-resolutions (layer height) using mSLAb and 15% RO-12h-L after 11 days of culture. Maximum intensity projections of 147 µm z-stacks with Phalloidin-stained F-Actin (red) and Hoechst-stained cell nuclei (blue). Images show representative and comparable sections of the gyroid structure taken at identical exposure settings and post-processing of images. Images were acquired with 20x/0.40 objective. Scale bars, 100 µm.

The other half of each sample was embedded in cryomedium and cryosectioned to be stained for proliferation to further investigate the cell viability in dependence on the mSLAb z-layer height. For detailed information on sample incubation and staining procedure, please refer to **Chapter 4.6**. Briefly, on day 6 of culture, the first reagent of the EdU cell proliferation assay was added, which is integrated into the DNA during proliferation and visualized by adding a second reagent (click chemistry) to the cryosectioned samples. The 30 µm thick sections were imaged using confocal microscopy to generate 30 µm z-stack images, which were converted to maximum intensity projections and analyzed by manually counting the total cell numbers using the Hoechst-labeled cell nuclei and cells that showed positive signals for the proliferation assay. **Figure 31** is a plot of the percentage of cells with positive signals for proliferation, as well as the total number of cells counted in representative cryosections of samples printed at different z-resolutions. Notably, there is a sharp increase in the percentage of proliferation-positive cells when comparing 60 and 70 µm to 80 µm samples. When only the fraction of proliferating cells is compared, proliferation does seem to stagnate at layer heights greater than 80 µm.

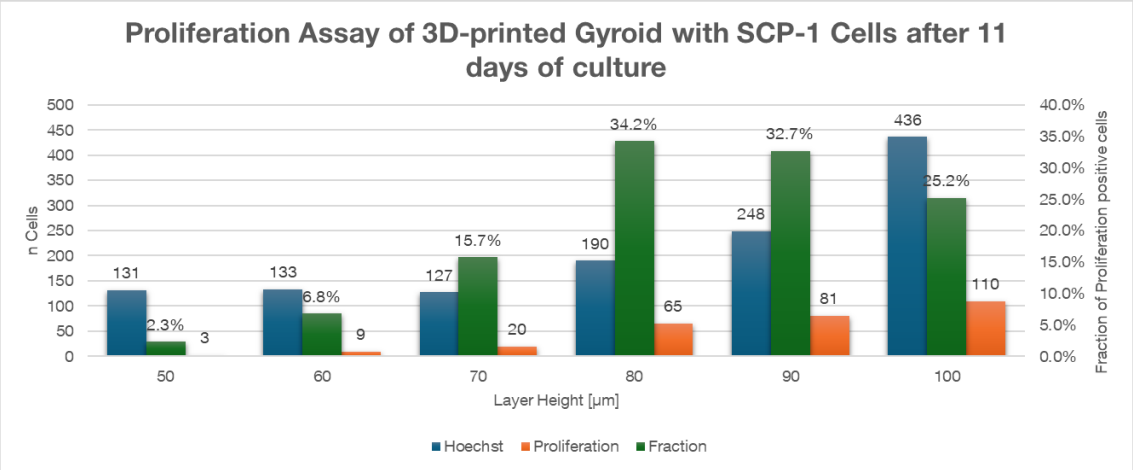

Figure 31: Proliferation in dependence on printing z-resolution. Percentage of cells showing positive signals for proliferation and the total number of cells counted in representative cryosections of samples printed at different z-resolutions.

However, it is important to note that the manufacturer's protocol for the proliferation assay was designed for monolayer cell culture and was first adapted for these 3D experiments based on estimates to fit the 3D sample model with cells printed in GelMA hydrogel. When looking at the total number of cells in comparable volumes of samples, there is a noticeable increase towards higher layer height samples, with the cell count more than doubling from 80 µm to 100 µm samples. This suggests that the amount of the first reagent of the assay, which is integrated during proliferation, was depleted during incubation and was

too low to stain samples with high proliferation accurately. Future experiments should determine if a one-time addition of the reagent (i.e., on day 6) in a higher concentration or a repeat addition of reagent is necessary to not limit the signal and skew data towards lower proliferation samples. The proliferation assay results align with the previous results for cell morphology, viability, and metabolic activity, suggesting the most considerable increase in cell signals in the 70- and 80 µm z-resolution range.

In summary, the combined results of confocal imaging of constitutive eGFP expression, cell morphology (F-actin and cell nuclei), and evaluation of cell proliferation of samples printed at different z-resolution with otherwise identical material composition (15% RO-12h-L and 0.5% LAP), number of cells ($4x10^6$ cells/ml) and sample volume, revealed a correlation of z-resolution with cell viability. When the printing process is examined, causation seems plausible – as the z-resolution (i.e., layer height) approaches the size of cells, whose geometry approximates spheres floating in a high density within a hydrogel, moving with the flow of the material during substrate (z-axis) movement after every single layer is exposed. Please refer to **Chapter 4.2** and **Figure 5** for details on the printing process and movements. In the comparison presented in this chapter, identical geometries were printed, which leads to more individual layers being polymerized in samples printed with thinner layers, i.e., 46 layers of a sample printed at 50 µm, compared to 23 layers for the same gyroid printed at 100 µm. This also contributes to overall printing times, see **Table 3**.

Table 3. Number of printed layers and overall print time in dependence on z-resolution.

Layer height [µm]	**100**	**90**	**80**	**70**	**60**	**50**
Layers [n]	23	25	28	32	38	46
Print time [min]	19	20	21	24	26	30

To gain more insight into the individual contribution of these factors (i.e., layer height, overall print time, and number of layers printed), these experiments should be repeated and normalized not to sample geometry but to one of the other parameters. This series of experiments was normalized to sample geometry because, typically, 3D printing processes start with the desired 3D model (constant), and the number of layers and print time are secondary (conditional elements). There is already literature on shear forces during extrusion-based bioprinting that suggests that this type of cell stress may be the leading cause of reduced cell viability [111-113]. Preliminary experiments conducted during printing parameter optimization on the influence of z-axis movement speed, varying between 10 and 80 mm/s, showed no significant effect on cell viability. Therefore, the speed was set to 80 mm/s during this series to minimize print time. However, with the results suggesting a dependence of

cell viability on shear stress, and with the velocity and acceleration of the z-axis movement possibly influencing the forces experienced by the cells, these variables might also be of interest to future studies.

While constitutive eGFP expression provided initial insights into cell activity, further investigation was conducted to gain a deeper understanding and support the hypothesis of metabolic activity. An additional set of gyroid constructs with SCP-1(eGFP) cells were printed at 50 and 100 µm resolutions. The MitoTracker assay was used to visualize metabolic activity by staining cell mitochondria with active membrane potential. Additionally, the prints were stained with phalloidin for F-actin and Hoechst for cell nuclei, as in previous experiments. **Figure 32** shows maximum intensity projections of 2x1 fields of view stitched 149.92 µm z-stacks of SCP-1(eGFP) cells printed at 50 and 100 µm z-resolution with mSLAb and 15% RO-12h-L after 15 days of culture. The images were normalized and show representative sections of the gyroid construct.

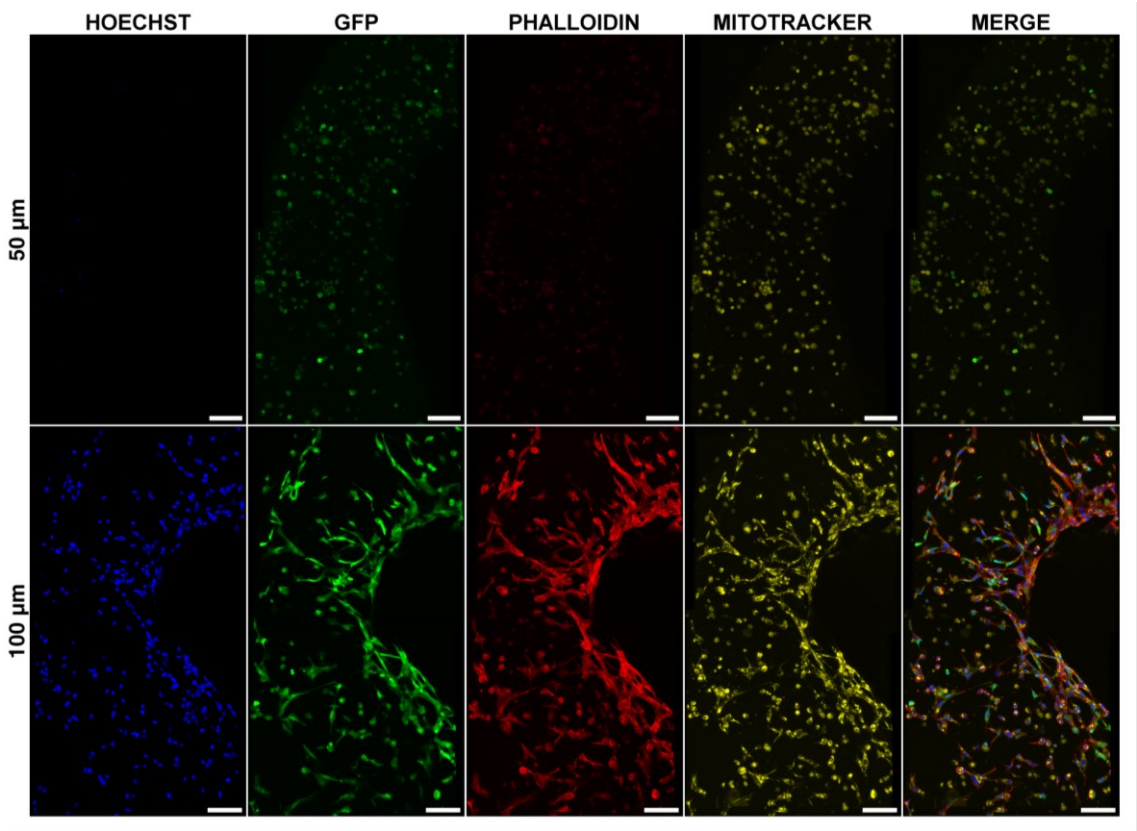

Figure 32: Morphology and metabolic activity of SCP-1(eGFP) cells printed at different z-resolution. Confocal microscopy images of gyroid constructs printed with SCP-1(eGFP) cells at 50 and 100 µm z-resolution using mSLAb and 15% RO-12h-L after 15 days of culture. Maximum intensity projections of 150 µm z-stacks with Hoechst-stained cell nuclei (blue), eGFP expression in the cytosol (green), phalloidin-stained F-Actin (red), MitoTracker-stained Mitochondria, and merged image. Images were acquired with 20x/0.40 objective. Scale bars, 100 µm.

The 100 µm print exhibited robust signals across all channels, with visible cell spreading, indicating cell-cell contacts and hydrogel interaction. The MitoTracker channel revealed active mitochondria, corroborating the presence of metabolic activity. In contrast, the 50 µm print displayed faint eGFP expression and mitochondrial activity, with minimal signals in the Hoechst and phalloidin channels. These observations are consistent with previous experiments, validating eGFP expression as a reliable indicator of metabolic activity. Higher cell density near the hydrogel surface suggests cellular responses to nutrient and stiffness gradients at the water-hydrogel interfaces. Nutrient availability is naturally higher near the surface of the printed matrix, surrounded by cell culture medium, which may lead to increased proliferation, higher metabolic activity, and migration along the nutrient gradient (chemotaxis). In addition, researchers have shown that prints generated by two-photon polymerization with GelMA-based protein resins exhibit stiffness gradients from the surface inwards, with reduced stiffness at the surface [16]. The exact contributing factors to this gradient are not entirely clear but may include reduced polymerization efficiency due to lower light intensity/excitation at the boundaries of the printed structure and swelling of the hydrogel matrix during incubation in cell culture medium. This gradient may have a contributing influence on cell behavior, potentially affecting cell mobility and interaction with the hydrogel matrix.

To further investigate and find an ideal compromise between z-resolution and cell viability, another sample was printed at a 75 µm layer height and cultured for 15 days. Given that the 70 and 80 µm samples showed the most notable changes in cell viability and proliferation, an intermediate z-resolution was chosen for this experiment. All other parameters remained unchanged to isolate the effect of layer height on cell viability. Additionally, this experiment aimed to gain insight into the distribution of cells within the printed construct and their ability to move and spread in all directions, assessing whether boundaries could be perceived at the interface of individual layers. To achieve this, a larger ROI within the construct was imaged using z-stack confocal imaging. **Figure 33** shows the eGFP expression (A) and depth-coded eGFP expression (B) of SCP-1(eGFP) cells printed at 75 µm z-resolution as maximum intensity projection of a 504 µm z-stack (127 slices, spaced 3.999 µm apart) in top view and side views (C, D). This extensive z-stack provided a more detailed impression of cell morphology and homogeneity throughout a gyroid lamella. Despite reduced signal intensity further from the surface, confocal microscopy successfully captured eGFP expression and cell morphology across the entire 500 µm z-stack, revealing the distinct 3D shape. Cell-cell contacts were visible in all spatial directions, suggesting isotropic material composition and unrestricted cell mobility with no barriers between individual printed layers.

These findings suggest that 75µm layer height could pose a good compromise between z-resolution and cell viability.

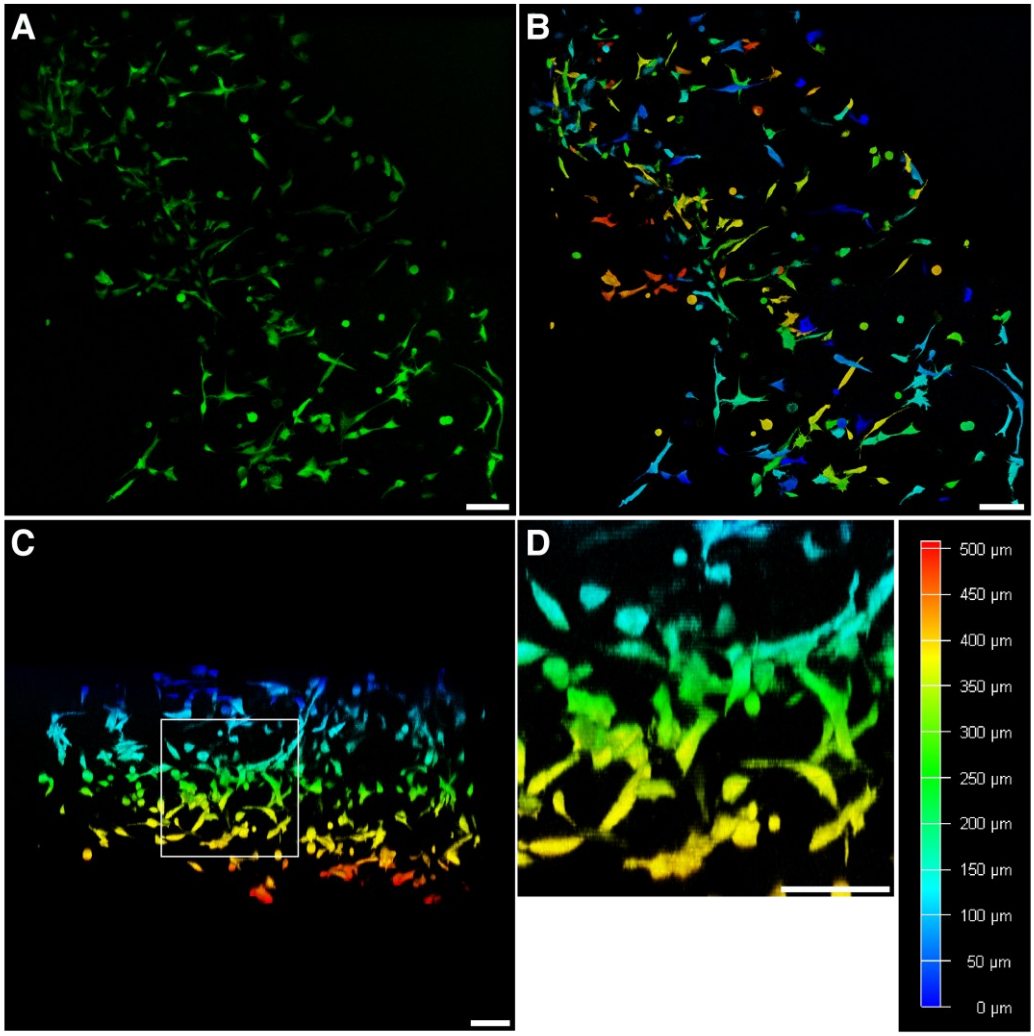

Figure 33: SCP-1(eGFP) cells printed at 75µm with depth-coded eGFP expression. Confocal microscopy image of a gyroid construct printed with SCP-1(eGFP) cells at 75 µm z-resolutions (layer height) using mSLAb and 15% RO-12h-L after 15 days of culture. Maximum intensity projections of 504 µm z-stack of eGFP expression (A) and depth-coded eGFP expression (B) in top view. Depth-coded side view (c) and zoomed-in ROI showing isotropic spreading of cells (D). Note the homogenous distribution of cells throughout the construct and the clearly discernible shape of the 3D gyroid lamella. Images were acquired with 20x/0.40 objective. Scale bars, 100 µm.

To evaluate the transferability of the findings on the effect of layer thickness found with SCP-1(eGFP) cells, the investigation was extended to include another cell type derived from musculoskeletal tissue. The TC28a2 cell line, derived from human costal cartilage, was selected as a well-established model for chondrocyte biology and physiology. Analogous to the origin of the SCP-1(eGFP) cells, these chondrocytes are located in a collagen-rich ECM environment in vivo, making them well-suited for integration within GelMA-based protein structures. TC28a2 cells were printed in 15% RO-12h-L under identical conditions to SCP-1(eGFP) cells to assess cell-specific viability and interaction

with the hydrogel matrix. Similar to SCP-1(eGFP) cells, TC28a2 cells exhibited a high dependence of viability and metabolic activity on z-resolution. In the samples printed at 50 µm layer height (data not shown), TC28a2 cells showed low to no visible cell viability, whereas printed at 100 µm layer height, high cell viability was observed. Notably, TC28a2 cells demonstrated distinct cell morphology near the surface regions and deeper within the printed hydrogel. **Figure 34** presents maximum intensity projections of 50.97 µm z-stack confocal microscopy images of TC28a2 cells printed in 15% RO-12h-L at 100 µm resolution after 5 days of culture, with phalloidin-stained F-Actin and Hoechst-stained cell nuclei.

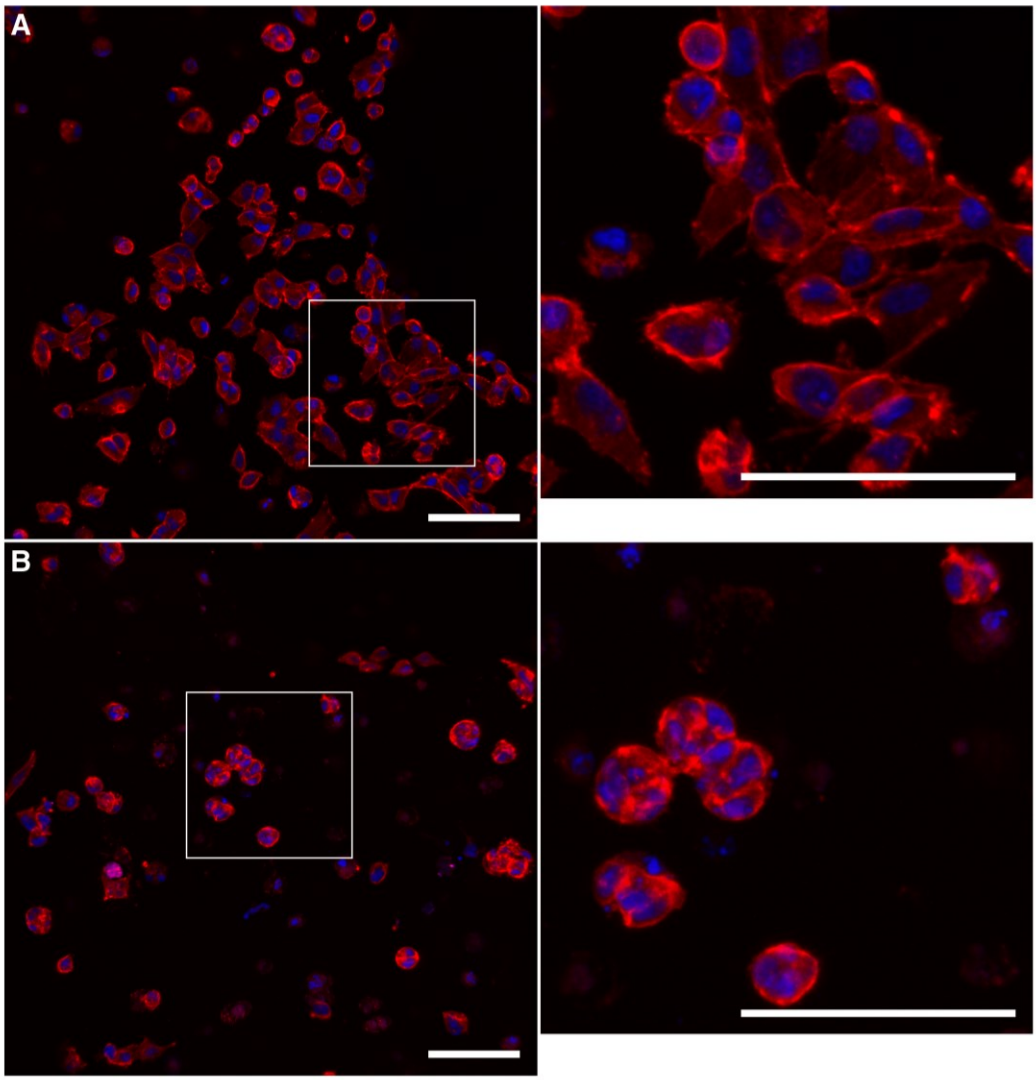

Figure 34: Actin-F cytoskeleton morphology of TC28a2 cells printed with mSLAb. Confocal microscopy images of gyroid construct printed with TC28a2 cells with 100 µm z-resolutions (layer height) using mSLAb and 15% RO-12h-L after 5 days of culture. Maximum intensity projections of 51 µm z-stacks with phalloidin-stained F-Actin (red) and Hoechst-stained cell nuclei (blue). Images show representative sections of the gyroid structure taken at identical exposure settings and post-processing of images at the surface of the structure (A) and 200 µm deeper in the construct (B) with respective zoomed-in ROI. Images were acquired with 20x/0.40 objective. Scale bars, 100 µm.

Cells near the surface exhibited a more stretched conformation with distal cell-cell contacts (**Figure 34** A, zoomed-in ROI), whereas cells in deeper regions of the biomaterial displayed an agglomerate morphology, forming cell spheres composed of 3-10 cells (**Figure 34** B, zoomed-in ROI). It remains unclear whether these agglomerates originated from individual cells proliferating without notable spreading and migration or from cells migrating toward one another to form clusters. Follow-up experiments aimed at further investigating TC28a2 cell viability, morphology, and metabolic activity in relation to z-resolution and location within the hydrogel were inconclusive due to recurrent mycoplasma contamination. This contamination was unrelated to the mSLAb process and was introduced through shared media with parallel projects in the laboratory. Despite the challenges encountered, the successful printing of TC28a2 cells demonstrates the potential of this cell line for further investigation in mSLA bioprinting. The distinct morphologies observed near the surface and deeper within the hydrogel suggest a possible response to varying microenvironments. These promising results indicate that continued exploration of TC28a2 cells in mSLA bioprinting could yield valuable insights into cell-material interactions and tissue engineering strategies.

5.3.4. Influence of a second GelMA derivate (GM10)

To investigate the effect of using different GelMA variants on cell viability experiments with GM10 were conducted by printing samples with SCP1-(eGFP) cells and identical conditions to the experiments presented in **Chapter 5.3.3** (i.e., 15% GelMA concentration, 100 µm z-resolution) to observe possible differences in cell morphology and metabolic activity. GM10 is a GelMA derivate with an exceptionally high degree of functionalization (refer to **Chapter 2.2**) that has shown good cytocompatibility when used as a protein resin for scaffold fabrication and subsequent cell seeding [16, 57]. These experiments aimed to validate GM10 for mSLA bioprinting with cells directly incorporated into the matrix during printing. **Figure 35** shows a maximum intensity projection of a 149.33 µm z-stack (63 slices, spaced 2.409 µm apart) of SCP-1(eGFP) cells printed at 100 µm z-resolution with mSLAb and 15% GM10 after 15 days of culture. The image displays eGFP expression in the cell cytosol (green), Hoechst-stained cell nuclei (blue), phalloidin-stained F-actin (red), and MitoTracker-stained mitochondrial activity (yellow). The results demonstrate that GM10, which was previously adapted for TPS scaffold fabrication, can be printed using mSLAb with cells incorporated directly into the material and that it is effectively colonized by these cells.

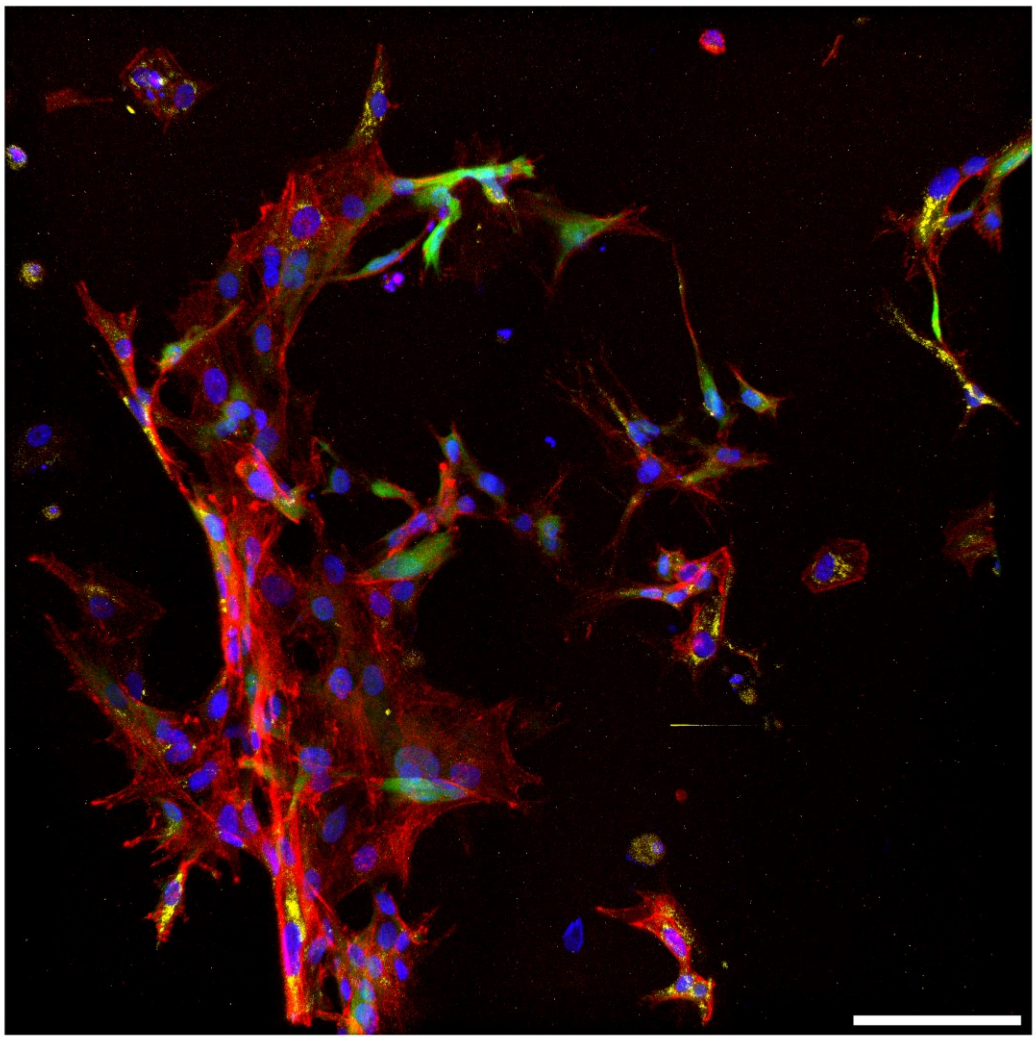

Figure 35: Morphology and metabolic activity of SCP-1(eGFP) cells printed with GM10. Confocal microscopy image of a gyroid construct printed with SCP-1(eGFP) cells at 100 µm z-resolution using mSLAb and 15% GM10 GelMA after 15 days of culture. Maximum intensity projections of 149.33 µm z-stack with Hoechst-stained cell nuclei (blue), eGFP expression in the cytosol (green), phalloidin-stained F-Actin (red), MitoTracker-stained mitochondria (yellow). Images were acquired with 20x/0.40 objective. Scale bar, 100 µm.

Cells exhibited well-defined stretching and adhesion, particularly towards the hydrogel-water interface, which is located in the left quarter of the image, indicating good compatibility with GM10 resin. Compared to RO-12h-L, cells showed a higher affinity for surface regions, potentially due to the overall higher stiffness of GM10. The increased crosslinking density of GM10 may result in smaller pore sizes, thereby reducing nutrient diffusion from the surface. During the culture of GM10 constructs, cells transitioned more slowly from an initially round morphology to spreading, with reduced mobility. Further investigation is required to determine the influence of stiffness alone, which could be adjusted by varying the hydrogel concentration. Additionally, assessing the specific impact of different GelMA variants on cell behavior, particularly in relation to GelMA synthesis, is necessary. These observations suggest that the distinct

morphologies could be a response to varying microenvironments within the hydrogel.

Taken together, these findings suggest that cells react dynamically to the microenvironment provided. These results highlight the exciting potential for developing methods to actively control these parameters. The promising observations open numerous avenues for further research. Specifically, the development of cell-specific bioink formulations could provide valuable insights into cell behavior and interactions within various microenvironments. The findings underscore the potential of mSLA bioprinting technology combined with ECM-based protein resins. The ability to tailor bioprinting parameters and bioink compositions to specific cell types could offer a pathway to optimizing tissue engineering strategies.

6. Conclusion

The primary aim of this doctoral thesis was to investigate the potential of mSLA technology for bioprinting applications. This study demonstrates the application of mSLA to the bioprinting of cell-laden ECM-based protein resins.

The first research question was whether mSLA could be used for the bioprinting of ECM-based protein resins and to identify the key requirements for mSLA bioprinters. To investigate the use of this technology in bioprinting, a conventional commercial mSLA printer (Phrozen Sonic Mini 4K) was successfully converted to an mSLA bioprinter. This involved integrating temperature control to maintain constant temperatures during the prints, enabling reproducible processing of cell-laden ECM protein-based hydrogels. Additionally, a humidification strategy was implemented to minimize hydrogel evaporation. An innovative build platform for attaching glass substrates was designed to streamline sample handling and integrate the printed tissue constructs into cell cultivation and microscopic analysis workflows. The resulting concept to convert mSLA printers to bioprinters was published as an open-source and open-access project to enable the reproduction of these results and foster customization and further community-driven development in the bioprinting research field. The mSLAb concept was subsequently applied to a next-generation printer (Phrozen Sonic Mini 8K), requiring only minor design changes, thereby validating the concept as a sustainable project applicable to other mSLA printers.

The second research question focused on identifying suitable GelMA-based protein resin compositions containing a cell-compatible photoinitiator and photoabsorber combination for mSLA bioprinting and investigating how these compositions, along with printing parameters (e.g., exposure time and layer height), affect the printability and fidelity of constructs. Two GelMA derivatives, RO 12h L and GM10, selected from the literature for their effective use in single and two-photon stereolithography, respectively, were synthesized and successfully combined with LAP and QY in cell-compatible compositions for mSLA bioprinting. By printing gyroid benchmark structures, concentrations of these components, which are well suited for 3D bioprinting and, at the same time, cell-friendly, were determined and validated through cell-based assays using the printer's specific light source. The results confirmed the complex interplay between printing parameters (e.g., exposure time and layer height) and the need to fine-tune material compositions, specifically the photoabsorber, to maximize resolution and facilitate printing of true 3D arbitrary geometries with overhangs and hollow features.

The third research question investigated whether different cell lines could be effectively incorporated into the mSLA bioprinting process, printed with sufficient viability, and subsequently cultured to evaluate cell behavior within the constructs. Two cell lines derived from collagen-rich ECM musculoskeletal tissue, the hMSC cell line SCP-1(eGFP) and the chondrocyte cell line TC28a2, were chosen and directly integrated into the protein resins and bioprinted into gyroid constructs, which were successfully cultivated for several weeks. Suitable fluorescence staining and microscopy protocols were established to analyze the cell behavior in these 3D structures, depending on the printing parameters and the bioink used. Insights from previous research questions were used to identify process windows that balance cell viability and printing resolution, ensuring the successful incorporation and cultivation of cells within bioprinted constructs. The results of 3D fluorescence microscopy using the SCP-1(eGFP) and TC28a2 cell lines suggest a correlation between z-resolution and cell viability due to shear forces exerted on the cells during printing. Bioprinting with layer heights < 75 µm caused extensive loss of cell viability, while cells printed at z resolutions ≥ 75 µm progressively exhibited metabolic activity and proliferation. Cell morphology visualized through F-actin staining and constitutive eGFP expression suggested that cells might modulate the artificial ECM environment to enable mobility, migration, and proliferation along nutrient or stiffness gradients.

Taken together, these findings establish and validate mSLA for bioprinting and provide a new basis for future 3D cell assays with cell-laden bioprinted ECM-based protein resins. The results indicate that cell behavior responds to the ECM microenvironment and other cues provided by the ECM, including nutrient and stiffness gradients. The ability to combine ECM-protein materials and cells into viable arbitrary 3D constructs that can be cultured and analyzed using high-resolution microscopy provides new avenues for tissue engineering, such as the design of cell-specific protein resins.

7. Acknowledgments

I want to acknowledge the contributions of the bachelor's and master's students I have supervised. Their project studies, bachelor's and master's theses, submitted to the Department of Applied Sciences and Mechatronics at Munich University of Applied Sciences, have been integral to the results presented in this thesis. While I was responsible for the conceptualization and development of the methodology, the students provided valuable assistance with the experimental work, without which the scope of this research would not have been possible. Matthias Rudolph, Markus Pechtl, and Geronimo Wildenburg contributed to the development of the mSLAb conversion and are co-authors of the respective research paper (Chapter 5.1). Marvin Berger and Karlo Kriedemann contributed to the optimization of printing parameters (Chapter 5.2.1). Fabienne Intelkofer and Christina Gabriel contributed to experiments on the influence of light irradiation and free radicals (Chapter 5.3.2). Svitlana Stetsenko and Sarah Klotz contributed to experiments on the influence of z-resolution on cell viability (Chapter 5.3.3). Yasemin Geiger contributed to experiments on the influence of a second GelMA derivate (Chapter 5.3.4).

I would also like to take this opportunity to thank all the people who have accompanied and supported me during my doctoral studies, providing invaluable encouragement and assistance, which contributed to the creation of this thesis.

I want to thank my supervisor, Oliver Hayden, without whom this work would not have been possible. Thank you for your swift support at any opportunity and, most of all, for giving me the freedom to pursue the topic according to my ideas.

I want to extend special thanks to my supervisor, Hauke Clausen-Schaumann, and mentor, Stefanie Sudhop, who have supported me throughout my entire scientific journey. From the moment I stepped foot into the labs of CANTER, mere theory turned into “applied science,” and my fascination with bioprinting was born. They encouraged me to seek a blank spot on the metaphorical map of science and fill this knowledge gap. Their tireless support and the opportunities they provided were invaluable to reaching this goal.

I want to thank Sascha Schwarz for not only providing inspiration and honest feedback but also for the great conversations and comic relief. Yasemin Geiger and Matthias Rudolph, it was a pleasure sharing an office, collaborating on projects, spending countless long days in the lab, and sharing inspired conversations (over lots of coffee). Yase, your positive attitude and well-stocked

snack bar were a silver lining even on the tougher days, and Matthias, you were always ready for a debugging session to keep the projects moving forward – thank you both! Bastian Hartmann and Bastian Kreidl, thank you for many fruitful discussions, helpful feedback, and collaboration on interesting interdisciplinary side projects. Conny Hasselberg-Christoph, thank you for your continuous support in the lab – from helping with cell culture to wrangling the mighty SAP… you were a tremendous help!

It is hard to convey my gratitude to all my fellow (PhD) students, colleagues, and collaborators with whom I had the pleasure of working during my time at the universities, TranslaTUM, and CANTER especially. People like Stefanie Kiderlen, Tanja Becke, Amelie Erben, Lutz Fleischhauer, Raphael Reuten, and Aurore Dupin, to name a few – thank you for being part of this journey. Special thanks to Tanja Becke and Aurore Dupin for the opportunity to have exciting interdisciplinary collaborations that led to two published papers. I want to thank the Bavarian Academic Forum (BayWISS) for providing extra funding for the project.

Finally, I would like to thank my parents, Erika and Raimund, for their unwavering belief in me and their continuous support.

8. References

[1] B. K. Kaufmann *et al.*, "mSLAb – An open-source masked stereolithography (mSLA) bioprinter," *HardwareX,* vol. 19, 2024, doi: 10.1016/j.ohx.2024.e00543.

[2] E. Mancha Sánchez *et al.*, "Hydrogels for Bioprinting: A Systematic Review of Hydrogels Synthesis, Bioprinting Parameters, and Bioprinted Structures Behavior," *Frontiers in Bioengineering and Biotechnology,* vol. 8, 2020, doi: 10.3389/fbioe.2020.00776.

[3] L. Moroni *et al.*, "Biofabrication strategies for 3D in vitro models and regenerative medicine," *Nature Reviews Materials,* vol. 3, no. 5, pp. 21-37, 2018, doi: 10.1038/s41578-018-0006-y.

[4] S. V. Murphy and A. Atala, "3D bioprinting of tissues and organs," *Nature Biotechnology,* vol. 32, no. 8, pp. 773-785, 2014/08/01 2014, doi: 10.1038/nbt.2958.

[5] H. Wang *et al.*, "An Overview of Extracellular Matrix-Based Bioinks for 3D Bioprinting," (in English), *Frontiers in Bioengineering and Biotechnology,* Review vol. 10, 2022-May-11 2022, doi: 10.3389/fbioe.2022.905438.

[6] L. Moroni *et al.*, "Biofabrication: A Guide to Technology and Terminology," *Trends in Biotechnology,* vol. 36, no. 4, pp. 384-402, 2018, doi: 10.1016/j.tibtech.2017.10.015.

[7] M. E. Gomes, M. T. Rodrigues, R. M. A. Domingues, and R. L. Reis, "Tissue Engineering and Regenerative Medicine: New Trends and Directions—A Year in Review," *Tissue Engineering Part B: Reviews,* vol. 23, no. 3, pp. 211-224, 2017, doi: 10.1089/ten.teb.2017.0081.

[8] A. Shapira and T. Dvir, "3D Tissue and Organ Printing—Hope and Reality," *Advanced Science,* vol. 8, no. 10, p. 2003751, 2021, doi: https://doi.org/10.1002/advs.202003751.

[9] J. Malda *et al.*, "25th Anniversary Article: Engineering Hydrogels for Biofabrication," *Advanced Materials,* vol. 25, no. 36, pp. 5011-5028, 2013, doi: 10.1002/adma.201302042.

[10] M. Mobaraki, M. Ghaffari, A. Yazdanpanah, Y. Luo, and D. K. Mills, "Bioinks and bioprinting: A focused review," *Bioprinting,* vol. 18, p. e00080, 2020/06/01/ 2020, doi: https://doi.org/10.1016/j.bprint.2020.e00080.

[11] P. S. Gungor-Ozkerim, I. Inci, Y. S. Zhang, A. Khademhosseini, and M. R. Dokmeci, "Bioinks for 3D bioprinting: an overview," *Biomaterials Science,* vol. 6, no. 5, pp. 915-946, 2018, doi: 10.1039/c7bm00765e.

[12] W. Sun *et al.*, "The bioprinting roadmap," *Biofabrication,* vol. 12, no. 2, p. 022002, 2020, doi: 10.1088/1758-5090/ab5158.

[13] A. C. Daly, M. E. Prendergast, A. J. Hughes, and J. A. Burdick, "Bioprinting for the Biologist," *Cell,* vol. 184, no. 1, pp. 18-32, 2021, doi: 10.1016/j.cell.2020.12.002.

[14] W. L. Ng, C. K. Chua, and Y.-F. Shen, "Print Me An Organ! Why We Are Not There Yet," *Progress in Polymer Science,* vol. 97, p. 101145, 2019/10/01/ 2019, doi: https://doi.org/10.1016/j.progpolymsci.2019.101145.

[15] J. A. Tavares-Negrete, C. Babayigit, S. Najafikoshnoo, S. W. Lee, O. Boyraz, and R. Esfandyarpour, "A Novel 3D-Bioprinting Technology of Orderly Extruded Multi-Materials via Photopolymerization," *Advanced Materials Technologies,* vol. 8, no. 12, 2023, doi: 10.1002/admt.202201926.

[16] A. Erben *et al.*, "Precision 3D-Printed Cell Scaffolds Mimicking Native Tissue Composition and Mechanics," *Advanced Healthcare Materials,* vol. 9, no. 24, p. 2000918, 2020, doi: https://doi.org/10.1002/adhm.202000918.

[17] Z. Wang *et al.*, "Visible Light Photoinitiation of Cell-Adhesive Gelatin Methacryloyl Hydrogels for Stereolithography 3D Bioprinting," *ACS Applied Materials & Interfaces,* vol. 10, no. 32, pp. 26859-26869, 2018/08/15 2018, doi: 10.1021/acsami.8b06607.

[18] M. Yang *et al.*, "Multi-Material Digital Light Processing (DLP) Bioprinting of Heterogeneous Hydrogel Constructs with Perfusable Networks," *Advanced Functional Materials,* vol. 34, no. 32, 2024, doi: 10.1002/adfm.202316456.

[19] R. Zhang and N. B. Larsen, "Stereolithographic hydrogel printing of 3D culture chips with biofunctionalized complex 3D perfusion networks," *Lab on a Chip,* vol. 17, no. 24, pp. 4273-4282, 2017, doi: 10.1039/c7lc00926g.

[20] N. Anandakrishnan *et al.*, "Fast Stereolithography Printing of Large-Scale Biocompatible Hydrogel Models," *Advanced Healthcare Materials,* vol. 10, no. 10, p. 2002103, 2021, doi: 10.1002/adhm.202002103.

[21] I. Ahmed, K. Sullivan, and A. Priye, "Multi-Resin Masked Stereolithography (MSLA) 3D Printing for Rapid and Inexpensive Prototyping of Microfluidic Chips with Integrated Functional Components," *Biosensors,* vol. 12, no. 8, p. 652, 2022, doi: 10.3390/bios12080652.

[22] S. Gassmann, S. Jegatheeswaran, T. Schleifer, H. Arbabi, and H. Schütte, "3D Printed PCB Microfluidics," *Micromachines,* vol. 13, no. 3, p. 470, 2022, doi: 10.3390/mi13030470.

[23] A. Minin, I. Blatov, S. Rodionov, and I. Zubarev, "Development of a cell co-cultivation system based on protein magnetic membranes, using a MSLA 3D printer," *Bioprinting,* vol. 23, p. e00150, 2021/08/01/ 2021, doi: https://doi.org/10.1016/j.bprint.2021.e00150.

[24] K. Elkhoury, J. Zuazola, and S. Vijayavenkataraman, "Bioprinting the future using light: A review on photocrosslinking reactions, photoreactive groups, and photoinitiators," *SLAS Technology,* vol. 28, no. 3, pp. 142-151, 2023, doi: 10.1016/j.slast.2023.02.003.

[25] C. Kim *et al.*, "Stem Cell Mechanosensation on Gelatin Methacryloyl (GelMA) Stiffness Gradient Hydrogels," *Annals of Biomedical Engineering,* vol. 48, no. 2, pp. 893-902, 2020/02/01 2020, doi: 10.1007/s10439-019-02428-5.

[26] B. J. Klotz, D. Gawlitta, A. J. W. P. Rosenberg, J. Malda, and F. P. W. Melchels, "Gelatin-Methacryloyl Hydrogels: Towards Biofabrication-Based Tissue Repair," *Trends in Biotechnology,* vol. 34, no. 5, pp. 394-407, 2016, doi: 10.1016/j.tibtech.2016.01.002.

[27] H. Kumar, K. Sakthivel, M. G. A. Mohamed, E. Boras, S. R. Shin, and K. Kim, "Designing Gelatin Methacryloyl (GelMA)-Based Bioinks for Visible Light Stereolithographic 3D Biofabrication," *Macromolecular Bioscience,* vol. 21, no. 1, p. 2000317, 2021, doi: 10.1002/mabi.202000317.

[28] H. Wang *et al.*, "General One-Pot Method for Preparing Highly Water-Soluble and Biocompatible Photoinitiators for Digital Light Processing-Based 3D Printing of Hydrogels," *ACS Applied Materials & Interfaces,* vol. 13, no. 46, pp. 55507-55516, 2021/11/24 2021, doi: 10.1021/acsami.1c15636.

[29] K. Yu *et al.*, "Printability during projection-based 3D bioprinting," *Bioactive Materials,* vol. 11, pp. 254-267, 2022/05/01/ 2022, doi: https://doi.org/10.1016/j.bioactmat.2021.09.021.

[30] H. Goodarzi Hosseinabadi, E. Dogan, A. K. Miri, and L. Ionov, "Digital Light Processing Bioprinting Advances for Microtissue Models," *ACS Biomater Sci Eng,* vol. 8, no. 4, pp. 1381-1395, Apr 11 2022, doi: https://doi.org/10.1021/acsbiomaterials.1c01509.

[31] W. Li, M. Wang, H. Ma, F. A. Chapa-Villarreal, A. O. Lobo, and Y. S. Zhang, "Stereolithography apparatus and digital light processing-based 3D bioprinting for tissue fabrication," *iScience,* vol. 26, no. 2, p. 106039, 2023/02/17/ 2023, doi: https://doi.org/10.1016/j.isci.2023.106039.

[32] A. Dupin *et al.*, "Synthetic cell–based materials extract positional information from morphogen gradients," *Science Advances,* vol. 8, no. 14, p. eabl9228, 2022, doi: doi:10.1126/sciadv.abl9228.

[33] F. Koch, O. Thaden, K. Trondle, R. Zengerle, S. Zimmermann, and P. Koltay, "Open-source hybrid 3D-bioprinter for simultaneous printing of thermoplastics and hydrogels," *HardwareX,* vol. 10, p. e00230, Oct 2021, doi: https://doi.org/10.1016/j.ohx.2021.e00230.

[34] M. Krane *et al.*, "Sequential Defects in Cardiac Lineage Commitment and Maturation Cause Hypoplastic Left Heart Syndrome," *Circulation,* vol. 144, no. 17, pp. 1409-1428, 2021, doi: doi:10.1161/CIRCULATIONAHA.121.056198.

[35] A. Krige, J. Haluska, U. Rova, and P. Christakopoulos, "Design and implementation of a low cost bio-printer modification, allowing for switching between plastic and gel extrusion," *HardwareX,* vol. 9, p. e00186, Apr 2021, doi: https://doi.org/10.1016/j.ohx.2021.e00186.

[36] G. Gillispie *et al.*, "Assessment methodologies for extrusion-based bioink printability," *Biofabrication,* vol. 12, no. 2, p. 022003, 2020/02/19 2020, doi: 10.1088/1758-5090/ab6f0d.

[37] J. Gong *et al.*, "Complexation-induced resolution enhancement of 3D-printed hydrogel constructs," *Nature Communications,* vol. 11, no. 1, p. 1267, 2020/03/09 2020, doi: https://doi.org/10.1038/s41467-020-14997-4.

[38] H. Gudapati, M. Dey, and I. Ozbolat, "A comprehensive review on droplet-based bioprinting: Past, present and future," *Biomaterials,* vol. 102, pp. 20-42, 2016/09/01/ 2016, doi: https://doi.org/10.1016/j.biomaterials.2016.06.012.

[39] A. Zennifer, A. Subramanian, and S. Sethuraman, "Design considerations of bioinks for laser bioprinting technique towards tissue regenerative applications," *Bioprinting,* vol. 27, p. e00205, 2022/08/01/ 2022, doi: https://doi.org/10.1016/j.bprint.2022.e00205.

[40] J. Zhang *et al.*, "Single Cell Bioprinting with Ultrashort Laser Pulses," *Advanced Functional Materials,* vol. 31, no. 19, p. 2100066, 2021, doi: https://doi.org/10.1002/adfm.202100066.

[41] J. Zhang *et al.*, "Dynamics of single cell femtosecond laser printing," (in eng), *Biomed Opt Express,* vol. 14, no. 5, pp. 2276-2292, May 1 2023, doi: 10.1364/boe.480286.

[42] A. A. Antoshin *et al.*, "LIFT-bioprinting, is it worth it?," *Bioprinting,* vol. 15, p. e00052, 2019/09/01/ 2019, doi: https://doi.org/10.1016/j.bprint.2019.e00052.

[43] A. Erben *et al.*, "Engineering Principles and Algorithmic Design Synthesis for Ultracompact Bio-Hybrid Perfusion Chip," *bioRxiv,* p. 2022.03.16.484492, 2022, doi: 10.1101/2022.03.16.484492.

[44] E. D. Lemma, B. Spagnolo, M. De Vittorio, and F. Pisanello, "Studying Cell Mechanobiology in 3D: The Two-Photon Lithography Approach," *Trends in Biotechnology,* vol. 37, no. 4, pp. 358-372, 2019, doi: 10.1016/j.tibtech.2018.09.008.

[45] A. Tudor *et al.*, "Fabrication of soft, stimulus-responsive structures with sub-micron resolution via two-photon polymerization of poly(ionic liquid)s," *Materials Today,* vol. 21, no. 8, pp. 807-816, 2018/10/01/ 2018, doi: https://doi.org/10.1016/j.mattod.2018.07.017.

[46] F. Zurita *et al.*, "Fully 3D-Printed Cuff Electrode for Small Nerve Interfacing," *Advanced Materials Technologies,* vol. 8, no. 3, p. 2200989, 2023, doi: https://doi.org/10.1002/admt.202200989.

[47] Y. Li *et al.*, "High-fidelity and high-efficiency additive manufacturing using tunable pre-curing digital light processing," *Additive Manufacturing,* vol. 30, p. 100889, 2019/12/01/ 2019, doi: https://doi.org/10.1016/j.addma.2019.100889.

[48] J. Van Hoorick *et al.*, "(Photo-)crosslinkable gelatin derivatives for biofabrication applications," *Acta Biomaterialia,* vol. 97, pp. 46-73, 2019/10/01/ 2019, doi: https://doi.org/10.1016/j.actbio.2019.07.035.

[49] Y. Wu *et al.*, "The influence of the stiffness of GelMA substrate on the outgrowth of PC12 cells," *Bioscience Reports,* vol. 39, no. 1, 2019, doi: 10.1042/bsr20181748.

[50] V. Kokol and S. Gorgieva, "Collagen- vs. Gelatine-Based Biomaterials and Their Biocompatibility: Review and Perspectives," in *Biomaterials - Applications for Nanomedicine*, R. Pignatello Ed. Rijeka: IntechOpen, 2011.

[51] A. G. Ward and A. Courts, *The Science and technology of gelatin / edited by A. G. Ward, A. Courts* (Food science and technology). London ;: Academic Press, 1977.

[52] J.-F. Pan *et al.*, "One-step cross-linked injectable hydrogels with tunable properties for space-filling scaffolds in tissue engineering," *RSC Advances,* vol. 5, no. 51, pp. 40820-40830, 2015, doi: 10.1039/c5ra02588e.

[53] C.-H. Lin, J. J.-M. Su, S.-Y. Lee, and Y.-M. Lin, "Stiffness modification of photopolymerizable gelatin-methacrylate hydrogels influences endothelial differentiation of human mesenchymal stem cells," *Journal of Tissue Engineering and Regenerative Medicine,* vol. 12, no. 10, pp. 2099-2111, 2018, doi: https://doi.org/10.1002/term.2745.

[54] S. Gao *et al.*, "3D-bioprinted GelMA nerve guidance conduits promoted peripheral nerve regeneration by inducing trans-differentiation of MSCs into SCLCs via PIEZO1/YAP axis," *Materials Today Advances,* vol. 17, p. 100325, 2023/03/01/ 2023, doi: https://doi.org/10.1016/j.mtadv.2022.100325.

[55] Y. Zheng *et al.*, "Neuro-regenerative imidazole-functionalized GelMA hydrogel loaded with hAMSC and SDF-1α promote stem cell differentiation and repair focal brain injury," *Bioactive Materials,* vol. 6, no. 3, pp. 627-637, 2021/03/01/ 2021, doi: https://doi.org/10.1016/j.bioactmat.2020.08.026.

[56] C. Claaßen *et al.*, "Quantification of Substitution of Gelatin Methacryloyl: Best Practice and Current Pitfalls," *Biomacromolecules,* vol. 19, no. 1, pp. 42-52, 2018/01/08 2018, doi: 10.1021/acs.biomac.7b01221.

[57] E. Hoch, T. Hirth, G. E. M. Tovar, and K. Borchers, "Chemical tailoring of gelatin to adjust its chemical and physical properties for functional bioprinting," *Journal of Materials Chemistry B,* vol. 1, no. 41, p. 5675, 2013, doi: 10.1039/c3tb20745e.

[58] E. Hoch, C. Schuh, T. Hirth, G. E. M. Tovar, and K. Borchers, "Stiff gelatin hydrogels can be photo-chemically synthesized from low viscous gelatin solutions using molecularly functionalized gelatin with a high degree of methacrylation," *Journal of Materials Science: Materials in Medicine,* vol. 23, no. 11, pp. 2607-2617, 2012, doi: 10.1007/s10856-012-4731-2.

[59] M. Zhu, Y. Wang, G. Ferracci, J. Zheng, N.-J. Cho, and B. H. Lee, "Gelatin methacryloyl and its hydrogels with an exceptional degree of controllability and batch-to-batch consistency," *Scientific Reports,* vol. 9, no. 1, 2019, doi: 10.1038/s41598-019-42186-x.

[60] D. Loessner *et al.*, "Functionalization, preparation and use of cell-laden gelatin methacryloyl–based hydrogels as modular tissue culture platforms," *Nature Protocols,* vol. 11, no. 4, pp. 727-746, 2016/04/01 2016, doi: 10.1038/nprot.2016.037.

[61] B. D. Fairbanks, M. P. Schwartz, C. N. Bowman, and K. S. Anseth, "Photoinitiated polymerization of PEG-diacrylate with lithium phenyl-2,4,6-trimethylbenzoylphosphinate: polymerization rate and cytocompatibility," *Biomaterials,* vol. 30, no. 35, pp. 6702-6707, 2009, doi: 10.1016/j.biomaterials.2009.08.055.

[62] A. K. Nguyen, P. L. Goering, V. Reipa, and R. J. Narayan, "Toxicity and photosensitizing assessment of gelatin methacryloyl-based hydrogels photoinitiated with lithium phenyl-2,4,6-trimethylbenzoylphosphinate in human primary renal proximal tubule epithelial cells," *Biointerphases,* vol. 14, no. 2, p. 021007, 2019, doi: 10.1116/1.5095886.

[63] H. Xu, J. Casillas, S. Krishnamoorthy, and C. Xu, "Effects of Irgacure 2959 and lithium phenyl-2,4,6-trimethylbenzoylphosphinate on cell viability, physical properties, and microstructure in 3D bioprinting of vascular-like constructs," *Biomedical Materials,* vol. 15, no. 5, p. 055021, 2020, doi: 10.1088/1748-605x/ab954e.

[64] M. Klak *et al.*, "Irradiation with 365 nm and 405 nm wavelength shows differences in DNA damage of swine pancreatic islets," *PLOS ONE,* vol. 15, no. 6, p. e0235052, 2020, doi: 10.1371/journal.pone.0235052.

[65] X.-H. Qin, A. Ovsianikov, J. Stampfl, and R. Liska, "Additive manufacturing of photosensitive hydrogels for tissue engineering applications," *BioNanoMaterials,* vol. 15, no. 3-4, 2014, doi: 10.1515/bnm-2014-0008.

[66] A. Faralli, F. Melander, E. K. U. Larsen, S. Chernyy, T. L. Andresen, and N. B. Larsen, "Multiplexed Dosing Assays by Digitally Definable Hydrogel Volumes," *Advanced Healthcare Materials,* vol. 5, no. 2, pp. 244-254, 2016, doi: 10.1002/adhm.201500542.

[67] J. Nie, S. Lou, A. M. A. O. Pollet, M. Van Vegchel, C. V. C. Bouten, and J. M. J. Den Toonder, "A Cell Pre-Wrapping Seeding Technique for Hydrogel-Based Tubular Organ-On-A-Chip," *Advanced Science,* vol. 11, no. 30, 2024, doi: 10.1002/advs.202400970.

[68] M. L. Tomov *et al.*, "A 3D Bioprinted In Vitro Model of Pulmonary Artery Atresia to Evaluate Endothelial Cell Response to Microenvironment," *Advanced Healthcare Materials,* vol. 10, no. 20, p. 2100968, 2021, doi: 10.1002/adhm.202100968.

[69] Y. Zhang *et al.*, "A Bioadhesive Nanoparticle–Hydrogel Hybrid System for Localized Antimicrobial Drug Delivery," *ACS Applied Materials & Interfaces,* vol. 8, no. 28, pp. 18367-18374, 2016/07/20 2016, doi: 10.1021/acsami.6b04858.

[70] J. Konasch *et al.*, "A Novel Hybrid Additive Manufacturing Process for Drug Delivery Systems with Locally Incorporated Drug Depots," *Pharmaceutics,* vol. 11, no. 12, p. 661, 2019. [Online]. Available: https://www.mdpi.com/1999-4923/11/12/661.

[71] H. Seo, S. G. Heo, H. Lee, and H. Yoon, "Preparation of PEG materials for constructing complex structures by stereolithographic 3D printing," *RSC Advances,* vol. 7, no. 46, pp. 28684-28688, 2017, doi: 10.1039/c7ra04492e.

[72] H. Oettel, H. Frohberg, H. Nothdurft, and G. Wilhelm, "Die Prüfung einiger synthetischer Farbstoffe auf ihre Eignung zur LebensmittelfÄrbung," *Archiv für Toxikologie,* vol. 21, no. 1, pp. 9-29, 1965/01/01 1965, doi: 10.1007/BF00578966.

[73] H. K. Bankhede and A. Ganguly, "Pharmaceutical polymer-based hydrogel formulations as prospective bioinks for 3D bioprinting applications: A step towards clean bioprinting," *Annals of 3D Printed Medicine,* vol. 6, p. 100056, 2022/06/01/ 2022, doi: https://doi.org/10.1016/j.stlm.2022.100056.

[74] N. Khorshidi and A. Niazi, "A novel ion pair based surfactant assisted microextraction modified by orthogonal signal correction partial least squares for determination of food dyes," *Journal of Food Measurement and Characterization,* vol. 12, no. 3, pp. 1885-1895, 2018, doi: 10.1007/s11694-018-9802-8.

[75] K. Dubbin *et al.*, "Projection Microstereolithographic Microbial Bioprinting for Engineered Biofilms," *Nano Letters,* vol. 21, no. 3, pp. 1352-1359, 2021/02/10 2021, doi: 10.1021/acs.nanolett.0c04100.

[76] K. Asadpour-Zeynali and S. Manafi-Khoshmanesh, "Simultaneous Spectrophotometric Determination of Sunset Yellow and Quinoline Yellow in a Single Step," *Journal of the Chinese Chemical Society,* vol. 62, no. 9, pp. 772-779, 2015, doi: 10.1002/jccs.201400529.

[77] B. K. R. Kaufmann, Matthias; Pechtl, Markus; Wildenburg, Geronimo; Hayden, Oliver; Clausen-Schaumann, Hauke; Sudhop, Stefanie, "mSLAb – an open-source masked stereolithography (mSLA) bioprinter," *Mendeley Data,* vol. V1, 13 November 2023 2023, doi: 10.17632/kxt5sks9zs.1.

[78] V. Saranathan *et al.*, "Structure, function, and self-assembly of single network gyroid (I 4 ₁ 32) photonic crystals in butterfly wing scales," *Proceedings of the National Academy of Sciences,* vol. 107, no. 26, pp. 11676-11681, 2010, doi: 10.1073/pnas.0909616107.

[79] K. Michielsen and D. G. Stavenga, "Gyroid cuticular structures in butterfly wing scales: biological photonic crystals," *Journal of The Royal Society Interface,* vol. 5, no. 18, pp. 85-94, 2008, doi: 10.1098/rsif.2007.1065.

[80] V. Saranathan, S. Narayanan, A. Sandy, E. R. Dufresne, and R. O. Prum, "Evolution of single gyroid photonic crystals in bird feathers," *Proceedings of the National Academy of Sciences,* vol. 118, no. 23, p. e2101357118, 2021, doi: 10.1073/pnas.2101357118.

[81] A. H. Schoen, *Infinite periodic minimal surfaces without self-intersections*. National Aeronautics and Space Administration, 1970.

[82] S. N. Khaderi, V. S. Deshpande, and N. A. Fleck, "The stiffness and strength of the gyroid lattice," *International Journal of Solids and Structures,* vol. 51, no. 23,

pp. 3866-3877, 2014/11/01/ 2014, doi: https://doi.org/10.1016/j.ijsolstr.2014.06.024.

[83] Z. Qin, G. S. Jung, M. J. Kang, and M. J. Buehler, "The mechanics and design of a lightweight three-dimensional graphene assembly," *Science Advances,* vol. 3, no. 1, p. e1601536, 2017, doi: 10.1126/sciadv.1601536.

[84] D. W. Abueidda, M. Elhebeary, C.-S. Shiang, S. Pang, R. K. Abu Al-Rub, and I. M. Jasiuk, "Mechanical properties of 3D printed polymeric Gyroid cellular structures: Experimental and finite element study," *Materials & Design,* vol. 165, p. 107597, 2019/03/05/ 2019, doi: https://doi.org/10.1016/j.matdes.2019.107597.

[85] C. Silva, A. I. Pais, G. Caldas, B. P. P. A. Gouveia, J. L. Alves, and J. Belinha, "Study on 3D printing of gyroid-based structures for superior structural behaviour," *Progress in Additive Manufacturing,* vol. 6, no. 4, pp. 689-703, 2021, doi: 10.1007/s40964-021-00191-5.

[86] E. Mancini, M. Utzeri, E. Farotti, A. Lattanzi, and M. Sasso, "DLP printed 3D gyroid structure: Mechanical response at meso and macro scale," *Mechanics of Materials,* vol. 192, p. 104970, 2024/05/01/ 2024, doi: https://doi.org/10.1016/j.mechmat.2024.104970.

[87] D.-J. Yoo, "Advanced porous scaffold design using multi-void triply periodic minimal surface models with high surface area to volume ratios," *International Journal of Precision Engineering and Manufacturing,* vol. 15, no. 8, pp. 1657-1666, 2014, doi: 10.1007/s12541-014-0516-5.

[88] L. Germain, C. A. Fuentes, A. W. Van Vuure, A. Des Rieux, and C. Dupont-Gillain, "3D-printed biodegradable gyroid scaffolds for tissue engineering applications," *Materials & Design,* vol. 151, pp. 113-122, 2018, doi: 10.1016/j.matdes.2018.04.037.

[89] M. D. Poskus, T. Wang, Y. Deng, S. Borcherding, J. Atkinson, and I. K. Zervantonakis, "Fabrication of 3D-printed molds for polydimethylsiloxane-based microfluidic devices using a liquid crystal display-based vat photopolymerization process: printing quality, drug response and 3D invasion cell culture assays," *Microsystems & Nanoengineering,* vol. 9, no. 1, p. 140, 2023/11/09 2023, doi: 10.1038/s41378-023-00607-y.

[90] B. Venzac *et al.*, "PDMS Curing Inhibition on 3D-Printed Molds: Why? Also, How to Avoid It?," *Analytical Chemistry,* vol. 93, no. 19, pp. 7180-7187, 2021/05/18 2021, doi: 10.1021/acs.analchem.0c04944.

[91] W. Böcker *et al.*, "Introducing a single-cell-derived human mesenchymal stem cell line expressing hTERT after lentiviral gene transfer," (in eng), *J Cell Mol Med,* vol. 12, no. 4, pp. 1347-59, Aug 2008, doi: 10.1111/j.1582-4934.2008.00299.x.

[92] Z. Yin, "Establishment of a clonal immortalized human mesenchymal stem cell line expressing hTERT using lentiviral gene transfer," Dissertation, LMU München, 2012. [Online]. Available: http://nbn-resolving.de/urn:nbn:de:bvb:19-145290

[93] M. B. Goldring, "Culture of Immortalized Chondrocytes and Their Use As Models of Chondrocyte Function," in *Cartilage and Osteoarthritis: Volume 1: Cellular and Molecular Tools*, M. Sabatini, P. Pastoureau, and F. De Ceuninck Eds. Totowa, NJ: Humana Press, 2004, pp. 37-52.

[94] M. B. Goldring *et al.*, "Interleukin-1 beta-modulated gene expression in immortalized human chondrocytes," (in eng), *J Clin Invest,* vol. 94, no. 6, pp. 2307-16, Dec 1994, doi: 10.1172/jci117595.

[95] Y. Lee, Q. Wang, I. Shuryak, D. J. Brenner, and H. C. Turner, "Development of a high-throughput γ-H2AX assay based on imaging flow cytometry," *Radiation Oncology,* vol. 14, no. 1, 2019, doi: 10.1186/s13014-019-1344-7.

[96] F. A. Auger, L. Gibot, and D. Lacroix, "The Pivotal Role of Vascularization in Tissue Engineering," *Annual Review of Biomedical Engineering,* vol. 15, no. Volume 15, 2013, pp. 177-200, 2013, doi: https://doi.org/10.1146/annurev-bioeng-071812-152428.

[97] E. C. Novosel, C. Kleinhans, and P. J. Kluger, "Vascularization is the key challenge in tissue engineering," *Advanced Drug Delivery Reviews,* vol. 63, no. 4, pp. 300-311, 2011/04/30/ 2011, doi: https://doi.org/10.1016/j.addr.2011.03.004.

[98] G. Yang, B. Mahadik, J. Y. Choi, and J. P. Fisher, "Vascularization in tissue engineering: fundamentals and state-of-art," *Progress in Biomedical Engineering,* vol. 2, no. 1, p. 012002, 2020/01/09 2020, doi: 10.1088/2516-1091/ab5637.

[99] Q. Gao, Y. He, J.-z. Fu, A. Liu, and L. Ma, "Coaxial nozzle-assisted 3D bioprinting with built-in microchannels for nutrients delivery," *Biomaterials,* vol. 61, pp. 203-215, 2015/08/01/ 2015, doi: https://doi.org/10.1016/j.biomaterials.2015.05.031.

[100] D. B. Kolesky, K. A. Homan, M. A. Skylar-Scott, and J. A. Lewis, "Three-dimensional bioprinting of thick vascularized tissues," *Proceedings of the National Academy of Sciences,* vol. 113, no. 12, pp. 3179-3184, 2016, doi: 10.1073/pnas.1521342113.

[101] D. B. Kolesky, R. L. Truby, A. S. Gladman, T. A. Busbee, K. A. Homan, and J. A. Lewis, "3D Bioprinting of Vascularized, Heterogeneous Cell-Laden Tissue Constructs," *Advanced Materials,* vol. 26, no. 19, pp. 3124-3130, 2014, doi: 10.1002/adma.201305506.

[102] C. Prein, N. Warmbold, Z. Farkas, M. Schieker, A. Aszodi, and H. Clausen-Schaumann, "Structural and mechanical properties of the proliferative zone of the developing murine growth plate cartilage assessed by atomic force microscopy," *Matrix Biology,* vol. 50, pp. 1-15, 2016/03/01/ 2016, doi: https://doi.org/10.1016/j.matbio.2015.10.001.

[103] E. D'Arcangelo and A. P. McGuigan, "Micropatterning Strategies to Engineer Controlled Cell and Tissue Architecture in Vitro," *BioTechniques,* vol. 58, no. 1, pp. 13-23, 2015, doi: 10.2144/000114245.

[104] M. Théry, "Micropatterning as a tool to decipher cell morphogenesis and functions," *Journal of Cell Science,* vol. 123, no. 24, pp. 4201-4213, 2010, doi: 10.1242/jcs.075150.

[105] S. Sharifi, H. Sharifi, A. Akbari, and J. Chodosh, "Systematic optimization of visible light-induced crosslinking conditions of gelatin methacryloyl (GelMA)," *Scientific Reports,* vol. 11, no. 1, 2021, doi: 10.1038/s41598-021-02830-x.

[106] S. Duchi *et al.*, "Handheld Co-Axial Bioprinting: Application to in situ surgical cartilage repair," *Scientific Reports,* vol. 7, no. 1, 2017, doi: 10.1038/s41598-017-05699-x.

[107] A. Kalilayeva, D. Zhumashev, D. Wei, A. Perveen, and D. Talamona, "Investigation of Stereolithography Additively Manufactured Components for Deviations in Dimensional and Geometrical Features," *Polymers,* vol. 16, no. 23, p. 3311, 2024, doi: 10.3390/polym16233311.

[108] K. Chen, M. Xu, F. Lu, and Y. He, "Development of Matrix Metalloproteinases-Mediated Extracellular Matrix Remodeling in Regenerative Medicine: A Mini Review," *Tissue Engineering and Regenerative Medicine,* vol. 20, no. 5, pp. 661-670, 2023, doi: 10.1007/s13770-023-00536-x.

[109] W.-Z. Tu *et al.*, "γH2AX foci formation in the absence of DNA damage: Mitotic H2AX phosphorylation is mediated by the DNA-PKcs/CHK2 pathway," *FEBS Letters,* vol. 587, no. 21, pp. 3437-3443, 2013, doi: 10.1016/j.febslet.2013.08.028.

[110] Z. S. Galis and J. J. Khatri, "Matrix Metalloproteinases in Vascular Remodeling and Atherogenesis," *Circulation Research,* vol. 90, no. 3, pp. 251-262, 2002, doi: 10.1161/res.90.3.251.

[111] W. Liu *et al.*, "Extrusion Bioprinting of Shear-Thinning Gelatin Methacryloyl Bioinks," *Advanced Healthcare Materials,* vol. 6, no. 12, p. 1601451, 2017, doi: 10.1002/adhm.201601451.

[112] S. Boularaoui, G. Al Hussein, K. A. Khan, N. Christoforou, and C. Stefanini, "An overview of extrusion-based bioprinting with a focus on induced shear stress and its effect on cell viability," *Bioprinting,* vol. 20, p. e00093, 2020/12/01/ 2020, doi: https://doi.org/10.1016/j.bprint.2020.e00093.

[113] G. Cidonio, M. Glinka, J. I. Dawson, and R. O. C. Oreffo, "The cell in the ink: Improving biofabrication by printing stem cells for skeletal regenerative medicine," *Biomaterials,* vol. 209, pp. 10-24, 2019/07/01/ 2019, doi: https://doi.org/10.1016/j.biomaterials.2019.04.009.

List of Publications

Publications directly related to my doctoral thesis:

Benedikt K. Kaufmann, Matthias Rudolph, Markus Pechtl, Geronimo Wildenburg, Oliver Hayden, Hauke Clausen-Schaumann, Stefanie Sudhop, **mSLAb – An open-source masked stereolithography (mSLA) bioprinter**, HardwareX, Volume 19 (2024), DOI: 10.1016/j.ohx.2024.e00543

Publications resulting from further projects and collaborations during my time as a PhD student:

Tanja D. Becke, Stefan Ness, **Benedikt K. Kaufmann**, Bastian Hartmann, Arndt F. Schilling, Stefanie Sudhop, Markus Hilleringmann, and Hauke Clausen-Schaumann, **Pilus-1 Backbone Protein RrgB of Streptococcus pneumoniae Binds Collagen I in a Force-Dependent Way**, ACS Nano 2019 13 (6), 7155-7165, DOI: 10.1021/acsnano.9b02587

Aurore Dupin, Lukas Aufinger, Igor Styazhkin, Florian Rothfischer, **Benedikt K. Kaufmann**, Sascha Schwarz, Nikolas Galensowske, Hauke Clausen-Schaumann, Friedrich C. Simmel, **Synthetic cell-based materials extract positional information from morphogen gradients**, Science Advances (2022), DOI: 10.1126/sciadv.abl9228